NEMA NU 4-2008 performance evaluation of the Raycan Trans-PET/CT X5 all-digital small animal PET/CT scanner prototype

Leon Riehakainen
41171

Master's thesis

Åbo Akademi University
Faculty of Science and Engineering
01.06.2018

Master´s degree of Biomedical Imaging
Small animal in-vivo imaging instrumentation

Credits: 45 ECTS

Supervisors:
1: Dr. Chunlei Han

2: Dr. Jarmo Teuho

3: Prof. Anne Roivainen

ÅBO AKADEMI UNIVERSITY
Biomedical Imaging
Faculty of Science and Engineering

LEON RIEHAKAINEN

NEMA NU 4-2008 performance evaluation of the Raycan Trans-PET/CT X5 all-digital small animal PET/CT scanner prototype

Master's thesis, 71 pp., 4 Appendices
06.2018

Abstract: By using a standardized measurement protocol, this study focused on evaluation of an all-digital Raycan positron emission tomography scanner prototype that was installed in Turku PET centre in May 2017 as a part of a research collaboration between Turku PET Centre (Turku, Finland) and RAYCAN Ltd/RAYDATA Ltd (Wuhan, China). In addition to testing the system performance in accordance with NEMA NU-4 2008, the image quality of the Raycan scanner was compared with Inveon and Molecubes systems currently in use in Turku PET Centre. Additionally, comparative imaging of live animals was performed on Raycan and Inveon systems. Finally, the measurement results were compared with other systems measured in accordance with the standard reported in the literature.

The image quality test for the Raycan system with three-dimensional ordered subset expectation maximization reconstruction algorithm and low post filter setting resulted in 4.6% standard deviation in uniformity, recovery coefficient values between 0.1 and 0.93 and spill-over ratios for water and air regions 14.3% and 22.75% respectively. The total absolute sensitivity obtained from single slice rebinned data is 87.3% and average absolute sensitivity is 0.87%. Using single slice rebinned data in a rat-sized phantom, the true counts peak is 73.9 kcps and noise equivalent counts peak is 64.3 kcps, both at 56.5 MBq activity. For a mouse-sized phantom, the true and noise equivalent count peaks are 152.8 and 141.3 kcps respectively at 55.9 MBq activity. Spatial resolution was calculated from two-dimensional filtered back projection and single slice rebinned data without filter and at the center of field of view produces 2.15/2.30/1.34 mm full width at half maximum resolution values for radial/tangential/axial directions. The corresponding values become 2.13/2.93/1.52 at 25 mm radial offset from the center of field of view and then rapidly become worse at 50 mm and beyond.

Animal imaging revealed that the system has problems with activity estimation for high uptake values during dynamic scans, but generally produces good quality images. In conclusion, it was determined that the prototype currently has an average performance compared to similar commercially available systems.

KEYWORDS: Positron Emission Tomography; National Electrical Manufacturers Association; System Evaluation; Raycan Trans-PET/CT X5; Small Animal Imaging; System Comparison;

List of Abbreviations

APD – Avalanche Photodiode

CT – Computed Tomography

DRAMA – Dynamic Row-Action Maximum Likelihood Algorithm

FBP – Filtered Back Projection

FDG –Fluorodeoxyglucose

FORE – Fourier Rebinning

FOV – Field of View (a – axial; t – transaxial)

FWHM – Full Width at Half Maximum

FWTM – Full Width at Tenth Maximum

LOR – Line(s) of Response

LSO – Lutetium Oxyorthosilicate

LYSO – Lutetium-Yttrium Oxyorthosilicate

MAP – Maximum *A posteriori*

MLEM – Maximum-Likelihood Expectation-Maximization

NEC – Noise Equivalent Count

NEMA – National Electrical Manufacturers Association

OSEM – Ordered Subset Expectation Maximization

PET – Positron Emission Tomography

PMT – Photomultiplier Tube

RC – Recovery Coefficient

ROI – Region of Interest

RP – Reprojection

SD – Standard Deviation

SF – Scatter Fraction

SOP – Standard Operating Procedure

SOR – Spill-Over Ratio

SPECT – Single-Photon Emission Computed Tomography

SSRB – Single-Slice Rebinning

SUV – Standardized Uptake Value

VOI – Volume of Interest

Table of Contents

1 Introduction

1.1 PET Imaging

Positron Emission Tomography (PET) is a biomedical imaging technology based on information technology, mathematics, nuclear physics and chemistry. From an early research of "tracer principle" described by Georg Karl von Hevesy in the 1920's (Bailey et al., 2014), it had developed into recognized clinical technology by the 1980's with the appearance of affordable computers and relevant technology such as cyclotrons (Anand et al., 2009). As a widely adjustable, flexible, non-invasive imaging method, it has now become one of the cornerstones of modern research dealing with anatomy and metabolic processes in oncology, neurology, cardiology, pharmacokinetics and other fields of research and medicine (Anand et al., 2009).

1.1.1 Radioactive Decay and Positron Annihilation

The PET procedure relies on the injectable radioactive tracers that accumulate in tracer-specific tissues. The accumulation is localized and quantified when the radionuclides within the tracer undergo beta plus (β^+) decay. Such radionuclides are also known as proton rich due to having an excess of protons in their nuclei, which is the reason behind their instability.

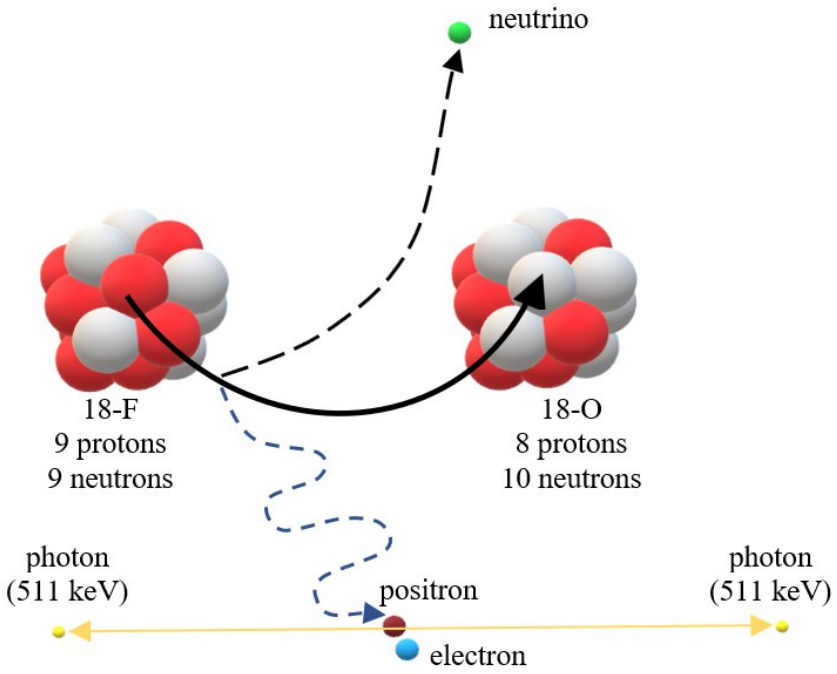

Figure 1. Example β^+ decay of fluorine-18 into oxygen-18 and positron reaction with electron.

Within the nuclei of these radionuclides, the positively-charged protons are continuously converted into neutrally charged neutrons, a process that emits positively-charged positrons and neutral electronic neutrinos (Figure 1). As the result, the element of the radionuclide shifts down by one atomic number. Positrons are, in turn, annihilated during interaction with nearby (depending on isotope, usually ~1 mm) electrons. The positron-electron interaction produces two 511 keV photons (gamma rays) that move in opposite directions and are thus detected. The 180˚ angle between the photons of known energy is the basic theory behind actual event localization.

1.1.2 Radionuclides and Tracers

The radionuclides used in PET imaging (Table 1) have different physical half-lifes, maximum positron energies, maximum positron ranges and linkable tracers (Nolting et al., 2012; Serdons et al., 2009). The differences in physical and chemical properties provide significant flexibility in designing suitable radiopharmaceuticals for specific needs.

Table 1. Widely used PET radionuclides, their physical half-lifes, maximum positron energies and ranges, related tracers and uses.

Radionuclide	Half-life	Maximum positron energy	Maximum positron range	Tracers	Use in PET
18-F	109.7 min	634 keV	~2.3 mm	FDG	metabolism
				NaF	bones
15-O	2.07 min	1732 keV	~8 mm	$H_2{}^{15}O$	perfusion
				$^{15}O_2$	metabolism
				$C^{15}O_2$	blood flow
				$C^{15}O$	blood volume
11-C	20.4 min	960 keV	~3.9 mm	carbon	metablolism, perfusion, etc
64-Cu	12.7 h	653 keV	~2.4 mm	Cl_2, peptides	metabolism, perfusion
13-N	9.96 min	1198 keV	~5.1 mm	ammonia	perfusion
68-Ga	67.72 min	1899 keV	~5.9 mm	DOTA-derivatized peptides	perfusion, blood flow, metabolism etc.
82-Rb	1.30 min	3150 keV	~16.5 mm	salt water	perfusion
124-I	4.18 d	2138 keV	~10.2 mm	Salt water, MIBG etc.	metabolism, diagnostics etc.

The period of radionuclide half-life determines the availability of tracers and duration of possible imaging studies. The higher positron energy, the longer distance it usually travels before annihilation, thus affecting the image quality and noise.

The radionuclides are generally produced either using reactors (neutron rich) or particle accelerators (neutron poor). Afterwards, they are introduced into tracers via chemical synthesis (Bailey et al., 2014). The properties of the tracers (except for cases like 82-Rb or 124-I that can be used independently in saline water solution) decide the behavior of radiopharmaceuticals in the body. For example, ^{18}F-FDG (fluorodeoxyglucose), as a glucose analogue, by participating in glucose metabolism allows to trace its uptake pathways and statistics in the tissues.

1.1.3 Detection and Acquisition

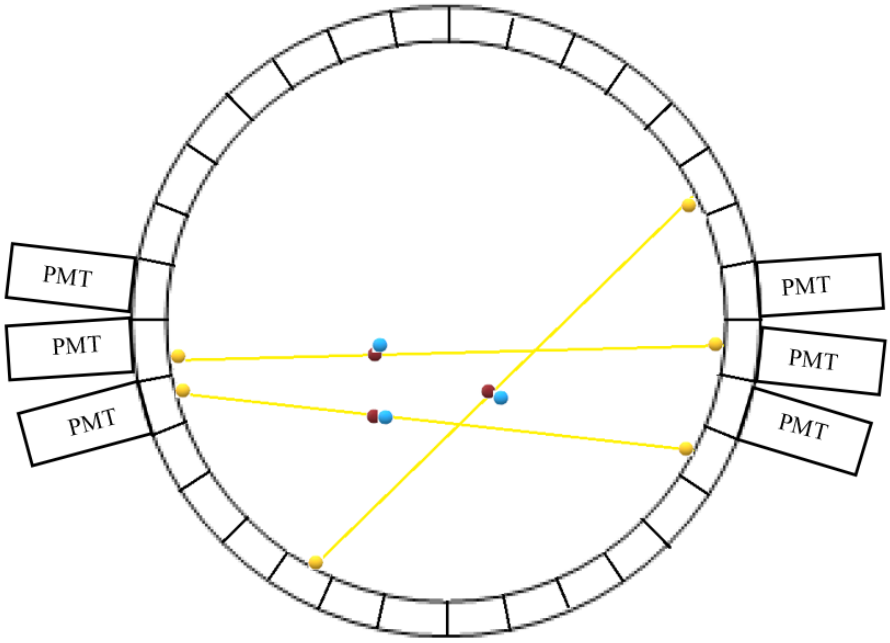

Figure 2. Diagram of positron annihilation event detection within one PET detector ring. Only part of PMTs are shown.

Most PET systems use scintillation crystal detectors for detecting the gamma rays (Figure 2). When a high-energy photon hits a scintillator, the crystal produces a low-energy photon in the form of a brief flash of luminescence (light). Because the luminescence emitted by the scintillator is weak and thus difficult to detect, the signal is boosted for example with the use of a photomultiplier tube (PMT), avalanche photodiode (APD), silicon photomultiplier (SiPM) or other methods (Vaquero and Kinahan, 2015). Within the PMT the photocathodes convert light photons into electrons. The electrons are multiplied by dynode array and after reaching the anode become the readable signal. The signals from all PMTs are analyzed within coincidence circuit that matches signals to positron annihilation events.

The PET imaging device can either acquire data in 2D format by gathering signals from an axially narrow range or as 3D, if coincidences from oblique planes are recorded as well (Figure 3). For 2D acquisition, the detector rings are separated by septa, metal separators that block the oblique incident photons.

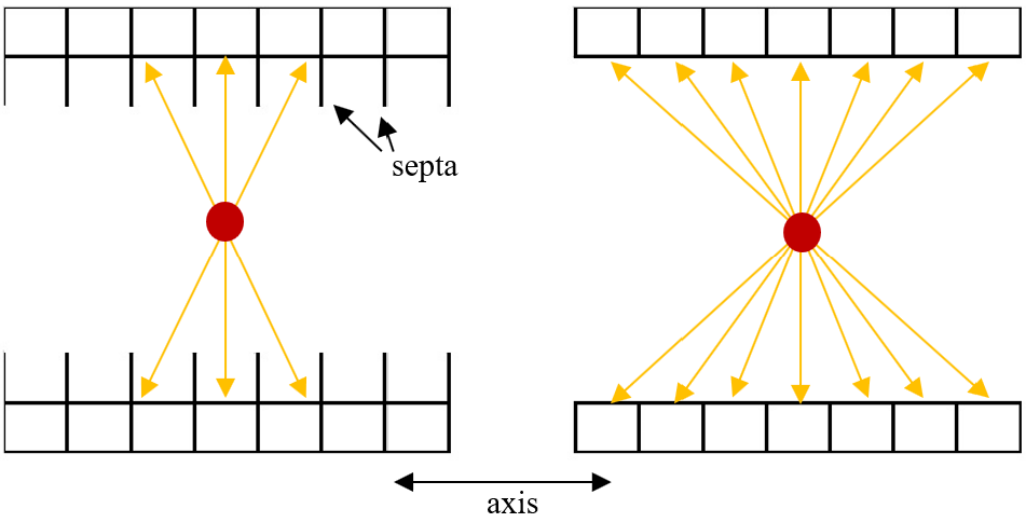

Figure 3. 2D and 3D PET ring composition. Adapted from Tong et al., 2010.

The gamma rays of suitable energy (511 keV) and within appropriate coincidence timing, usually 1-10 ns (Vaquero and Kinahan, 2015) are recorded as pairs. The line connecting the two detectors that had recorded the coincidence is known as line of response (LOR).

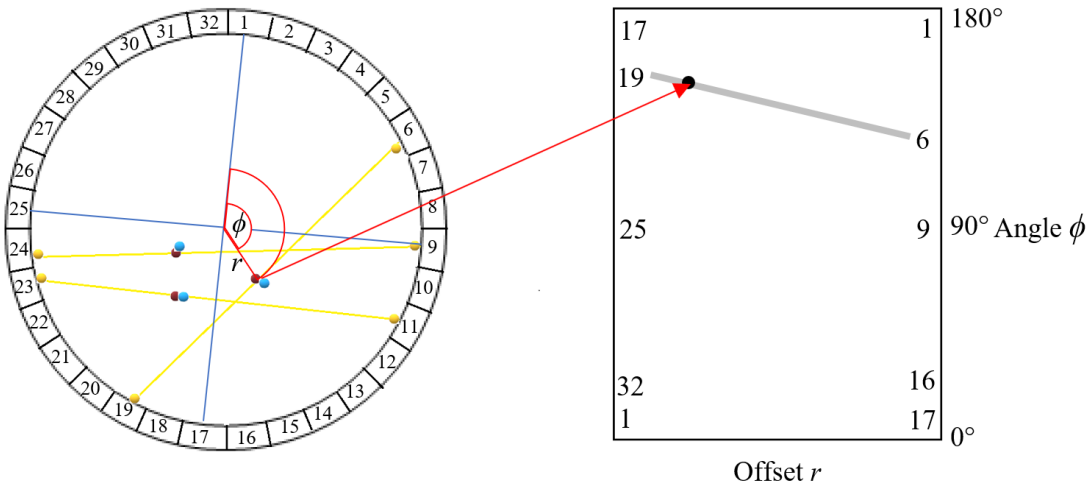

Figure 4. Signal recording on typical sinogram. LOR of annihilation event recorded as a line of the sinogram. Intersection points of multiple LORs represent the locations of increased activity.

For each plane, the coincidences are plotted as a collection of functions of angles and offsets producing the sinogram (Figure 4). 2D systems produce image volume from

separate sinograms that form individual slices, so a system with N rings and acquiring direct and cross coincidences produces 2N-1 sinograms (and slices). 3D systems can form sinograms for coincidences from all rings, bringing the total number of sinograms and slices up to $(N-1)^2$. Due to the sheer amount of data from 3D acquisitions, it is usually conceptualized in the form of michelograms (Fahey, 2002).

Traditional PET systems rely on forming numerous LORs to determine the positions of increased activity. New time-of-flight PET systems are capable of calculating the time difference between the coincidences with sufficient accuracy to calculate the relative distance and the position of each event (Vandenberghe et al., 2016).

1.1.4 Data Reconstruction

The gathered raw data have to be reconstructed to form a visual image. The two main types of image reconstructions are analytical and iterative.

A common example of analytical reconstruction is filtered back projection (FBP). FBP uses the process “back projection” mentioned in its name to draw the projection of the sources through the opposing sides of the image. By repeating that at 360° around the sources, the original points are then deduced by localizing the coordinates where the source projections intersect. Correspondingly, the numerous overlapping projections result in blurring. That requires the use of filtering as suggested by the part “filtered” in the name of FBP, which is performed by applying the ramp filter to accentuate lower frequencies. Consequently, the images obtained with the use of the FBP algorithm additionally lose some of their sharpness, finer details and contrast. That significantly degrades the quality of low-count images (Iriarte et al., 2016).

Currently being used and developed are iterative reconstruction algorithms based on the maximum likelihood expectation maximization (MLEM) calculation that belongs to the category of statistical algorithms. The key part of such algorithms is the term “iterative”, which means that the algorithm at each round of iteration compares the estimated data from the previous round with the measured data. Based on the measured information and produced estimations, corresponding adjustments are made to the updated image after each iteration, which finally results in the final image. Generally, this process yields statistically better images than obtained via analytical reconstructions. Due to the

calculations involved, the computation times for iterative algorithms can be significantly long.

For that reason, faster versions of the MLEM algorithm, such as ordered subsets expectation maximization (OSEM), have been developed. In the case of OSEM, the image (or projection) is separated into subsets that are updated separately at each iteration, thus improving the computation speed of the basic algorithm. However, over multiple repeated iterations, the image variance usually increases, thus slowly accumulating extra noise. Therefore, to obtain visually better images, the algorithm iterations are often limited without reaching the maximum result (which would then have minimum bias).

To reduce the size of data and keep calculation times acceptable, large-volume data (especially in 3D format) are usually rebinned to 2D data. That produces sets of direct LOR sinograms from oblique LOR sinograms, which means producing stacks of 2D data that are easier and faster to reconstruct. The Fourier rebinning algorithm (FORE) is widely used for both OSEM and FBP algorithms, replacing single slice rebinning (SSRB) that has been commonly used for FBP. SSRB, as the simplest rebinning method, uses averaging of all oblique sinograms that intersect the direct plane at the center of the transaxial field of view to form the direct slices. The FORE algorithm uses the similarity of elements in Fourier transformations to reversibly convert oblique sinograms into sets of equivalent direct sinograms (Tong et al., 2010).

1.1.5 PET Performance and Image Quality

Because PET is the multi-step technique involving different approaches for detection, collection, data reconstruction and corrections, its performance is subject to a multitude of independent sources of errors.

Starting from the positron annihilation event, the final results are already affected by variables such as positron range (travel distance before annihilation), non-collinearity caused by deviations of high-energy photons from the perfect 180° angle (also known as scatter) and loss of photon energy (attenuation) within the matter (Sánchez-Crespo et al., 2016). Additionally, simultaneous detections caused by different events or unrelated signals (randoms) cause misaligned LORs that create noise and reduce image contrast (Figure 5).

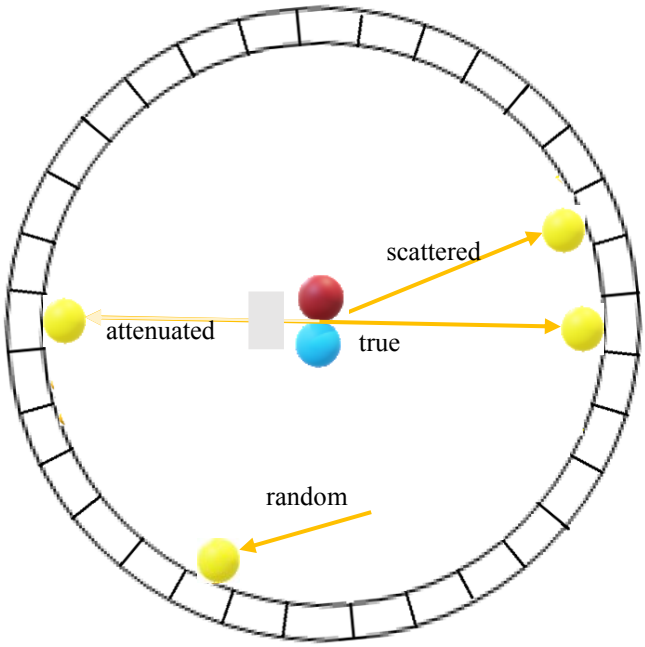

Figure 5. Scatter, random, true and attenuated detections of annihilation event.

The detection processes that use scintillation crystals and PMTs are dependent on the quality, design and structure of the scanner elements. The different shape, dimensions and materials of the crystals and the size of the gantry are directly affecting the sensitivity and resolutions (both spatial and temporal) of the system. For example, longer crystals stop high-energy photons better, which increases sensitivity, but at the same time reduces spatial resolution because of increased crystal width from oblique angles (parallax error). The detector dead time that refers to the period of time required for the detector to process the signal (including crystal scintillation and decay time, PMT processing speed and circuit efficiency) and minimum signal threshold parameters determine the ability of the system to detect both high and low counts. The design of detector electronics and implemented coincidence processing are heavily dependent on system design and manufacturer.

Including compensation for nonuniformity of detectors (normalization), the corrections for above mentioned attenuation, scatter, randoms, dead time and parallax errors are required to reconstruct the data into accurate images. For FBP, data are pre-corrected before reconstruction, while iterative algorithms should include corrections into the iteration loop to achieve the best accuracy and maintain the Poisson distribution of the data.

Finally, reconstruction algorithms and settings are the factors deciding the final quality of the images. Depending on the efficiency of implemented algorithms, the quality of corrections, the level of noise and uniformity can be significantly different even if the system hardware remains the same.

1.2. CT Imaging

1.2.1 Physical Basis of CT

Computed Tomography (CT) is an imaging procedure conventionally combined with PET. A CT system usually consists of a rotating x-ray source and a set of detectors opposite from the source (Figure 6). The electron tube produces x-rays by accelerating electrons released by the heated cathode and colliding them with the anode.

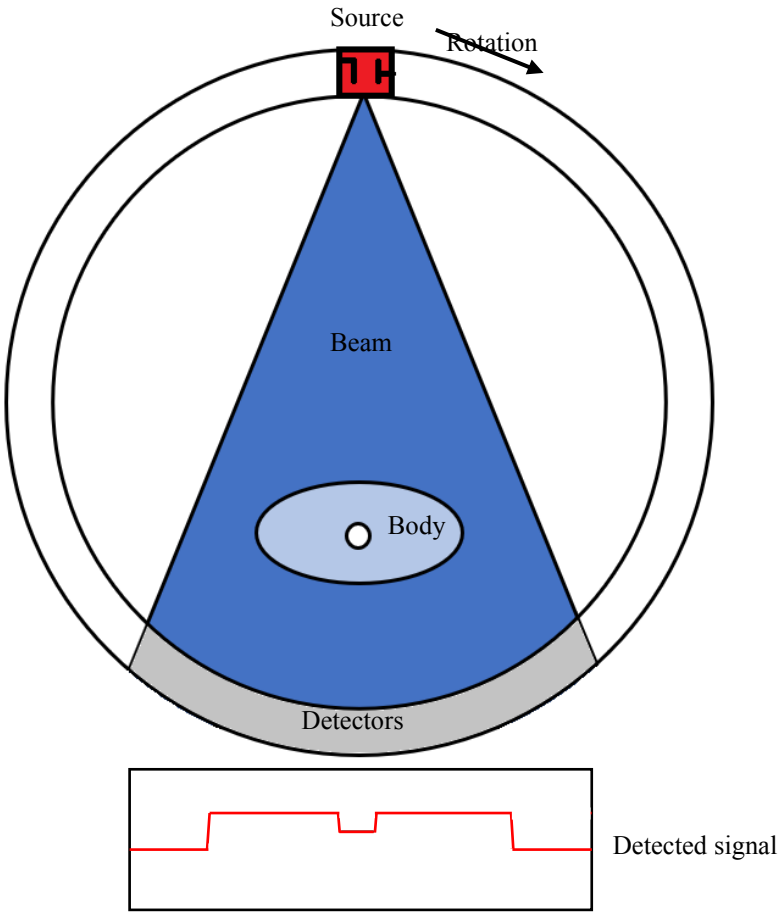

Figure 6. Structure of CT system and data acquisition.

The x-rays are photons with a wavelength longer than gamma rays, and are detected in similar fashion using for example scintillator crystals or semiconductors. When the x-rays pass through the tissues, they are absorbed differently depending on tissues,

producing signals of various strength. As the beam circles around the target, the signals from all angles are collected and recorded. To acquire a three-dimensional image, multiple stacks are acquired when either bed gradually moves along the axis or the x-ray unit circles in a spiral pattern around it. The collected signal data are combined into sinograms and reconstructed into image slices in a process similar to PET.

1.2.2 Application of CT in PET Imaging

CT images can be linked to PET images if spatial data of both are equalized. As CT data reflect tissue densities that allow to distinguish structures, computed tomography is conventionally used to provide accurate reference and data corrections for PET. Mostly, CT is used to correct attenuated events to compensate loss of photon energy when passing through the tissues.

The high-precision alternative to CT for attenuation factor calculation is to use 68-Ge, 68-Ga or 137-Cs sources rotated around the imaged body and calculate the attenuation factors for all possible lines of response from the gathered data (Turkington, 2011; Jones and Klein, 2015). However, the advantage of the combined PET/CT is the faster speed and shorter scan duration when compared to 68-Ge transmission scan.

1.3 Preclinical PET/CT

1.3.1 Motivation

As the oncological, cardiovascular and neurological causes continue to be the leading concerns of global healthcare, the related research can be considered as a major focus of multiple scientific fields. Because of the limitations of *ex vivo* experiments and simulated environments, animal testing continues to be an important part of biomedical studies.

PET, as the technology that can provide highly specific, time-resolved data of *in vivo* metabolic processes, has to be adapted for the requirements of animal studies. The non-invasive and repeatable technique allows to image the same animals multiple times, improving the quality of the studies and validity of the results (Levin and Zaidi, 2007; Yao et al., 2012). That, by increasing the efficiency of the research, reduces the duration of studies and the required number of animals.

1.3.2 Practical Application and Challenges

The studies of brain, different cancers and cardiac conditions can be effectively performed on laboratory animals. Due to the genetic similarity to humans, cheap price, variable strains, and simple and fast breeding, most preclinical PET systems focus on murine, mostly mouse and rat imaging. To obtain sufficiently detailed data from such small-sized targets, preclinical PET/CT systems have to have better photon sensitivity, spatial resolution and contrast than clinical systems.

Small animal size requires smaller injected radiation doses and, thus, places high demand on system sensitivity, the ability to detect photons and resolution, and the ability to separate the locations of detections. For that reason, most preclinical PET systems have small gantry sizes and bore diameters. To improve resolution, scintillator crystal sides facing the target are made smaller, but also longer, to ensure that the crystals have sufficient volume to stop highly penetrating 511 keV photons.

Compact detector geometry maximizes solid angle coverage and the longer crystals improve photon detection. However, the long and narrow crystals surrounding small gantry have a high rate of oblique photons interacting with the longer sides of the crystals (Figure 7). That causes so-called parallax error that degrades spatial resolution and distorts the actual positions of lines of response that, in turn, results in blurring and loss of contrast (Levin and Zaidi, 2007; Gu et al., 2015).

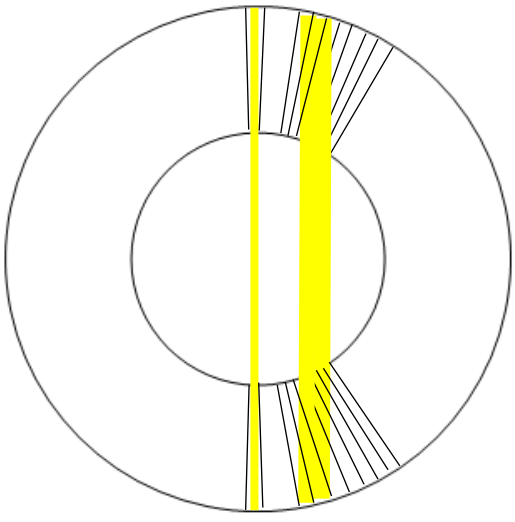

Figure 7. The effect of parallax error on detection process.

The parallax error is of significant concern for PET systems that are required to do simultaneous imaging of multiple animals. High throughput imaging is necessary for studies that can require multiple tens of animals to reach statistically significant results. Several animals result in complex attenuation and active use of the edge regions of field of view. The resulting noise and degradation of spatial resolution are issues that are approached in multiple ways – from specially designed beds to ensure the placement of regions of interest near the center of field of view to large-bore systems with large sensitive FOV area (Aide et al., 2012). To make sure that the results are precise and reproducible, common performance baselines of different PET systems are required. To do so, preclinical PET scanners need to be evaluated and standardized according to a uniform format.

1.4 NEMA NU 4-2008 Standard

1.4.1 NEMA NU 4-2008 Background

Because of the increasing importance of preclinical PET studies for pharmacological and medical research, the quantitative measurements have become the deciding part of the results. The differences between animal handling, protocols, imaging systems and reconstruction and analysis methods result in empirical results that can be difficult to replicate, confirm and compare. To ensure the quality and reproducibility, standard operation procedures (SOPs), accurate reporting and efficient system quality control are required (Mannheim et al., 2017).

This work focuses on performance evaluation of the PET component of a small animal PET/CT system. The current standard for preclinical small animal PET systems is NEMA NU 4-2008, that has been developed by Animal PET Standard Task Force chartered by the Nuclear Section and issued by National Electrical Manufacturers Association in 2008. NEMA standard specifies the methodology for evaluating the performance of animal imaging PET scanners, with the aim of providing the framework for conclusive evaluation and comparison of the available systems in reproducible manner.

The performance of PET systems is generally evaluated as the measures of energy, spatial and temporal resolution, sensitivity and image quality (Bailey at al., 2014). NEMA NU

4-2008 has separated most of these and some other measurable variables into four sections (Section 3 to 6). These sections are:

- Section 3: Spatial Resolution.
- Section 4: Scatter Fraction, Count Losses, and Random Coincidence Measurements.
- Section 5: Sensitivity.
- Section 6: Image Quality, Accuracy of Attenuation, and Scatter Corrections.

1.4.2 Spatial Resolution

Spatial resolution represents the ability of the system to separate different points of activity within space. As mentioned in Part 1.3, small animals such as mice and rats require higher system resolution for adequate imaging compared to humans. As a reference, just half a decade ago, the usual spatial resolution of clinical PET systems was in the range of 4-6 mm, despite better technical capabilities (Yao et al., 2012) and only now, with improved computing powers and data storage, new clinical systems with 1 mm resolution are being actively developed (Hsu et al., 2018).

However, average human weight is around 60-70 kg globally, while the mouse weight is around 25 grams and the rat 300 grams. The weight difference between humans and mice is thus over 2000 times, and 200 between humans and rats. By roughly translating that into body volume, the difference between the targets of clinical and preclinical systems is 2 to 3 orders of magnitude. Obviously, the current preclinical systems that have average spatial resolution of around 2 mm across the field of view (FOV) and 1 mm resolution at best, do not reach yet the ideal desired values. Therefore, the spatial resolution remains one of the most important parameters that is used to compare and evaluate preclinical PET systems.

The Spatial Resolution section of NEMA standard provides the raw, natural measure of system spatial resolution without the effect of smoothing. That allows direct and adequate comparison of different systems as long as the methodology is being followed.

1.4.3 Scatter Fraction, Count Losses, and Random Coincidence Measurements

Scatter fraction is a measure of energy resolution that describes the sensitivity of a system to scattered events. The gamma rays consisting of 511 keV photons scatter within the imaged body and are detected as true coincidences if they fall into the energy acceptance window (e.g. 350 keV to 650 keV), which results in inaccurate LORs. With the accumulation of misplaced LORs, the fraction of scattered events increases. As mentioned in Part 1.3, it is especially noticeable for small-sized gantry designs with small detector ring diameters that are prone to the parallax error.

The sensitivity of systems to scatter events is also linked to energy window settings, as the narrower range of accepted photon energies reduces the detector dead time and limits the possible detection of scattered events. Notably, the small animals have lesser body volumes that result in lesser intrinsic scatter and attenuation values compared to humans. On the other hand, the simultaneous imaging of multiple animals can produce results that are significantly different from single animal scans due to the complexity of tissue and activity distribution within FOV and thus increased complex attenuation, scatter and random events.

Count losses and random coincidences fall under temporal resolution and measure how the system deals with different numbers of simultaneous events that occur at different levels of activity, which is especially important for precise measurements at high activity values. The detector dead time decides the ability of detectors to process signals and thus defines the temporal resolution quality of the system. As described in Part 1.1.5, random and scattered events are significant sources of noise that directly affect image quality by producing misplaced lines of response. And similar to the scattered events, their influence can be adjusted by energy window settings. Additionally, systems with intrinsically radioactive detectors such as LSO and LYSO (contain 176-Lu) add to the background activity and have a noticeable effect on true and random coincidences during the performance evaluation measurements.

1.4.4 Sensitivity

System sensitivity is a measure describing the number of detections within set time for specific activity and evaluates the ability of the system to detect gamma rays from positron annihilation events. In essence, that represents how many of the annihilation

events are detected within the FOV, either as count rate (cps/Bq) or absolute value (percentage). Efficiency of the detectors is affected by detector geometry (crystal placement, septas etc), scintillator crystal quality, shape size and arrangement, photon detectors (PMTs, avalanche photodiodes etc) and energy window settings.

By using smaller-diameter detector rings, as described in Part 1.3, small-animal PET systems are designed to be more sensitive compared to clinical systems. The paper by Yao *et al.* (2012) mentions the best preclinical systems reaching maximum absolute sensitivity value of 10%, which placed it 3 times higher than state of the art human scanners. But already in 2013, a study by Gu *et al.* reported 18% maximum absolute sensitivity for the PETBox4 system (however, with extremely wide energy window setting 150-650 keV).

1.4.5 Image Quality, Accuracy of Attenuation, and Scatter Corrections

Because the quality of the PET image is a combination of multiple parameters, NEMA uses one test to simulate a standardized imaging situation. The effects of system hardware and software are combined to reflect the actual spatial resolution and the efficiency of corrections. Different from other sections evaluated by NEMA NU 4-2008, this section is heavily influenced by reconstruction methods and efficiency of data corrections. The variability of algorithms (iterative, analytical and their subtypes), filters, smoothing and correction factors make an accurate comparison of systems difficult and sometimes do not reflect the real capabilities of the systems.

A significant part of image quality depends on uniformity of the image throughout the FOV, which is also dependant on correction of attenuation and scatter effects caused by absorption and scatter of photons within the tissues. As a numeric value, it describes the percentage of deviation between highest and lowest values within the area.

Recovery coefficient, partly a form of measure of spatial resolution, refers to the system's ability to recover the activity concentration in different sized target areas. The accurate detections and measurements of small volumes of activity are an integral part of small animal imaging, where body structures are routinely measured in submillimetre scale.

Spill-over evaluated as a part of the test shows the effectiveness of data corrections implemented in the systems. The combination of attenuation, random and scatter corrections decide the quality of noise reduction and contrast.

1.4.6 Current State of Preclinical System Evaluation

There have been numerous publications about preclinical PET system evaluations within last two decades, starting from modified protocols for clinical PET scanners (NEMA NU2-1994 and revisions). With current NEMA NU 4-2008 standard, multiple tens of systems have been evaluated, notably including study by Goertzen et al. (2012), which included a comparison of 11 systems:

- microPET P4
- microPET Focus 220
- microPET R4
- microPET Focus 120
- Inveon
- ClearPET
- Mosaic HP
- Argus
- VrPET
- LabPET 8
- LabPET 12

This work further added other 13 studies that focused on NEMA NU 4-2008 evaluation of PET systems:

- NanoScan Mediso (Dahle, 2014)
- NanoPET/CT (Szanda et al., 2011)
- Albira (Pajak et al., 2016)
- ClearPET (Cañadas et al., 2011)
- rPET-1 (Cañadas et al., 2011)
- LabPET 8 (Prasad et al., 2011)
- ClairvivoPET (Sato et al., 2016)
- FLEX Triumph X-PET (Prasad et al., 2010)
- PETBox4 (Gu et al., 2013)

- NanoScan Mediso PET/MRI (Nagy et al., 2013)
- MuPET (Wong et al., 2012)
- Raycan Trans-PET BioCaliburn LH (Wang et al., 2015)
- Albira Trimodal PET/SPECT/CT (Spinks et al., 2014)

By combining these studies, this work further expands the comparative analysis and is tentatively the most up to date aggregation of preclinical PET system comparisons.

2 Aims

The aims of this study were to evaluate the new all-digital preclinical PET/CT scanner prototype "Trans-PET/CT X5" manufactured by RAYCAN Technology (China), recently installed in Turku PET Centre (Finland).

The Raycan scanners are using new digital sampling algorithms for the acquisition of PET scintillation pulse signals. Making that their major marketing point, RAYCAN promises improved system performance, reliability and increased potential for further upgrades.

The Raycan Trans-PET/CT X5 system in Turku PET Centre is a prototype of the next-generation system with the technical configuration almost identical to previous commercial Trans-PET® BioCaliburn® LH system evaluated by Wang et al. (2015). However, according to manufacturer, the Trans-PET/CT X5 system has implemented some optimization in firmware and circuits.

To evaluate the Raycan scanner and compare it to the existing systems, the evaluation standard NEMA NU 4-2008 provided by National Electrical Manufacturers Association (USA) was used. To find the baseline of system performance and for in-house comparison, the Raycan and two of the other PET/CT systems currently in Turku PET Centre (Siemens Inveon and Molecubes) were first analyzed at different settings with NEMA Section 6 (Image Quality) protocol. Further Sections 5 to 1 evaluations were performed only with the Raycan and the results compared with other systems in the form of literature review.

In addition to official standard, recommendations for future evaluation procedures were made and developed into a practical protocol to be used in future in-house testing.
The optimized performance guideline will be used for future animal imaging at Turku PET Centre.

The aims were as follows:

1. System performance and acceptance testing with NEMA NU 4-2008 standard.
2. Performance evaluation and comparison by measurements and literature review of the PET component of the Raycan PET/CT system against the current Inveon PET/CT scanner and other preclinical PET systems.
3. Establishing a performance baseline of the Raycan PET/CT system, which can then be optimized further for the animal imaging needs of Turku PET Centre.

3 Materials and Methods

3.1 PET/CT systems

3.1.1 Raycan

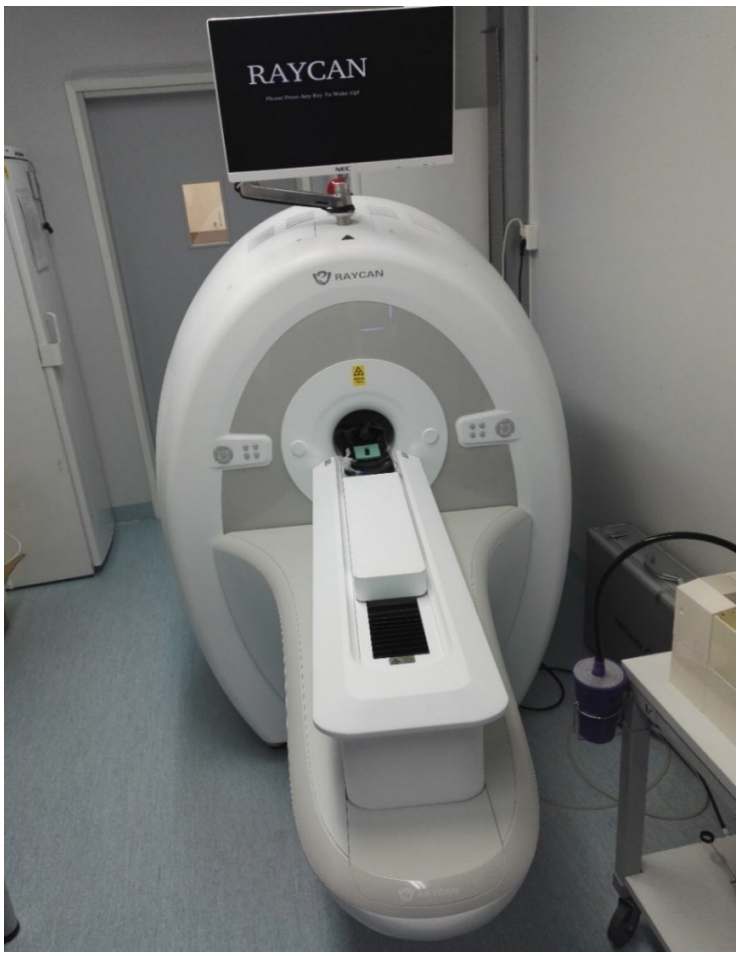

Figure 8. Raycan Trans-PET/CT X5 scanner in Turku PET Centre

The Raycan Trans-PET/CT X5 (referred to as 'Raycan' in this text) is a small-animal imaging system that uses traditional configuration of linearly placed PET and CT modules. The scanner used in this study is presented on Figure 8.

The main distinguishing feature of the Raycan PET system is wide (13 cm) transaxial FOV with short (5 cm) axial FOV and all-digital acquisition consisting of 12-block detector modules in dodecagon arrangement. Each module consists of 2×2 sub-modules with a 13×13 crystal array in every sub-module. The detector cyrstals are cerium doped lutetium-based scintillation crystals (LYSO) with 1.9×1.9 mm dimensions. Each sinogram is composed of 311 bins and 156 views.

The manufacturer-supplied technical information is presented in Table 2. The general technical details are similar to the BioCaliburn system (Wang et al., 2015).

Table 2. Manufacturer's parameters for the Raycan Trans-PET/CT X5 scanner.

PET Parameters	
Scintillation Crystal	LYSO
Crystal Size (mm)	1.9×1.9

Ring Number	26
Crystal Number/Ring	312
Bore Size (cm)	16.0
TFOV (cm)	13.0
AFOV (cm)	5.0
Sensitivity	2.0%
Spatial Resolution (mm)	1.1
Timing Resolution (ns)	1.5
Energy Resolution	15%
CT Parameters	
FOV (cm)	105
Resolution (μm)	~120
Voltage (kV)	50
Current (μA)	1000
Other	
Scan Modes	Static scan, dynamic scan, whole-body scan
Reconstructions	2D-FBP, 2D-OSEM, 3D-OSEM
Image Export	DICOM 3.0
Corrections	Normalization, attenuation, CT detector correction, geometric correction

The calibration and operation of the all-digital Raycan PET/CT scanner was done according to the manufacturer-supplied Trans-PET/CT User manual by Niu Ming dated 05.05.2017.

The Raycan system uses PiSYS software for scanner settings, quality control, scanning and image reconstructions (Figures 9 to 13).

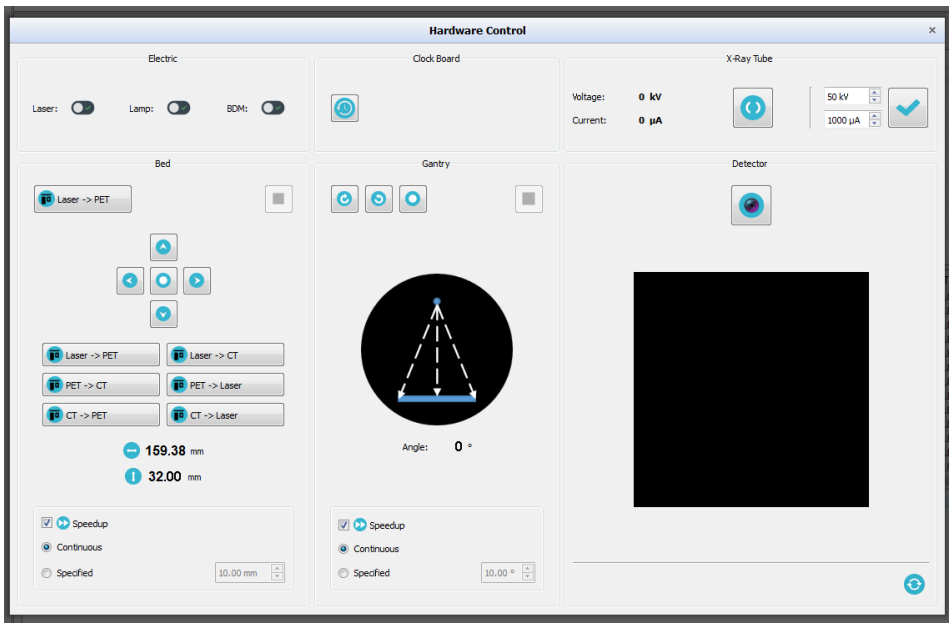

Figure 9. Hardware control window in the Raycan PiSYS software.

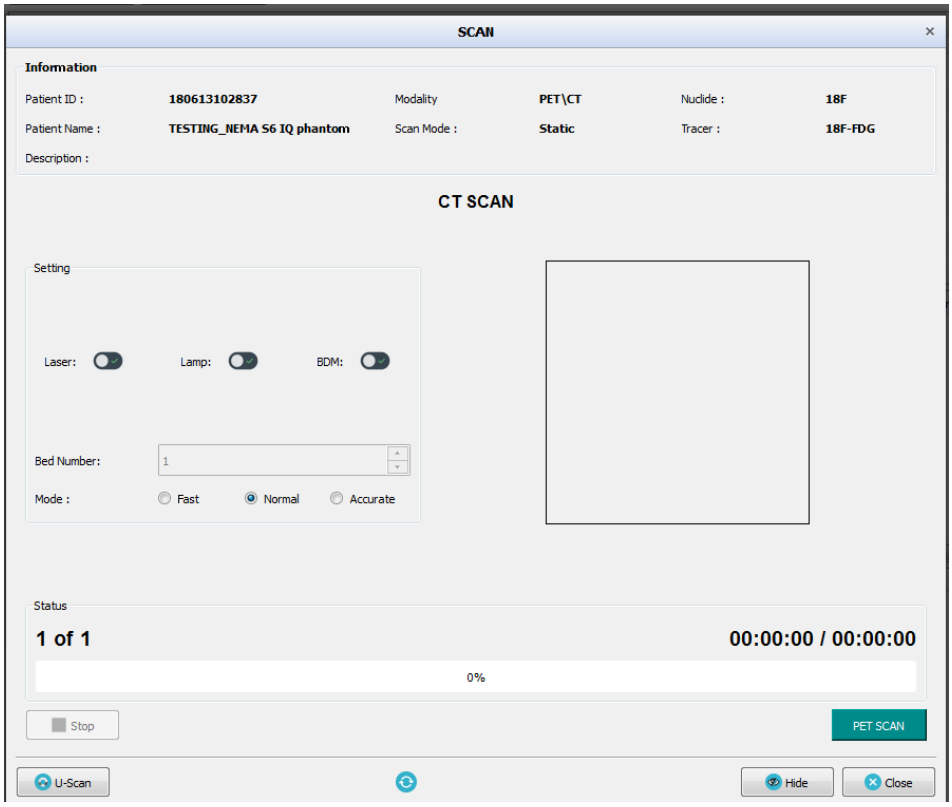

Figure 10. CT scan window in the Raycan PiSYS software.

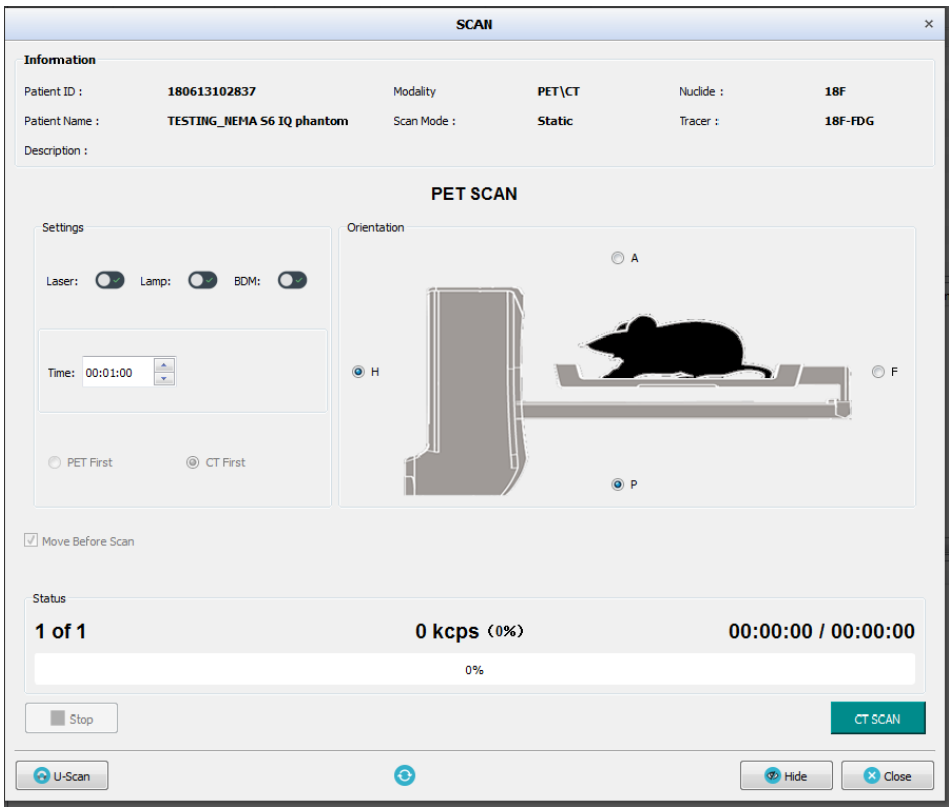

Figure 11. PET scan window in the Raycan PiSYS software.

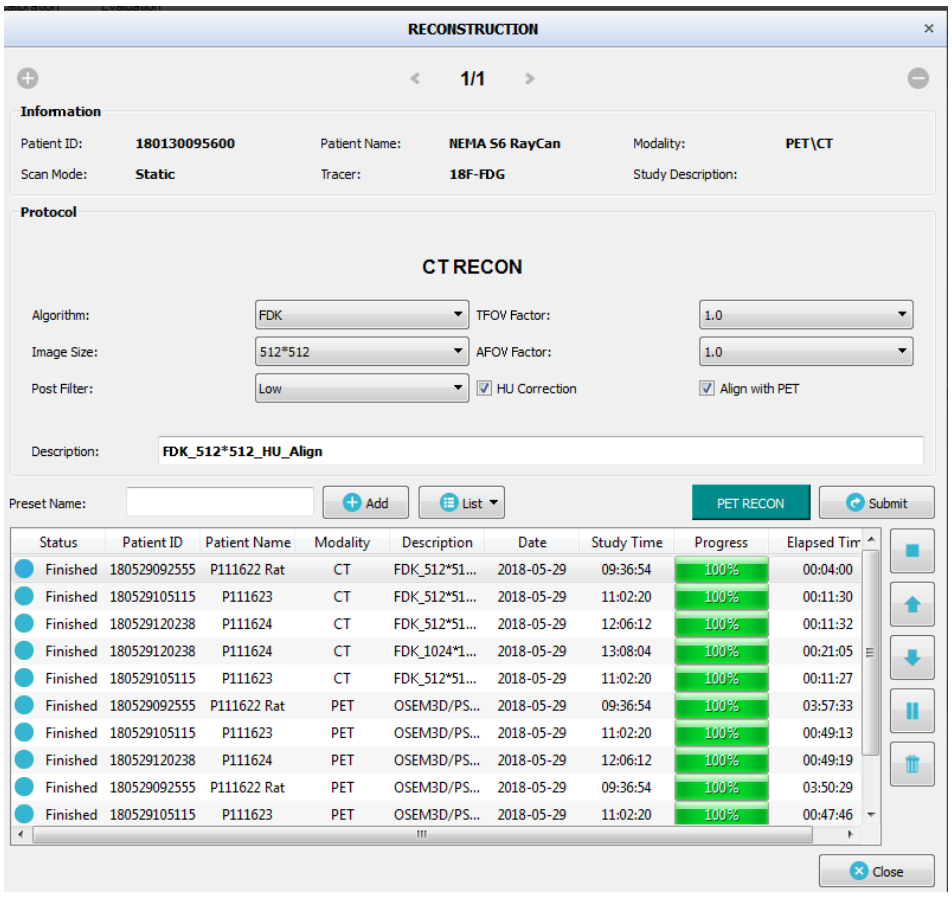

Figure 12. CT reconstruction window in the Raycan PiSYS software.

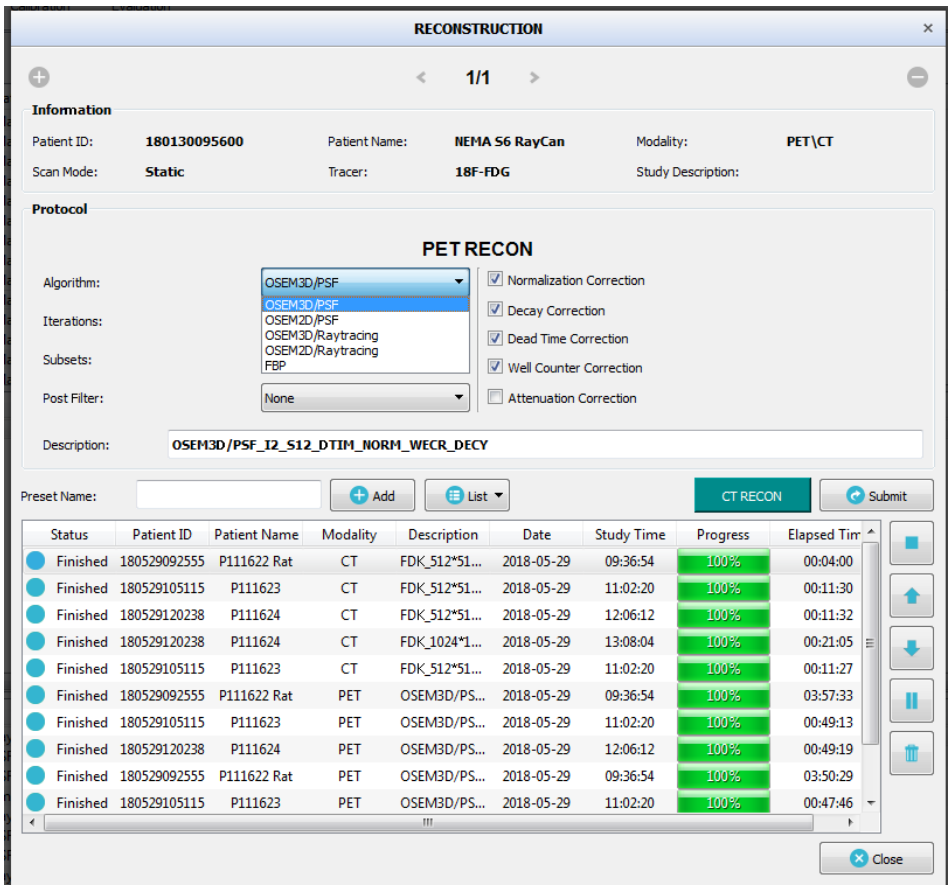

Figure 13. PET reconstruction window in the Raycan PiSYS software.

3.1.2 Inveon

NEMA Section 6 (Image Quality, Accuracy of Attenuation, and Scatter Corrections) evaluation was also performed on the Siemens Inveon PET/CT system (Siemens Medical Solutions, USA) that is being routinely used for animal studies in Turku PET Centre (Figure 14).

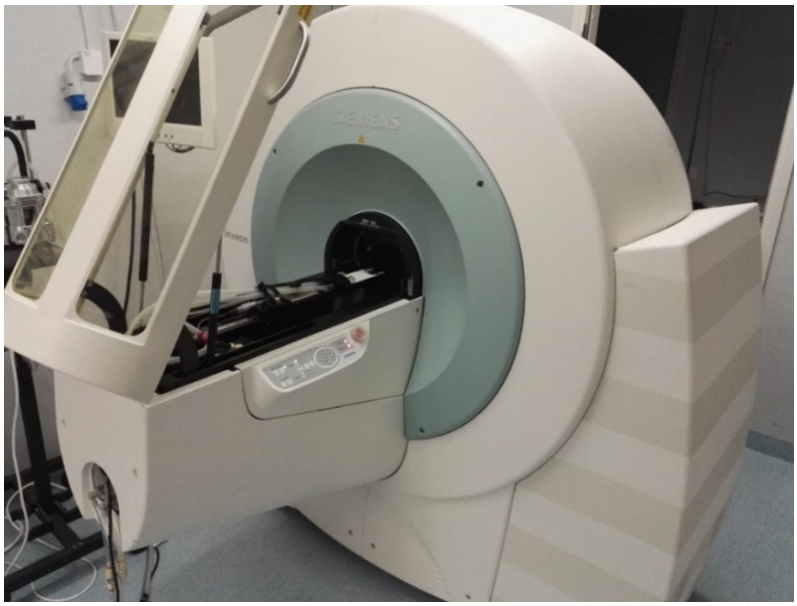

Figure 14. Siemens Inveon PET/CT scanner in Turku PET Centre.

The technical characteristics of the Siemens Inveon PET/CT are presented in Table 3.

Table 3. Manufacturer's parameters for the Siemens Inveon PET/CT scanner.

PET Parameters	
Scintillation Crystal	LSO
Crystal Size (mm)	1.5×1.5
Bore Size (cm)	12.0
TFOV (cm)	10.0
AFOV (cm)	12.7
Sensitivity	≥10%
Spatial Resolution (mm)	1.4
Timing Resolution (ns)	1.5
Energy Resolution	18%
CT Parameters	
FOV (cm)	125
Resolution (μm)	>20
Other	
Scan Modes	Static scan, dynamic scan, whole-body scan
Reconstructions	2D-FBP, 2D-OSEM, 3D-RP, 3D-OSEM+SP-MAP, 3D-OSEM+OP-MAP
Corrections	Attenuation, scatter, normalization, decay, dead time, non-uniform radial sampling

3.1.3 Molecubes

NEMA Section 6 (Image Quality, Accuracy of Attenuation, and Scatter Corrections) evaluation was additionally performed on the recently installed β-CUBE, a benchtop micro-PET scanner manufactured by MOLECUBES (Belgium). The Molecubes system is composed of separate units, X-CUBE for CT and β-CUBE for PET (Figure 15).

Figure 15. Molecubes X-(left) and β-CUBE (right) scanners in Turku PET Centre.

The detailed technical information on the Molecubes was unavailable during the time of this study, but the parameters available on official website are presented in Table 4.

Table 4. Manufacturer's parameters for the Molecubes β-CUBE scanner.

Scintillation Crystal	LYSO
Bore Size (mm)	78
AFOV (mm)	130
TFOV (mm)	72
Spatial Resolution (mm)	0.85 (with 3D OSEM)
Sensitivity	12%
Energy Resolution	12.6%
Reconstructions	FBP, 3D MLEM, 3D OSEM
Corrections	Noise regularisation, dead time, CT-based attenuation, randoms.

3.2 Section 6: Image Quality, Accuracy of Attenuation, and Scatter Corrections

3.2.1 Phantom

According to NEMA NU 4-2008 standard, Section 6 phantom is a cylinder made of polymethylmethacrylate with internal dimensions 50×30 mm. The phantom is composed of three distinct areas that are used for measuring uniformity, recovery coefficients and accuracy of corrections.

- For measuring uniformity is the empty, fillable ("hot") region of the phantom with 30×30 mm dimensions.
- For measuring recovery coefficients, the 20 mm part from one side of the phantom is solid with five radially evenly spaced rods drilled at 7 mm from the center. The rods have diameters of 1, 2, 3, 4 and 5 millimeters.
- For accuracy of corrections measurements, the lid at the "hot" region of the phantom has two chambers, 15×8 mm internal dimensions each. One is filled with air, another with non-radioactive water.

NEMA NU 4-2008 Section 6 phantom schematic is presented on Figure 16.

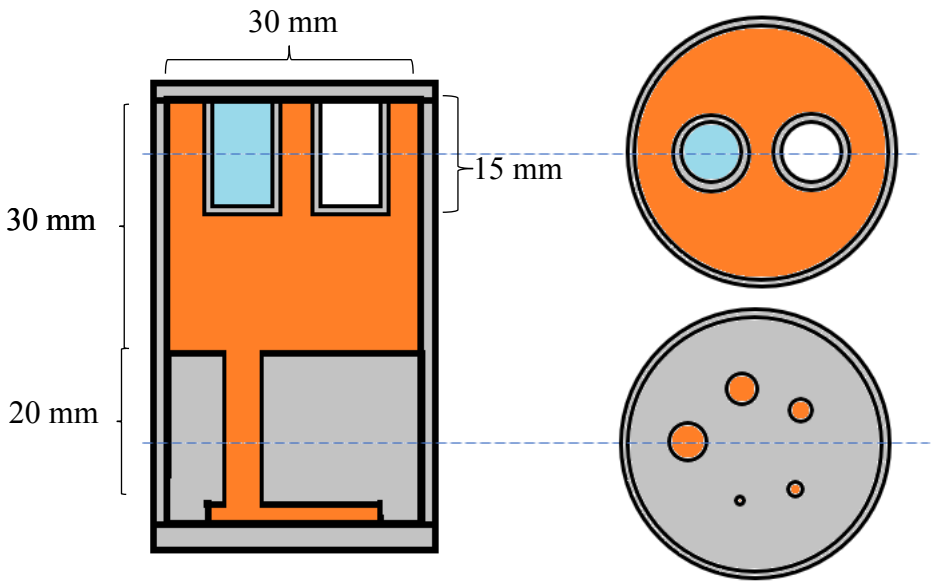

Figure 16. Schematic of NEMA NU 4-2008 Section 6 phantom.

The phantom used in this project conformed to the NEMA NU 4-2008 requirements and was supplied with Raycan PET/CT system (Figure 17).

The volume was measured by weighting the empty and water-filled phantom and calculating the weight difference. Assuming the density of pure water is 0.998774 g/ml at 21˚C, the resulting total volume was 21.79 ml.

Figure 17. RAYCAN-supplied phantom for Section 6 data acquisition used in the project.

3.2.2 Procedure

According to NEMA NU 4-2008 standard, the hot region of the phantom is to be filled with fluorodeoxyglucose (^{18}F-FDG) with the activity of 100±5% µCi. As 100 µCi is equal to 3.7 MBq, the required activity is between 3.515 and 3.885 MBq. The activity in this and experiments was measured with VDC-405 Dose Calibrator (Comecer Group, Netherlands).

Section 6 analysis was performed on three systems (Raycan, Inveon and Molecubes) and the injected activities were 3.620 (Raycan), 3.872 (Inveon) and 3.750 (Molecubes) MBq.

The measured activity of ^{18}F-FDG was injected into phantom and distilled water was added to fill the phantom and remove the air bubbles. Water-filled compartment of the phantom was also filled with distilled water.

The phantom was placed into the center of FOV, centered according to laser positioning grid, and imaged in static scan mode for 20 minutes, excluding the time needed for CT image. The Molecubes and Inveon systems have a scouting CT feature, allowing precise positioning within FOV. Raycan has no such feature and all positioning was performed according to the laser positioning grid.

3.2.3 Data Analysis

Because Section 6 of NEMA NU 4-2008 combines multiple parameters to simulate standardized imaging conditions, this test was used to determine the effect of image reconstruction settings available in evaluated systems. The results were used to define performance baselines for future tests.

Raycan PET/CT system's uniformity, recovery coefficients and accuracy of corrections were measured for filtered back projection (2D FBP) and iterative 3D OSEM (2 iterations, 12 subsets) reconstructions with PSF resolution modelling at "No" and "Low" filter (Gaussian, 3 pixel window) settings available in PiSYS. The matrix sizes were 140×140×47 and 280×280×100 and voxel sizes were 1 mm^3 and 0.5 mm^3 respectively.

The Inveon PET/CT system was also evaluated using FORE-FBP and 3D OSEM (2 iterations, 18 MAP iterations) reconstructions, with and without scatter correction. The

matrix sizes were 128×128×159 and voxel sizes were 0.48 mm^3 for both. The effect of scatter correction was evaluated as it is regularly not implemented during in-vivo imaging in Turku PET Centre.

Molecubes PET/CT system had no significant choice of options and could only be reconstructed with 3D OSEM algorithm (30 iterations). The matrix size was 192×192×384 and voxel size was 0.064 mm^3.

For measuring Uniformity and Accuracy of Corrections, VINCI 4 ("Volume Imaging in Neurological Research, Co-Registration and ROIs included") software by Max Planck Institute for Metabolism Research (Cologne, Germany) was used together with Microsoft Excel (by Microsoft Corporation, USA), and in-house MATLAB code was used for calculating Recovery Coefficients.

Uniformity was measured by drawing a 22.5×10 mm cylinder volume of interest (VOI) in the center of largest uniform hot region of the phantom (Figure 18). The VOI report tool was used to export the data and find the required average activity concentration, maximum and minimum values and percentage standard deviation (%SD) as required by NEMA NU 4-2008. Additionally, for the system comparison purposes as done by Goertzen et al. (2012), Maximum/Mean and Minimum/Mean uniformity values were calculated.

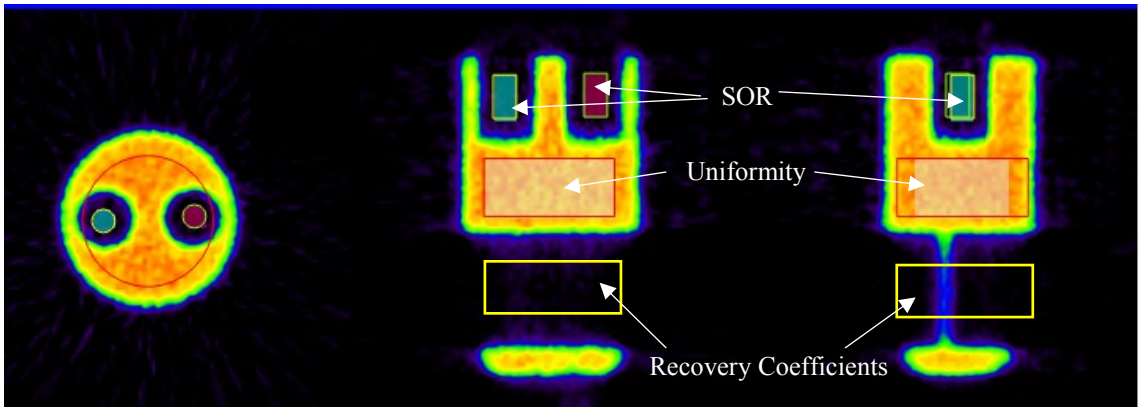

Figure 18. Image quality analysis VOI locations (Uniformity and SOR) as seen in VINCI. Recovery Coefficients VOI drawn separately.

Recovery Coefficients were calculated by averaging the slices within central 10 mm part of the rods (Figure 18). On the resulting one low-noise slice, circular regions of interest (ROIs) were drawn around each rod, with the diameter of ROIs being double the actual

rod diameter. In-house MATLAB code was used to find within ROIs the pixels with maximum values. The locations of these pixels were used to plot the activity values through the original central 10 mm of the rods (Figure 19).

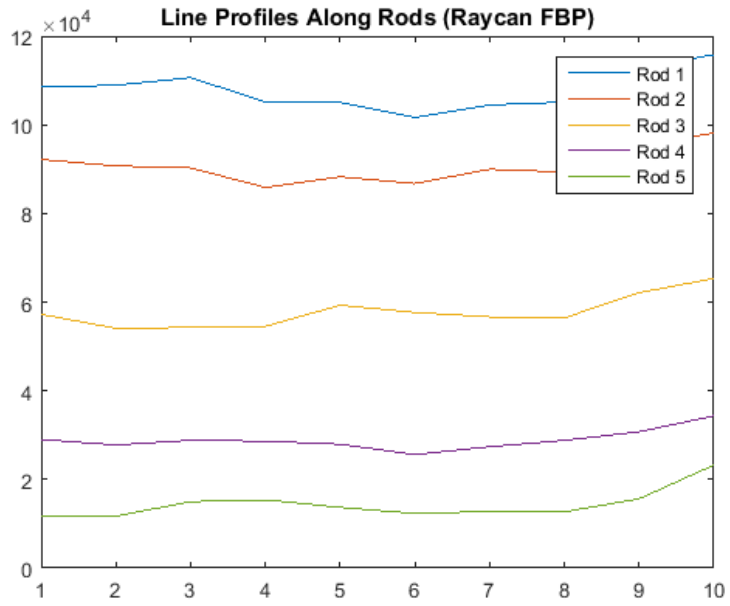

Figure 19. Line profiles through central 10 mm of the rods as seen in MATLAB.

The values from each line profile were divided by mean uniform activity concentration and used to calculate the mean and standard deviation for each rod.

$$\%STD_{RC} = 100 \times \sqrt{\left(\frac{SD_{lineprofile}}{Mean_{lineprofile}}\right)^2 + \left(\frac{SD_{background}}{Mean_{background}}\right)^2} \quad 1.$$

Accuracy of Corrections was measured by drawing 7.5×4 mm cylinders in the center of cylinders that were filled with air and non-radioactive water (Figure 11). The spill-over ratio (SOR) was calculated as a ratio of the mean in each cold cylinder (air and water) to the mean in uniform region. %SD of SOR of cylinder *i* was calculated as

$$\%SD_{SORi} = 100 \times \sqrt{\left(\frac{SD_i}{Mean_i}\right)^2 + \left(\frac{SD_{uniform\ region}}{Mean_{uniform\ region}}\right)^2} \quad 2.$$

3.3 Section 5: Sensitivity

3.3.1 Phantom

According to the NEMA NU 4-2008 standard, the phantom used in Sections 5 and 3 is the same. It is composed of 22-Na point source not larger than 0.3×0.3×0.3 mm embedded in an acrylic cube with external side dimensions 10×10×10 mm.
The phantom used in this study (Figure 20) was supplied by Eckert & Ziegler (Germany), with catalogue number MMS09-022-10U, where MMS09 denotes the capsule type. The activity at the moment of production was 9.874 μCi = 0.365338 MBq. By the time of the study, the source activity (A_{cal}) had decayed to 0.321 MBq.

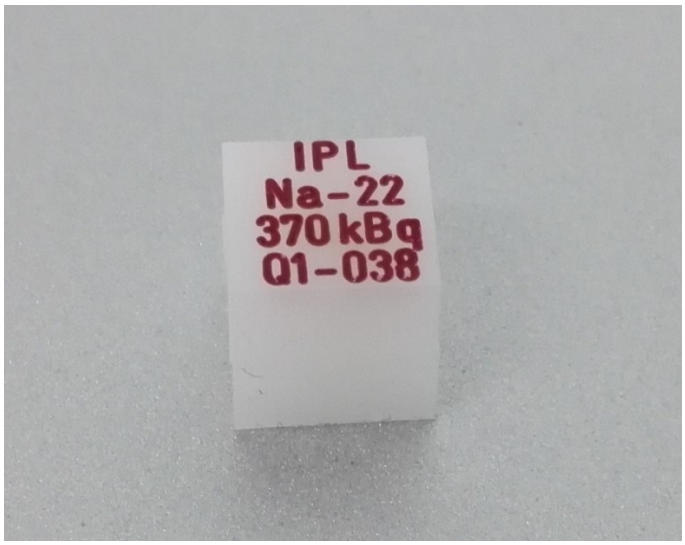

Figure 20. Phantom used for Sections 5 and 3 data acquisition.

3.3.2 Procedure

In accordance with NEMA NU 4-2008 guidelines, the acquisition times are to be sufficient for collecting at least 10 000 true events. Due to the system limitation and ease of operation, the decided acquisition duration (T_{acq}) was 1 minute (60 seconds). That T_{acq} was used for all measurements in this section.

First, the background PET scan was acquired without activity. Subsequently, the phantom was placed close to the far end of the bed to ensure it could reach the whole axial FOV. The bed height for this phantom was set as 45.0 mm. After centering the phantom in FOV according to laser positioning grid, the PET data were collected. Afterwards, the bed motion control was used to axially move the phantom and acquire PET data in 0.5 mm

steps to one end of PET FOV. Then the phantom was returned to the center and stepped to the other end of the FOV. The graphic representation of the imaging plan is shown on Figure 21.

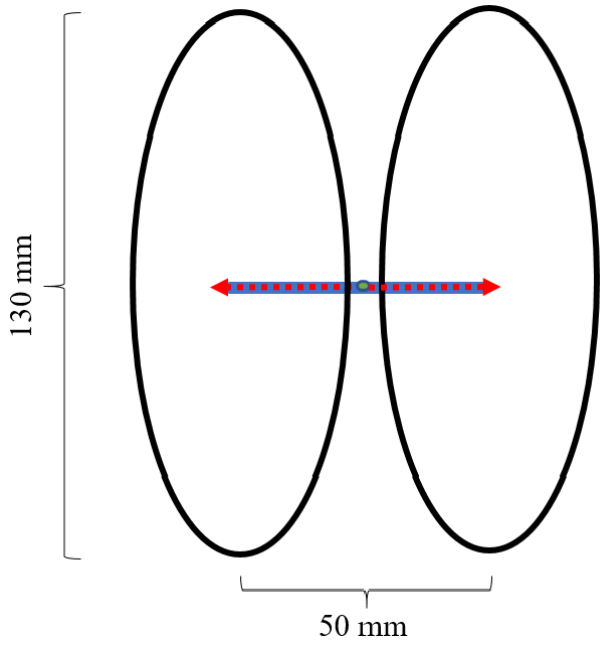

Figure 21. Sketch of the Section 5 acquisition procedure within Raycan PET FOV. Data acquisition directions marked with red.

3.3.3 Data Analysis

NEMA NU 4-2008 states that for Sensitivity evaluation: "single slice rebinning (SSRB) method has to be used to assign counts in oblique lines-of response (LORs) to the image slice where the LOR crosses the scanner axis, so that each slice is represented by one sinogram. For each row of the sinogram (angle), the highest value shall be located, and all pixels greater than 1 cm from this peak shall be set to zero. The total of all pixels in the sinogram shall then be summed to form the total counts in that slice".

The NEMA NU 4-2008 standard has been intended to analyze the sinogram data in 2D format, possibly due to historical reasons. The sensitivity evaluation was performed with data rebinned to 2D sinograms with SSRB and with 3D michelograms data available in the systems. Additionally, due to the noisy edges of Raycan-produced SSRB sinograms, the masks were created and centered according to axial line (Figure 22). All calculations were performed using in-house MATLAB code.

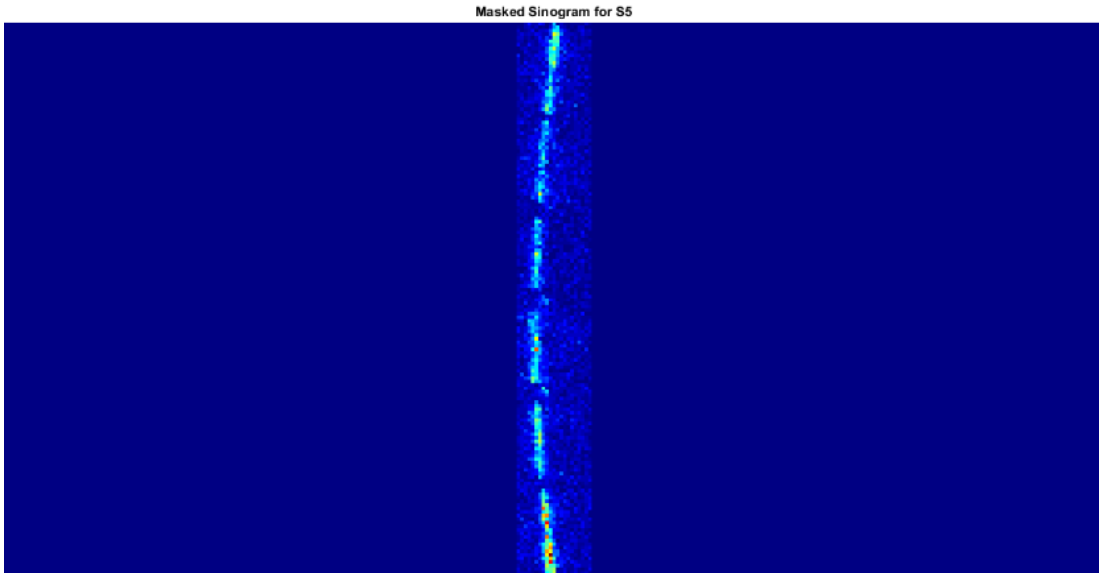

Figure 22. Masked sinogram from MATLAB for Sensitivity evaluation.

As stated in NEMA NU 4-2008, no corrections for scattered or random events were applied. For each measurement (i), the count rate (R_i), in counts per second was calculated by dividing the total counts per slice (from masked sinogram) by the acquisition duration (T_{acq} = 60 sec).

Background count rate ($R_{B,i}$) was calculated by applying the same sinogram mask to the background scan and dividing the sinogram sum of each slice by background acquisition duration.

Sensitivity (counts/sec/Bq^{-1}) was calculated using the formula:

$$S_i = \left(\frac{R_i - R_{B,i}}{A_{cal}}\right) \quad 3.$$

Absolute sensitivity (%) was calculated using the formula:

$$S_{A,i} = \frac{S_i}{0.9060} \times 100 \quad 4.$$

Because the Raycan axial FOV is 50 mm, shorter than even assumed mouse length, all total sensitivity calculations were done with these two formulas:

$$S_{tot} = \sum_{\substack{all \\ i}} S_i \quad 5.$$

$$S_{A,tot} = \sum_{\substack{all \\ i}} S_{A,i} \quad 6.$$

3.4 Section 4: Scatter Fraction, Count Losses, and Random Coincidence Measurements

3.4.1 Phantom

According to NEMA NU 4-2008 standard, the suitable phantoms are produced from solid high-density polyethylene (density 0.96±0.1 g/cm^3). Because of the scanner limitations, only mouse- and rat-sized phantoms were used (shown on Figure 23), excluding the monkey-sized phantom.

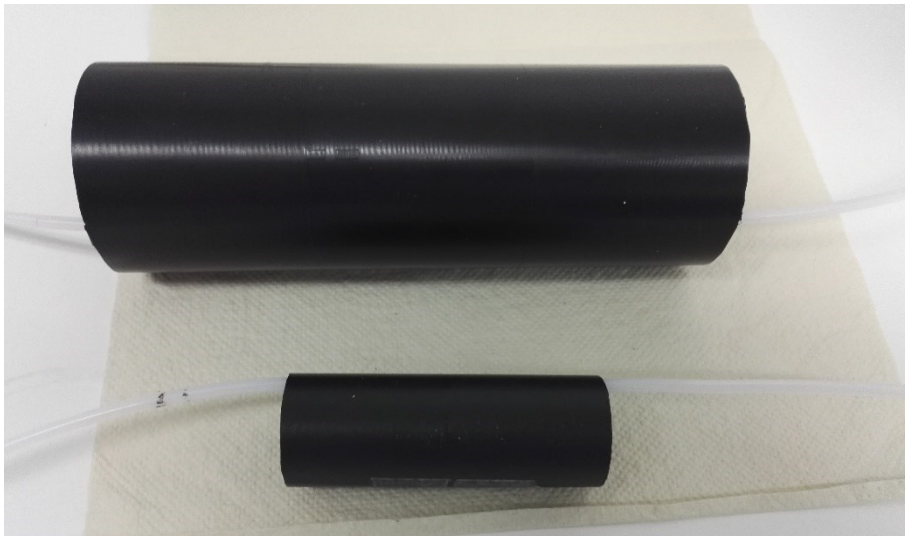

Figure 23. NEMA specified rat-sized (above) and mouse-sized (below) phantoms for Section 4 data acquisition.

The mouse-sized phantom is a cylinder with the dimensions of 70×25 mm. The rat-sized phantom is a cylinder with the dimensions of 150×50 mm. Both phantoms have a 3.2 mm diameter cylindrical bore drilled lengthwise through the phantom at the radial distance of 10 mm (mouse) and 17.5 mm (rat).

Clear flexible tubes with 3.2 mm external diameter are used to hold enough 18-F or 11-C activity to reach peak true count rate and noise equivalent count rate. The volume is enough to fill the tubes 10 mm less than the length of the corresponding phantom.

The phantoms used in this study had an active volume of 0.11 ml and 0.22 ml for mouse- and rat-sizes respectively. The used isotope was 18-F.

NEMA NU 4-2008 recommends using manufacturer-provided activity. RAYCAN suggested to use the activity of 60 MBq. However, after two scans, the suggested activity was proven to be insufficient and acquisitions were redone with minimum activity of 100 MBq. The rat-sized phantom had the injected activity of 123.71 MBq and mouse-sized had 106.54 MBq.

3.4.2 Procedure

The phantom was axially and transaxially centered according to laser positioning grid, with line source positioned to be closest to the bed. The bed height for rat-sized phantom was 19.50 mm and for mouse-sized 32.00 mm. The phantom placement schematic from NEMA NU 4-2008 is shown on Figure 24. To measure system's intrinsic activity, a phantom scan without activity was performed for 5 minutes before each scan session.

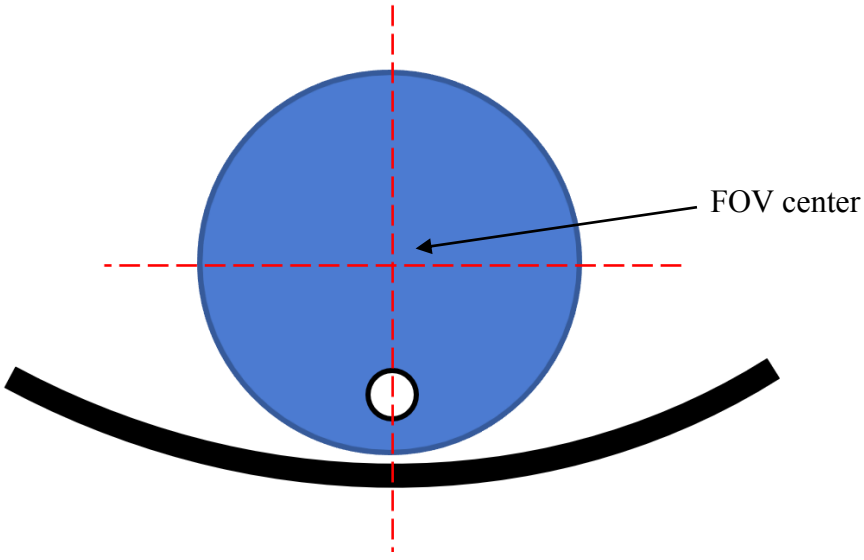

Figure 24. Section 4 phantom placement schematic.

NEMA NU 4-2008 also suggests using manufacturer-provided acquisition durations and time points. RAYCAN provided the following acquisition protocol:

0-1h: 5 minute acquisitions every 7 minutes (leaving 2 minutes between scans)

1-2h: 5 minute acquisitions every 10 minutes

2-5h: 5 minute acquisitions every 25 minutes

5+h: 5 minute acquisitions every 35 minutes

3.4.3 Data Analysis

As stated in NEMA NU 4-2008, the collected data were not corrected. Similar to Section 5 (Sensitivity), the data were processed using both 2D sinograms rebinned with SSRB and the original 3D michelograms. All the analysis was done with in-house MATLAB code.

In each sinogram (i) of each acquisition (j), all pixels further than 8 mm from the edges of the phantom were set to zero. In the sinogram, for each projection angle (ϕ), the pixel with highest value was found and determined as the center of LOR. Every projection was shifted to align the highest value pixel with the central pixel of the sinogram. Then, a sum projection was produced, where a pixel in sum projection was the sum of the pixels in each angular projection that had the same radial offset as the pixel in the sum projection, according to the following formula:

$$C(r)_{i,j} = \sum_{\phi} C(r - r_{max}(\phi), \phi)_{i,j} \quad 7.$$

Where: r – pixel number in projection

ϕ – projection number in sinogram (row)

$r_{max}(\phi)$ – location of the highest value pixel in projection ϕ.

From the sum projection (Figure 25), at the 7 mm left and right offsets from the maximum pixel at the center of the sinogram, the pixel intensities (counts) $C_{L,i,j}$ and $C_{R,i,j}$ were obtained. There, linear interpolation from maximum pixel to ±7 mm points was used to find the pixel values. The average of $C_{L,i,j}$ and $C_{R,i,j}$ pixel values was multiplied by the number of pixels within the ±7 mm area.

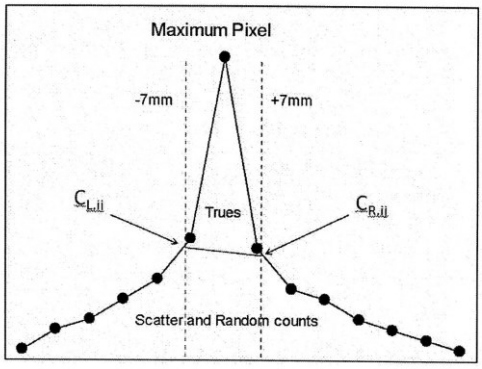

Figure 4-2
INTEGRATION OF BACKGROUND COUNTS INSIDE AND OUTSIDE 14 MM STRIP

Figure 25. Sum projection sketch adapted from NEMA NU 4-2008.

The result was added to the counts in the pixels outside this area, which gave the number of random plus scattered events counts $C_{r+s,i,j}$ for the slice *i* of the acquisition *j*.

The total event count ($C_{TOT,i,j}$) was the sum of all pixels in the sum projection of slice *i* of the acquisition *j*. Average activity ($A_{ave,j}$) was calculated for each acquisition *j* with formula:

$$A_{ave} = \frac{A_0}{ln2}\left(\frac{T_{1/2}}{T_{acq}}\right)\left\{1 - exp\left(\frac{-T_{acq}}{T_{1/2}}ln2\right)\right\} \quad 8.$$

Where: A_0 – activity at the beginning of acquisition

$T_{1/2}$ – radionuclide half-life

T_{acq} – duration of acquisition

Total event rate $R_{TOT,i,j}$ for each acquisition *j* was calculayed according to formula:

$$R_{TOT,i,j} = \frac{C_{TOT,i,j}}{T_{acq,j}} \quad 9.$$

Where: $T_{acq,j}$ – acquisition duration (= 300 sec)

The system total event rate was calculated as a sum of all $R_{TOT,i,j}$ from all slices *i*.

True event rate $R_{t,i,j}$ for the slice *i* of the acquisition *j* was calculated with formula:

$$R_{t,i,j} = \frac{(C_{TOT,i,j} - C_{r+s,i,j})}{T_{acq,j}} \quad 10.$$

Where: $T_{acq,j}$ – acquisition duration

The system true event rate was calculated as a sum of all $R_{t,i,j}$ from all slices *i*.

Because Raycan system does not estimate random coincidences, the random event rate was calculated according to formula:

$$R_{r,i,j} = R_{TOT,i,j} - \left(\frac{R_{t,i,j}}{1 - SF_i}\right) \quad 11.$$

The system random event rate was calculated as a sum of all $R_{r,i,j}$ from all slices *i*.

For calculating scatter fraction, last 5 acquisitions (*j'*) were used. The scatter fraction for each slice (SF_i) is calculated by using the formula:

$$SF_i = \frac{\sum_{j'} C_{r+s,i,j'}}{\sum_{j'} C_{TOT,i,j'}} \quad 12.$$

Scattered event rate (Rs,i,j) for slice *i* was calculated with formula:

$$R_{s,i,j} = R_{TOT,i,i} - R_{t,i,j} - R_{r,i,j} - R_{int,i} \quad 13.$$

Where: R_{int} – intrinsic activity

The system scattered event rate was calculated as a sum of all $R_{s,i,j}$ from all slices *i*.

Due to Raycan using LYSO intrinsically radioactive detectors, for calculating system scatter fraction for acquisition $_j$ (SF_j) the used formula was:

$$SF_j = \frac{R_{s,j}}{R_{t,j} + R_{s,j}} \quad 14.$$

The system scatter fraction was calculated from last 5 acquisitions (*j'*) according to formula:

$$SF = \sum_{j'} SFj' = \frac{\sum_i \sum_{j'} R_{s,i,j'}}{\sum_i \sum_{j'} R_{t,i,j'} + \sum_i \sum_{j'} R_{s,i,j'}} \quad 15.$$

Because Raycan does not use direct random event subtraction, noise equivalent count rate ($R_{NEC,i,j}$) of slice *i* of the acquisition *j* was calculated as follows:

$$R_{NEC,i,j} = \frac{R^2{}_{t,i,j}}{R_{TOT,i,j}} \quad 16.$$

For system comparison, trendline for NECR profiles was found with MS Excel and used to deduce the NECR at 3.7 MBq (mouse phantom) and 10 MBq (rat phantom) remaining activities.

3.5 Section 3: Spatial Resolution

3.5.1 Phantom

The phantom for Section 3 was the same as the one used for Section 5 (Part 3.3.1), a 22-Na point source with 0.3×0.3×0.3 mm dimensions embedded into 10×10×10 mm acrylic cube.

3.5.2 Procedure

Following NEMA NU 4-2008 regulations, the phantom was centered in PET FOV according to laser positioning grid, with bed height set to 45.0 mm.

Bed motion control was used to manage the axial position of the phantom and static PET scan was performed at the center of FOV and ¼ of distance of axial FOV (12.5 mm from center) towards both ends. At each of these three axial points, the phantom was also imaged at 5, 10, 15 and 25 mm offsets from axial center of FOV. The total number of acquisitions was 15. The graphic representation of the procedure is shown on Figure 26. To obtain 10^5 prompt counts per measurement, acquisition durations used were 1 minute each.

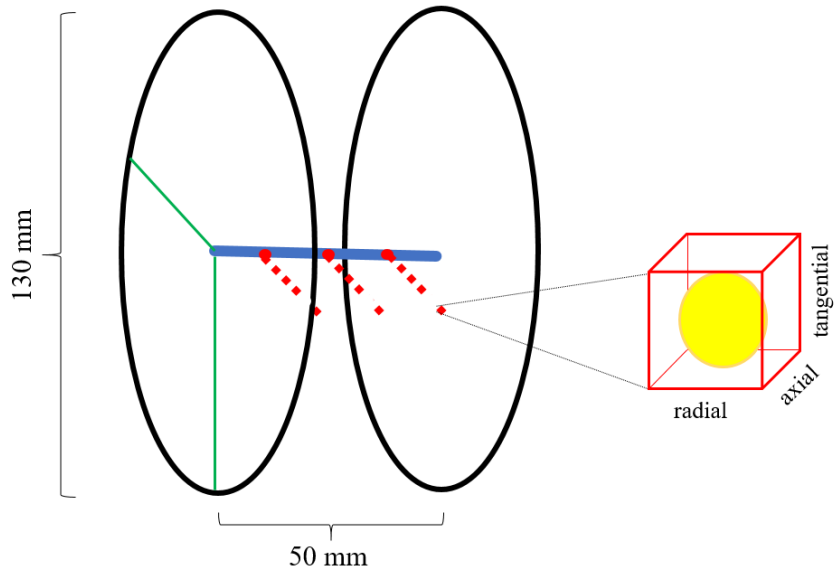

Figure 26. Sketch of the Section 3 acquisition procedure within Raycan PET FOV

3.5.3 Data Analysis

Spatial resolution data were reconstructed as 2D FBP using SSRB and no smoothing. One-dimensional response functions were created by forming lines through the peak of the image volume towards three orthogonal directions (axial, radial, tangential; Figure 19). Full width half maximum (FWHM) and full width tenth maximum (FWTM) were determined as horizontal difference between pixels at half (for FWHM) and tenth (for FWTM) of the response functions (Figures 27 and 28).

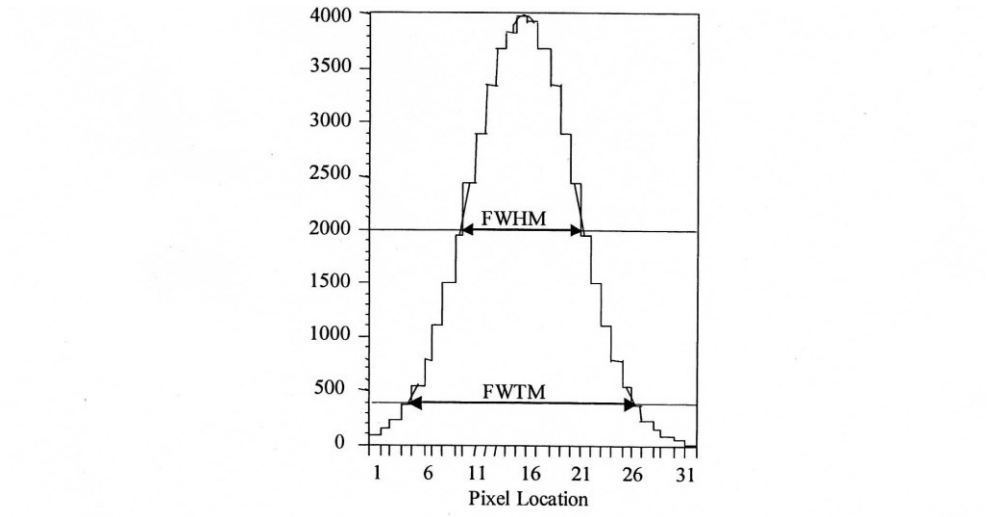

Figure 27. Typical response function with FWHM and FWTM locations. Adapted from NEMA NU 4-2008.

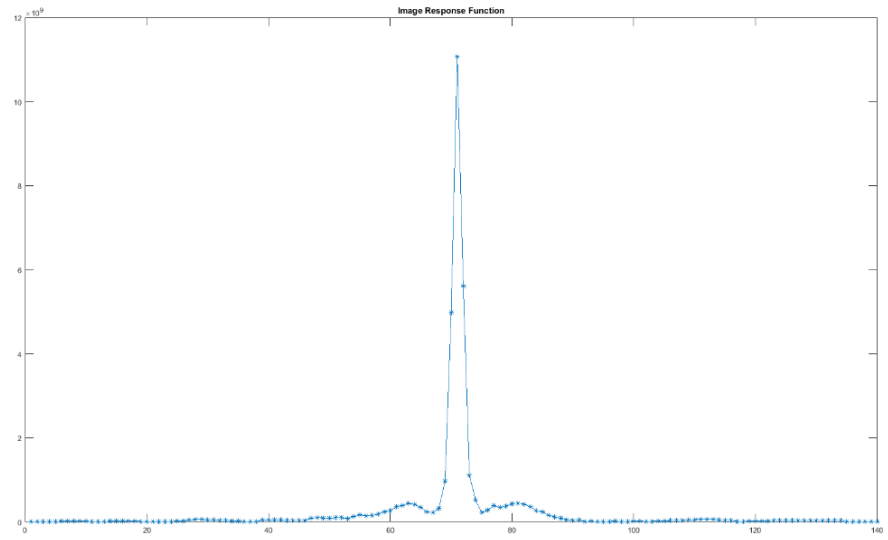

Figure 28. One of the Raycan resolution point response functions obtained in MATLAB.

The maximum value was determined as the maximum value of the response function as opposed using parabolic fit of the maximum value and two adjacent points and then using the fitted value to determine the maximum. Values were converted to millimetres by multiplication with pixel size (1 mm) to 2 decimal places.

3.6 Live Animal Imaging

3.6.1 Animals

Two male rats (Rat 1 and Rat 2) of BDIX strain (Charles River Laboratories, USA), both 7 weeks old were imaged on the Raycan and Inveon systems. Animals were put under isoflurane anaesthesia at 4-5% concentration for induction and 1-2% concentration for maintenance. The weight of Rat 1 was 183.7 grams and Rat 2 was 175.7 grams by the time of the experiment.

All animal experiments were approved by the national Animal Experiment Board in Finland and the Regional State Administrative Agency for Southern Finland (License number, ESAVI/3116/04.10.07/2017) and were conducted in accordance with the relevant European Union directive.

3.6.2 Imaging Protocol

Via lateral tail vein cannula, Rat 1 was injected 11.12 MBq and Rat 2 was injected 11.40 MBq of ^{18}F-FDG.

After injection, the heart region was centered in PET FOV and imaged for 60 minutes in PET dynamic scan mode. Afterwards, images for anatomical localization and attenuation correction were acquired with 6 minute CT scans.

After the 1st scan, the animals were switched between the PET/CT systems and whole-body static PET scans were performed for 30 minutes, with additional CT scan in the Raycan for 18 minutes and in the Inveon for 6 minutes.

The animals were switched again between scanners and the whole body static PET scans and CT were repeated.

The sequence for both rats was as follows:
Rat 1 – Raycan dynamic scan → Inveon static scan → Raycan static scan
Rat 2 – Inveon dynamic scan → Raycan static scan → Inveon static scan

3.6.2 Data Analysis

Images were reconstructed with 3D OSEM (2 iterations, 18 MAP iterations) algorithm on the Inveon and 3D OSEM (2 iterations, 12 subsets) with PSF on the Raycan. Volumes of interest (VOIs) were drawn with Carimas software (Turku PET Centre, Finland) at the locations of the lung, liver and muscle and 4 regions of interest (ROIs) were drawn on four adjacent slices of the myocardium of the left ventricle (heart muscle) (Figure 29).

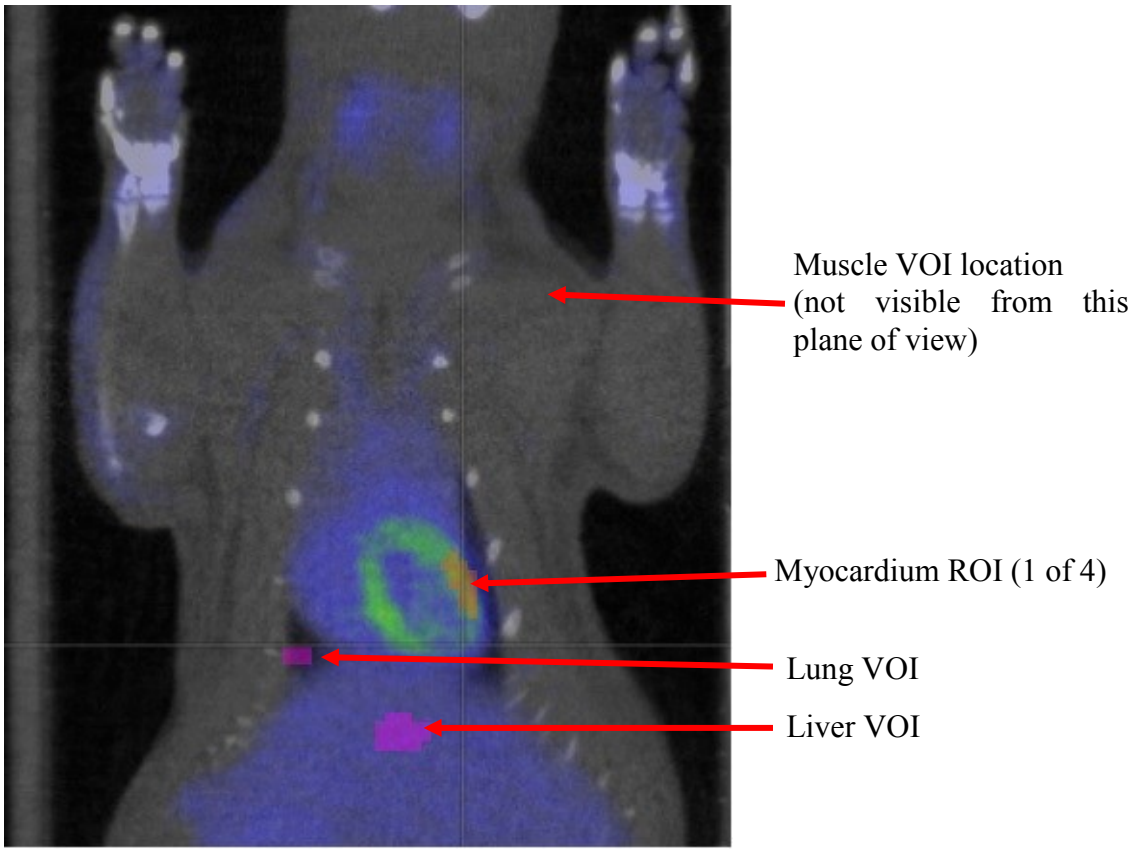

Figure 29. ROI and VOI locations. From Rat 1 dynamic scan image viewed in Carimas.

The radioactivity concentration data were exported and analyzed in Microsoft Excel. Standardized uptake values (SUVs) were calculated for all time points, with static scan values additionally decay corrected to the start of the first dynamic scans. SUVs were calculated according to the formula:

$$SUV = \frac{Radioactivity\ concentration\ (kBq/ml)}{Injected\ dose\ (KBq)/Animal\ weight\ (g)} \quad 17.$$

4 Results

4.1 Results for Section 6: Image Quality, Accuracy of Attenuation, and Scatter Corrections

4.1.1 NEMA Standard Report

Tables 5 to 13 present the results of uniformity, recovery coefficients and accuracy of corrections tests as standardized in NEMA NU 4-2008.

The parameter of Uniformity is compared according to resulting %SD. The lower %SD value means less deviation between the highest and the lowest values within the area, thus showing higher (or better) uniformity. The Raycan results from Table 5 show that low filter settings produce similar Uniformity values for both FBP and OSEM algorithms and numerically, is best among tested systems. All the Inveon (Table 6) and Molecubes (Table 7) reconstructions have comparable uniformity %SD values that are only ~1-2% worse than those produced by the Raycan.

Table 5. NEMA NU 4-2008 Section 6 Uniformity reports for the Raycan.

Raycan				
Report for Uniformity Test				
	Mean (Bq)	Maximum (Bq)	Minimum (Bq)	%SD
FBP Low Filter	158634	182181	136730	4.32
FBP No Filter	159014	264647	67756	19.19
3D OSEM Low Filter	156039	187141	135296	4.59
3D OSEM No Filter	156047	198735	127926	5.59

Table 6. NEMA NU 4-2008 Section 6 Uniformity reports for the Inveon.

Inveon				
Report for Uniformity Test				
	Mean (Bq)	Maximum (Bq)	Minimum (Bq)	%SD
FBP, No Scatter Correction	162647	196784	125372	5.47
FBP, With Scatter Correction	157581	191919	120463	5.78
3D OSEM, No Scatter Correction	173080	221552	124854	7.12
3D OSEM, With Scatter Correction	167666	205269	128159	6.14

Table 7. NEMA NU 4-2008 Section 6 Uniformity report for the Molecubes.

Molecubes				
Report for Uniformity Test				
	Mean (Bq)	Maximum (Bq)	Minimum (Bq)	%SD
3D OSEM	206720	269536	154491	6.81

Recovery coefficients test indicates the ability of the system to recover the absolute activity concentration in targets of different sizes, and thus reflects the spatial resolution of the system as well. The ideal result being equal to 1.00 for all rods means perfect recovery of activity compared to the uniform region of the phantom. %SD of recovery coefficients were calculated according to Formula 1 in Part 3.2.3. Table 8 shows that without filter, the Raycan produced better recovery coefficients than with, but still could not reach the level of the Inveon (Table 9). Both the Raycan and Inveon produced best results with iterative reconstruction algorithms, but had a RC peak at 4 mm rods with values dropping again for the 5 mm rods. The results for the Molecubes (Table 10) were more stable between rod sizes. Notably, the Molecubes showed highest RC values among tested systems for small rod sizes, but the values dropped to the level of the Inveon FBP/Raycan OSEM results for 4-5 mm rods

Table 8. NEMA NU 4-2008 Section 6 Recovery Coefficient reports for the Raycan.

Report for Recovery Coefficient Test										
Raycan FBP Low Filter										
Rods	1 mm	%SD	2 mm	%SD	3 mm	%SD	4 mm	%SD	5 mm	%SD
RC	0.09	0.23	0.18	0.20	0.36	0.19	0.57	0.19	0.67	0.20
Raycan FBP No Filter										
Rods	1 mm	%SD	2 mm	%SD	3 mm	%SD	4 mm	%SD	5 mm	%SD
RC	0.14	0.34	0.27	0.29	0.47	0.27	0.71	0.24	0.76	0.22
Raycan 3D OSEM Low Filter										
Rods	1 mm	%SD	2 mm	%SD	3 mm	%SD	4 mm	%SD	5 mm	%SD
RC	0.10	0.10	0.39	0.08	0.73	0.08	0.93	0.06	0.87	0.07
Raycan 3D OSEM No Filter										
Rods	1 mm	%SD	2 mm	%SD	3 mm	%SD	4 mm	%SD	5 mm	%SD
RC	0.11	0.15	0.48	0.12	0.82	0.11	0.98	0.07	0.88	0.09

Table 9. NEMA NU 4-2008 Section 6 Recovery Coefficient reports for the Inveon.

Report for Recovery Coefficient Test										
Inveon FBP No Scatter Correction										
Rods	1 mm	%SD	2 mm	%SD	3 mm	%SD	4 mm	%SD	5 mm	%SD
RC	0.15	0.16	0.41	0.07	0.67	0.07	0.80	0.06	0.88	0.06
Inveon FBP With Scatter Correction										
Rods	1 mm	%SD	2 mm	%SD	3 mm	%SD	4 mm	%SD	5 mm	%SD
RC	0.14	0.18	0.40	0.07	0.67	0.07	0.81	0.06	0.89	0.06
Inveon 3D OSEM No Scatter Correction										
Rods	1 mm	%SD	2 mm	%SD	3 mm	%SD	4 mm	%SD	5 mm	%SD
RC	0.19	0.11	0.57	0.09	0.88	0.08	0.94	0.08	0.93	0.08
Inveon 3D OSEM With Scatter Correction										
Rods	1 mm	%SD	2 mm	%SD	3 mm	%SD	4 mm	%SD	5 mm	%SD
RC	0.16	0.13	0.57	0.08	0.89	0.07	0.97	0.07	0.95	0.07

Table 10. NEMA NU 4-2008 Section 6 Recovery Coefficient report for the Molecubes.

Report for Recovery Coefficient Test										
Molecubes 3D OSEM										
Rods	1 mm	%SD	2 mm	%SD	3 mm	%SD	4 mm	%SD	5 mm	%SD
RC	0.20	0.11	0.61	0.10	0.81	0.10	0.82	0.09	0.88	0.10

Spill-over ratios show the effectiveness of data corrections implemented in the systems, such as attenuation, randoms and scatter correction. Low SORs are considered to be better. %SD of SOR were calculated according to Formula 2 in Part 3.3.3. Raycan results from Table 11 show that SOR values for FBP reconstructions were significantly better than for OSEM, without much effect from the filter. The Inveon (Table 12) produces best results with OSEM algorithm, with scatter correction option noticeably affecting only FBP reconstruction. Overall, the Inveon produced best SOR results among all tested systems, with the Molecubes (Table 13) showing high similarity between water and air region SORs, but with values being generally similar to the Raycan.

Table 11. NEMA NU 4-2008 Section 6 Accuracy of Corrections reports for the Raycan.

Raycan				
Report for Accuracy of Corrections				
	Region	SOR	SOR as %	%SD
FBP Low Filter	Water	968.06:11331	8.54	33.90
	Air	13910.15:79317	17.54	24.96
FBP No Filter	Water	12781.5:159014	8.04	108.61
	Air	25941.9:159014	16.31	69.83
3D OSEM Low Filter	Water	22261.5:156039	14.27	21.09
	Air	11831.17:52013	22.75	21.25
3D OSEM No Filter	Water	22284.1:156047	14.28	15.98
	Air	34841.7:156047	22.33	15.64

Table 12. NEMA NU 4-2008 Section 6 Accuracy of Corrections reports for the Inveon.

Inveon				
Report for Accuracy of Corrections				
	Region	SOR	SOR as %	%SD
FBP No Scatter Correction	Water	2913.48:162647	1.79	260.83
	Air	3521.36:162647	2.17	212.72
FBP with Scatter Correction	Water	-0.004084693	-0.41	1165.59
	Air	496.007:157581	0.31	1467.96
3D OSEM No Scatter Correction	Water	26.055125:21635	0.12	379.65
	Air	11.08155:43270	0.03	734.25
3D OSEM With Scatter Correction	Water	211.935:167666	0.13	235.08
	Air	35.16485:83833	0.04	289.48

Table 13. NEMA NU 4-2008 Section 6 Accuracy of Corrections reports for the Molecubes.

Molecubes				
Report for Accuracy of Corrections				
	Region	SOR	SOR as %	%SD
3D OSEM	Water	12.0997:103.36	11.71	17.11
	Air	21.3885:206.72	10.35	14.64

Figures 30 to 34 show the images used for Section 6 evaluation. The image quality was compared visually.

Images produced by Raycan (Figures 30 and 31) show quite good image quality. However, 2D FBP image without filtering has striped appearance due to the use of single-slice rebinning (SSRB) method used in reconstruction. Overall, smaller details are better visible in images produced by 3D OSEM reconstruction, with low filter making the objects look more uniform and definable. The visible spill-over which has been evaluated to be higher in air-filled cylinder, can be seen in all images. Additionally, in transaxial views of all images, the smallest 1 mm rods remain indistinguishable.

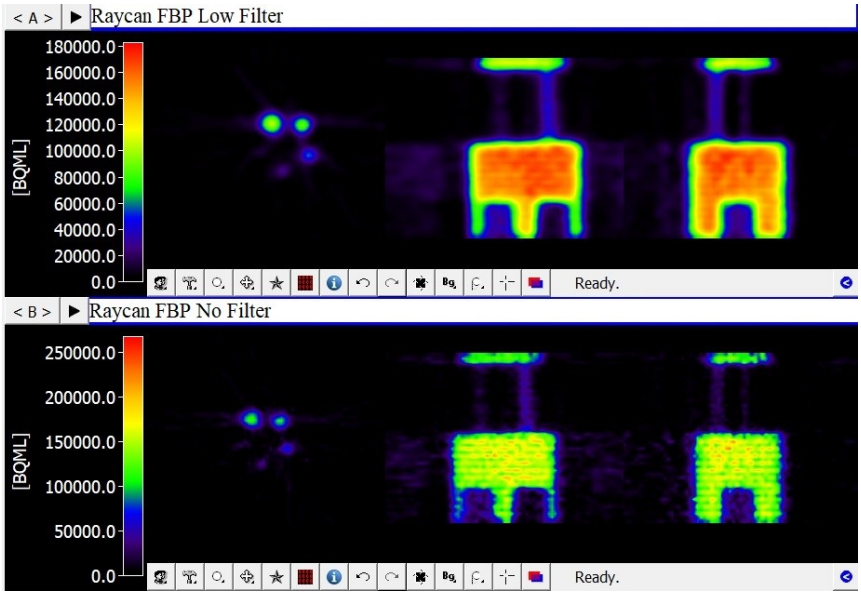

Figure 30. Raycan Image Quality (Section 6) phantom image FBP + SSRB reconstruction with low and no filter.

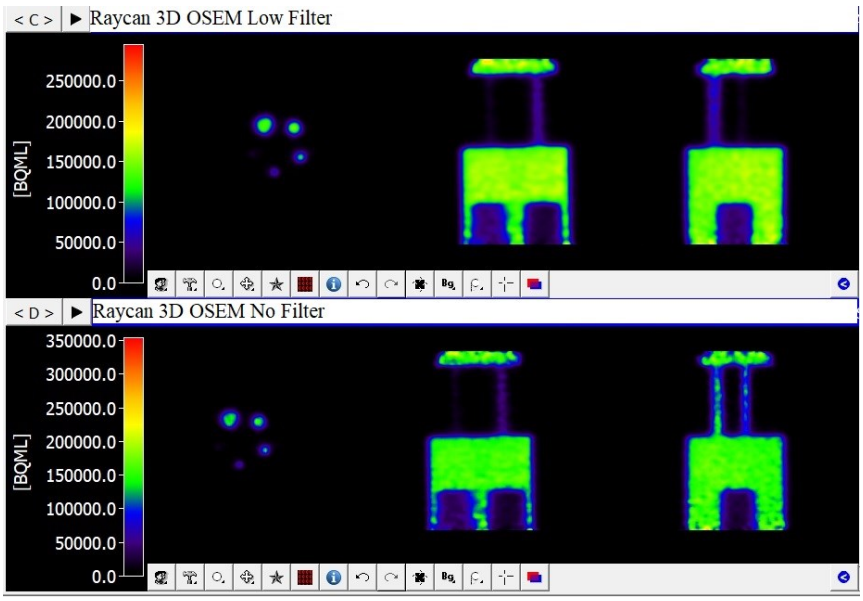

Figure 31. Raycan Image Quality (Section 6) phantom image 3D OSEM + PSF reconstruction with low and no filter.

For all Inveon images (Figures 32 and 33), the effect of scatter correction can't be distinguished visually. Overall, 3D OSEM produced better defined small objects and edges, with all five rods clearly visible in transaxial view.

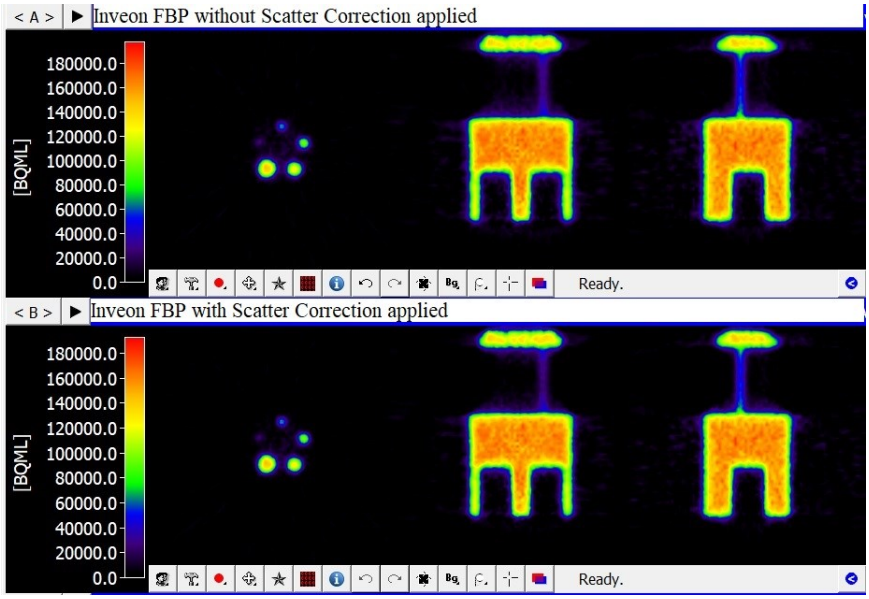

Figure 32. Inveon Image Quality (Section 6) phantom image FBP reconstruction with and without Scatter Correction applied.

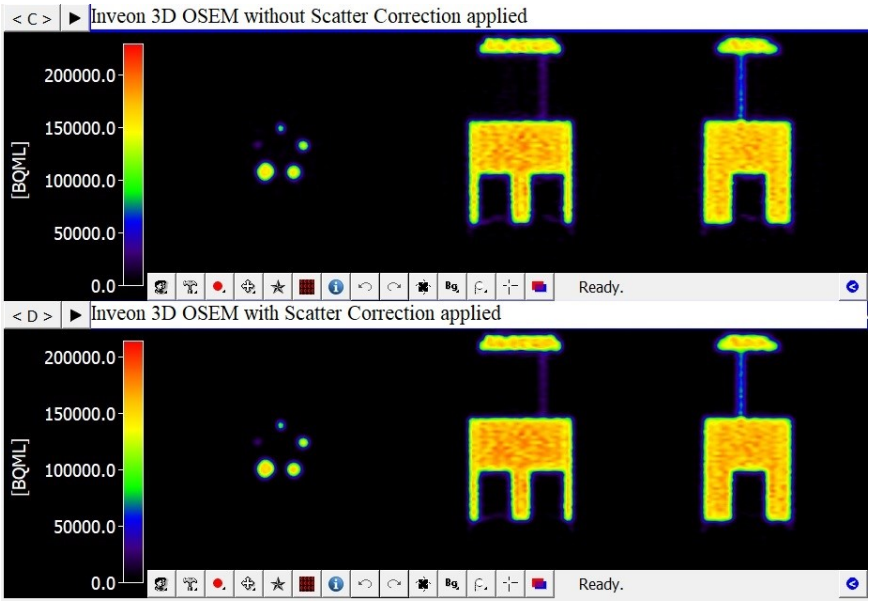

Figure 33. Inveon Image Quality (Section 6) phantom image 3D OSEM reconstruction with and without Scatter Correction applied.

The Molecubes (Figure 34) produces images visually similar to the Inveon 3D OSEM reconstructions, with all five rods visible in transaxial view. However, there is a visible spill-over in the cold regions of air- and water-filled cylinders.

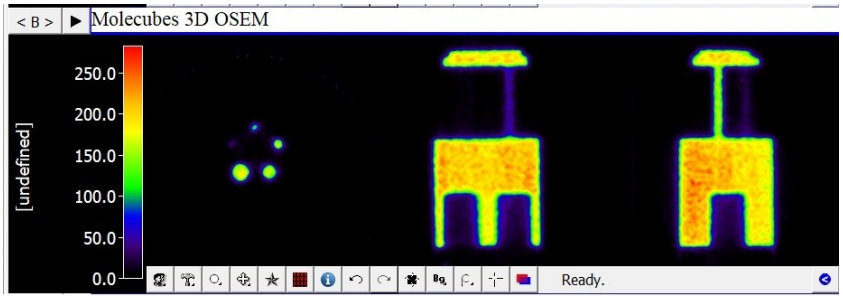

Figure 34. Molecubes Image Quality (Section 6) phantom image 3D OSEM reconstruction.

4.1.2 Comparison of Systems

Table 14. System comparison for Image Quality.

Summary of Results from Image-Quality Phantom													
				Uniform Region			Recovery coefficients					Spillover ratios (%)	
System	Energy window (keV)	Recon. algorithm	Attenuation/ Scatter correction	%SD	Ratio maximum/ mean	Ratio minimum/ mean	1 mm	2 mm	3 mm	4 mm	5 mm	Water	Air
microPET P4[1]	350-650	FORE + 2D FBP	Y/Y	5.2	1.20	0.81	0.11	0.37	0.60	0.77	0.86	4.9	4.0
microPET Focus 220[1]	250-700	FORE + 2D FBP	Y/Y	6.8	1.27	0.71	0.15	0.41	0.63	0.74	0.86	1.2	4.1
microPET R4[1]	350-650	FORE + 2D FBP	Y/N	4.5	1.14	0.80	0.14	0.35	0.60	0.79	0.87	6.2	4.6
microPET Focus 120[1]	350-650	FORE + 2D FBP	Y/Y	6.0	1.25	0.74	0.15	0.18	0.75	0.86	0.93	1.8	20.3
Inveon[1]	350-625	FORE + 2D FBP	Y/Y	5.3	1.18	0.80	0.17	0.48	0.72	0.84	0.93	1.7	20.6
ClearPET[1]	250-650	3D OSEM	N/N	10.9	1.42	0.58	0.11	0.21	0.42	0.73	0.90	36.9	26.7
Mosaic HP[1]	385-665	3D RAMLA	Y/Y	5.1	1.19	0.80	0.16	0.36	0.56	0.70	0.84	6.3	2.7
Argus[1]	250-700	3D OSEM	Y/Y	6.0	1.23	0.81	0.27	0.65	0.93	0.95	0.97	15.0	13.0
VrPET[1]	100-700	3D OSEM	N/N	15.4	1.75	0.47	0.22	0.62	0.72	0.75	0.75	9.3	8.5
LabPET 8[1]	250-650	2D MLEM	N/N	6.0	1.24	0.76	0.19	0.78	0.97	1.00	1.02	24.4	13.7
LabPET 12[1]	250-650	2D MLEM	N/N	7.9	1.29	0.73	0.24	0.77	0.92	0.93	0.97	25.6	16.0
nanoScan Mediso[2]	400-600	(Tera-Tomo) 3D OSEM	Y/Y	4.7	1.26	0.77	0.16	0.84	1.08	1.08	1.09	9.0	9.0
NanoPET/CT[3]	250-750	2D MLEM	N/N	8.0			0.19	0.58	0.81	0.89	0.99	8.0	20.0
Albira[4]	358-664	MLEM	N/Y	4.9			0.05	0.30	0.66	0.77	0.90	21.9	13.9
ClearPET[5]	250-750	3D OSEM	N/N	10.9			0.11	0.21	0.42	0.73	0.89	27.0	37.0
rPET-1[5]	250-650	3D OSEM	N/N	6.9			0.14	0.46	0.66	0.76	0.81	15.0	24.0
LabPET 8[6]	250-650	2D MLEM	N/N	7.0	1.23	0.77	0.13	0.32	0.58	0.83	0.96	20.0	11.0
ClairvivoPET[7]	250-750	FBP	Y/Y	15.3								-0.13	20.0
ClairvivoPET[7]	250-750	List-DRAMA	Y/Y	4.62								6.0	19.0
FLEX Triumph X-PET[8]	250-750	2D OSEM	Y/N	6.01	1.27	0.74	0.15	0.43	0.56	0.68	0.88	9.0	10.0
FLEX Triumph X-PET[8]	250-750	2D FBP	Y/N	6.37	1.24	0.71	0.13	0.39	0.54	0.67	0.85	5.0	19.0
PETBox4[9]	150-650	MLEM	Y/N	5.7			0.10	0.45	0.82	0.93	0.87	14.7	13.3
NanoScan[10]	250-750	(Tera-Tomo) 3D OSEM	Y/Y	3.52	1.13	0.86	0.26	0.84	0.90	0.98	1.03	6.2	5.8
MuPET[11]	350-650	3D OSEM	Y/N	6.5			0.19				0.95	9.0	5.0

Raycan Trans-PET BioCaliburn LH[12]	350-650	3D OSEM	N/N	9.94			0.16		0.76		0.89	9.2	17.7
Albira Trimodal PET/SPECT/CT[13]	358-664	MLEM	Y/Y	4.4	1.17	0.77	0.03	0.19	0.63	0.84	0.95	20.0	20.0
Raycan	350-650	SSRB + 2D FBP Low Filter	Y/N	4.32	1.15	0.86	0.09	0.18	0.36	0.57	0.67	8.5	17.5
Raycan	350-650	SSRB + 2D FBP No Filter	Y/N	19.2	1.66	0.43	0.14	0.27	0.47	0.71	0.76	8.0	16.3
Raycan	350-650	3D OSEM + PSF Low Filter	Y/N	4.59	1.20	0.87	0.10	0.40	0.73	0.93	0.87	14.3	22.8
Raycan	350-650	3D OSEM + PSF No Filter	Y/N	5.72	1.27	0.82	0.11	0.48	0.82	0.98	0.88	14.2	22.4
Inveon	350-650	FORE+2D FBP	Y/N	5.47	1.20	0.77	0.15	0.41	0.67	0.80	0.88	1.8	2.2
Inveon	350-650	FORE+2D FBP	Y/Y	5.78	1.22	0.76	0.14	0.40	0.67	0.81	0.89	-0.4	0.3
Inveon	350-650	3D OSEM	Y/N	7.12	1.28	0.72	0.19	0.57	0.88	0.94	0.93	0.1	0.03
Inveon	350-650	3D OSEM	Y/Y	6.14	1.22	0.76	0.16	0.57	0.89	0.97	0.95	0.1	0.04
Molecubes	409-613	3D OSEM	Y/N	6.81	1.30	0.75	0.20	0.61	0.81	0.82	0.88	11.7	10.3

Notes 1-13: 1. Goertzen et al., 2012; 2. Dahle, 2014; 3. Szanda et al., 2011; 4. Pajak et al., 2016; 5. Cañadas et al., 2011; 6. Prasad et al., 2011; 7. Sato et al., 2016; 8. Prasad et al., 2010; 9. Gu et al., 2013; 10. Nagy et al., 2013; 11. Wong et al., 2012; 12. Wang et al., 2015; 13. Spinks et al., 2014.

The image quality comparison of Table 14 places the Raycan Trans-PET/CT X5 system among average results for Uniformity and Recovery Coefficients, but the quality of data corrections appears to be relatively poor compared to other systems.

4.2 Results for Section 5: Sensitivity

4.2.1 NEMA Standard Report

Table 14 and Figures 35 and 36 summarise the results for NEMA NU 4-2008 Section 5 report for both SSRB- and 3D michelogram-based calculations.

Table 15 sums up the sensitivity parameters for the Raycan. The data were derived from the 3D michelograms and the SSRB 2D sinograms using Formulas 3 to 6 from Part 3.3.3. The use of SSRB-based, recommended by the NEMA standard, method, produces noticeably poorer sensitivity results compared to calculating the values directly from raw 3D michelograms.

Table 15. NEMA NU 4-2008 Section 5 Sensitivity report for the Raycan.

Report for Sensitivity	3D michelogram	SSRB
SM_{tot} (count/s/Bq)	0.9191	0.7909
$SM_{A,tot}$ (%)	101.44	87.29
SR_{tot} (count/s/Bq)	-	-
$SR_{A,tot}$ (%)	-	-

$S_{A,tot}$ (%)	101.44	87.29
Average sensitivity (count/s/Bq)	0.0092	0.0079
Average absolute sensitivity (%)	1.0144	0.8729

According to the sensitivity profiles visualized in Figures 35 and 36, the peak absolute sensitivity of the Raycan is 1.82% for 3D michelogram-based and 1.72% for SSRB sinogram-based data.

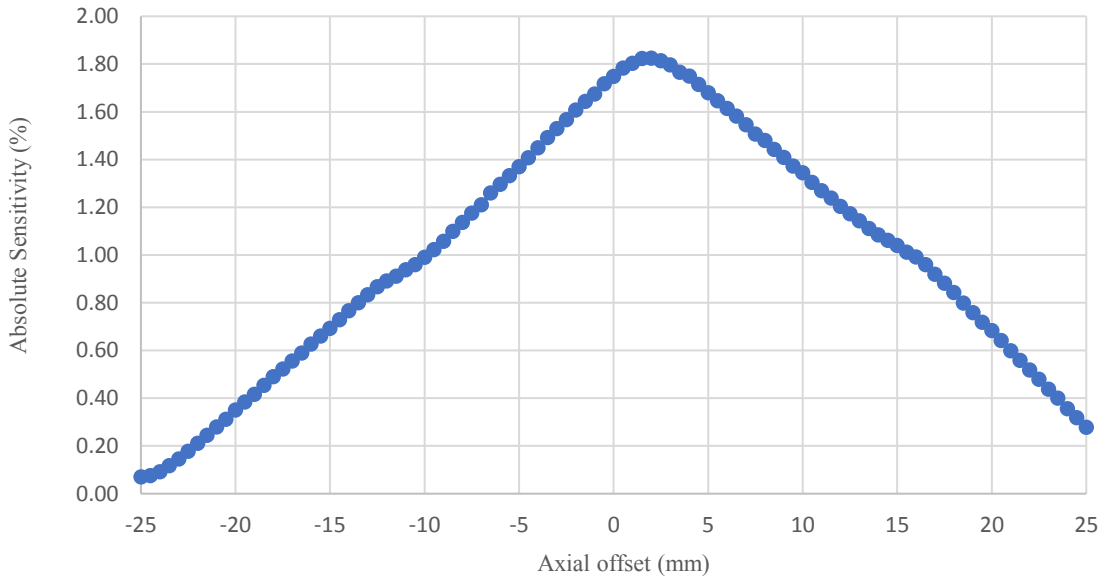

Figure 35. NEMA NU 4-2008 Section 5 Sensitivity report for the Raycan. Peak is at +2.0 offset Absolute sensitivity profiles plotted against the axis. Data from 3D michelogram.

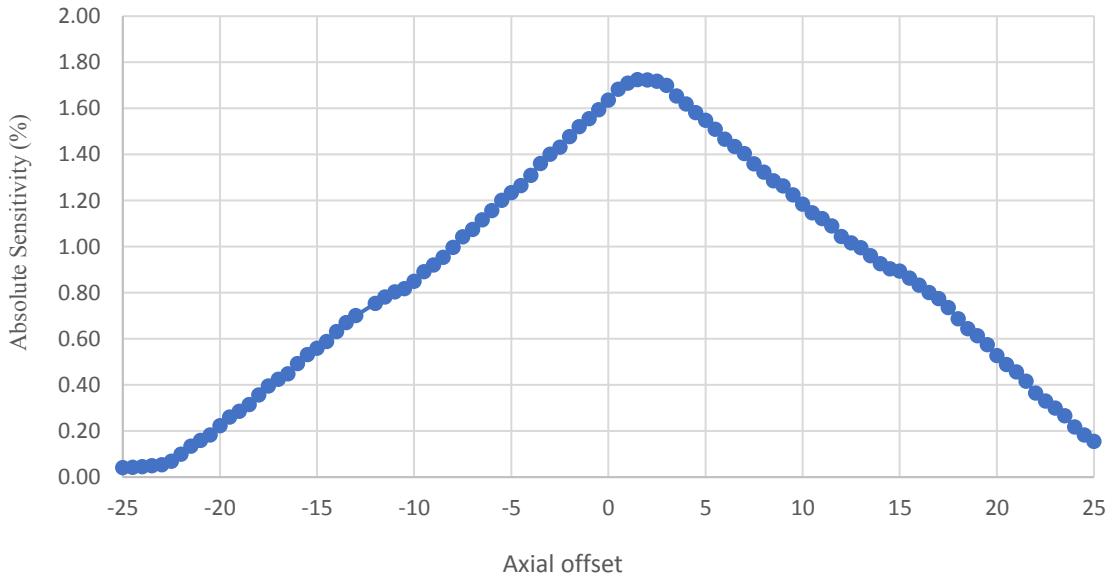

Figure 36. NEMA NU 4-2008 Section 5 Sensitivity report for the Raycan. Peak is at +1.5 offset. Absolute sensitivity profiles plotted against the axis. Data from SSRB sinograms.

4.2.2 Comparison of Systems

Table 16. System comparison for Sensitivities.

System	Energy window (keV)	Axial length (cm)	Average mouse sensitivity (%)	Average total sensitivity (%)	Peak detection efficiency (%)
microPET P4[1]	350-650	7.8	0.67	0.61	1.19
microPET Focus 220[1]	350-650	7.6	1.26	1.18	2.28
microPET R4[1]	350-650	7.8	1.19	1.10	2.06
microPET Focus 120[1]	350-650	7.6	1.98	1.82	3.42
Inveon[1]	350-625	12.7	4.0	2.8	6.72
ClearPET[1]	250-650	11.0	2.32	1.87	3.03
Mosaic HP[1]	385-665	11.9	2.43	1.77	2.83
Argus[1]	250-700	4.8			4.32
VrPET[1]	100-700	4.56	1.09	1.09	2.22
LabPET 8[1]	250-650	7.5	1.45	1.42	2.36
LabPET 12[1]	250-650	11.25	3.6	2.74	5.4
nanoScan Mediso[2]	250-750	9.4	6.1	5.1	8.8
NanoPET/CT[3]	250-750	9.48	5.14	4.21	8.6
Albira[4]	255-767	9.44	3.0		5.29
Albira[4]	358-664	9.44	2.4		4.18
ClearPET[5]	250-750	11.0	2.32	1.87	4.7 (100-750 keV)
rPET-1[5]	250-650	4.56	0.46	0.46	1.0 (100-700 keV)
LabPET 8[6]	250-650	7.5			1.33
ClairvivoPET[7]	250-750	15.1	7.26	4.92	8.72
FLEX Triumph X-PET[8]	250-750	11.6	4.56	3.19	5.9
PETBox4[9]	350-650	9.5			9.3
PETBox4[9]	150-650	9.5	14		18.1
NanoScan[10]	250-750	9.4	5.83		
MuPET[11]	350-650	11.6			6.38
Raycan Trans-PET BioCaliburn LH[12]	350-650	5.3			2.04
Albira Trimodal PET/ SPECT/CT[13]	358-664	14.8	4.6	3.3	6.3
Raycan (3D mich)	350-650	5.0	1.01	1.01	1.82
Raycan (SSRB)	350-650	5.0	0.90	0.90	1.72

Notes 1-13: 1. Goertzen et al., 2012; 2. Dahle, 2014; 3. Szanda et al., 2011; 4. Pajak et al., 2016; 5. Cañadas et al., 2011; 6. Prasad et al., 2011; 7. Sato et al., 2016; 8. Prasad et al., 2010; 9. Gu et al., 2013; 10. Nagy et al., 2013; 11. Wong et al.; 12. Wang et al., 2015; 13. Spinks et al., 2014

When compared to other systems, the Raycan PET/CT produces below average sensitivity values.

4.3 Results for Section 4: Scatter Fraction, Count Losses, and Random Coincidence Measurements

4.3.1 NEMA Standard Report

Tables 17 and 18 and Figures 37 to 40 summarise the report for NEMA NU 4-2008 count rate report. The calculations were done with Formulas 8 to 16 from Part 3.4.3.

Table 17. NEMA NU 4-2008 Section 4 Peak Count Rate Values report for rat-sized phantom, Raycan. Data analyzed from 3D michelogram and 2D sinogram rebinned by SSRB.

Peak Count Rate Values. rat-sized phantom	3D michelogram	SSRB
$R_{t.\ peak}$	75685.6	73935.80
$R_{NEC.\ peak}$	54895.7	64315.90
$R_{t.\ peak}$ activity	56.53 MBq	56.53 MBq
$R_{NEC.\ peak}$ activity	56.53 MBq	56.53 MBq

Table 17 and Figures 37-38 compare count rate statistics from rat-sized phantoms calculated from 3D michelogram and SSRB 2D sinograms. The peak values for both methods are at 56.53 MBq activity, but 3D michelogram produces higher total, true, scatter and random counts compared to corresponding time points of SSRB. For noise equivalent counts, SSRB produces higher values, due to total counts being lower while true counts are approximately equal.

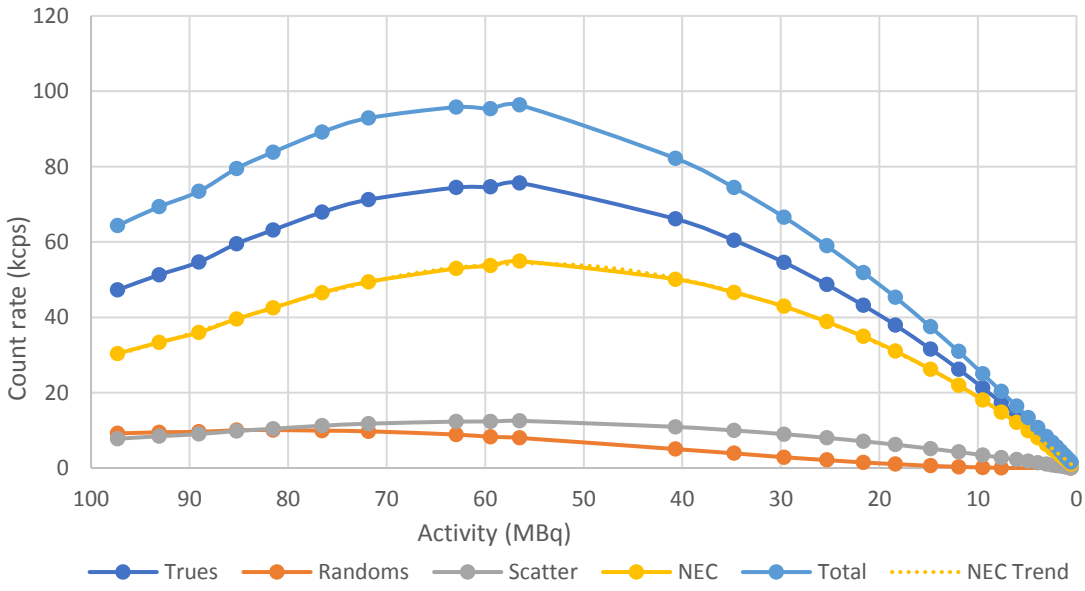

Figure 37. NEMA NU 4-2008 Section 4 report plot of count rates against remaining activity in rat-sized phantom, Raycan. Data analyzed from 3D michelogram. Three data points were excluded due to operator error.

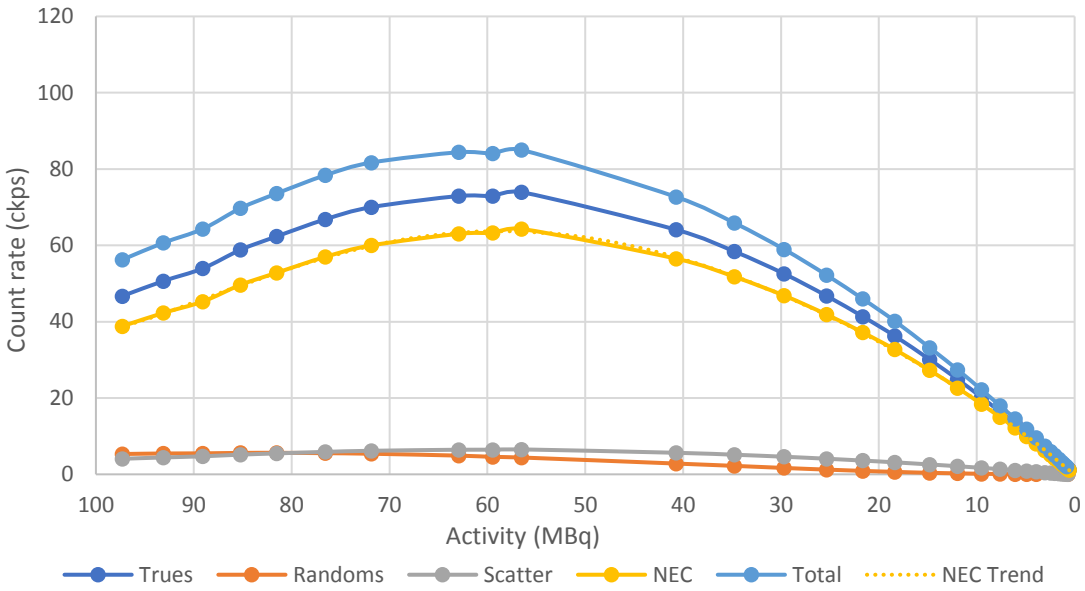

Figure 38. NEMA NU 4-2008 Section 4 report plot of count rates against remaining activity in rat-sized phantom, Raycan. Data analyzed from SSRB sinograms. Three data points were excluded due to operator error.

For mouse-sized phantom analyzed from 3D michelogram (Figure 39), noise equivalent count rate trendline had highest R^2-value as 5th order polynomial function with the formula $y = 0.00003x^5 - 0.0075x^4 + 0.6185x^3 - 39.85x^2 + 2257.6x - 204.07$. For rat-sized phantom (Figure 37), same data had highest R^2-value as 5th order polynomial function with the formula $y = 0.00004x^5 - 0.0075x^4 + 0.5296x^3 - 31.628x^2 + 2222x - 150.48$. These values were used to calculate NECR values for Table 19 (Part 4.3.2).

Table 18 and Figures 39-40 compare count rate statistics from mouse-sized phantoms calculated from 3D michelogram and SSRB 2D sinograms. The peak value for noise equivalent counts peak calculated from 3D michelogram was unexpectedly different from others (52.52 MBq compared to 55.94 MBq). Otherwise, the count rate statistics follow a pattern similar to rat phantom, with 3D michelograms producing higher total, true, scatter and random counts compared to corresponding time points of SSRB. For noise equivalent counts, SSRB produces again higher rate values.

Table 18. NEMA NU 4-2008 Section 4 Peak Count Rate Values report for mouse-sized phantom, Raycan. Data analyzed from 3D michelogram and 2D sinogram rebinned by SSRB.

Peak Count Rate Values. mouse-sized phantom	3D michelogram	SSRB
$R_{t.\ peak}$	154108	152766
$R_{NEC.\ peak}$	125861	141327
$R_{t.\ peak}$ activity	55.94 MBq	55.94 MBq
$R_{NEC.\ peak}$ activity	52.52 MBq	55.94 MBq

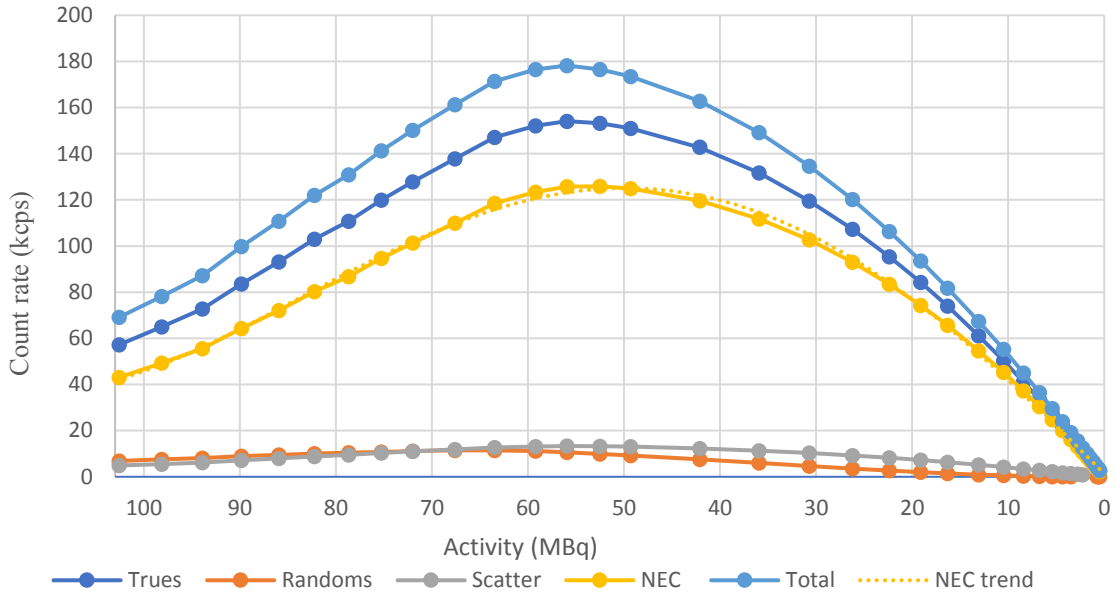

Figure 39. NEMA NU 4-2008 Section 4 report plot of count rates against remaining activity in mouse-sized phantom, Raycan. Data analyzed from 3D michelogram.

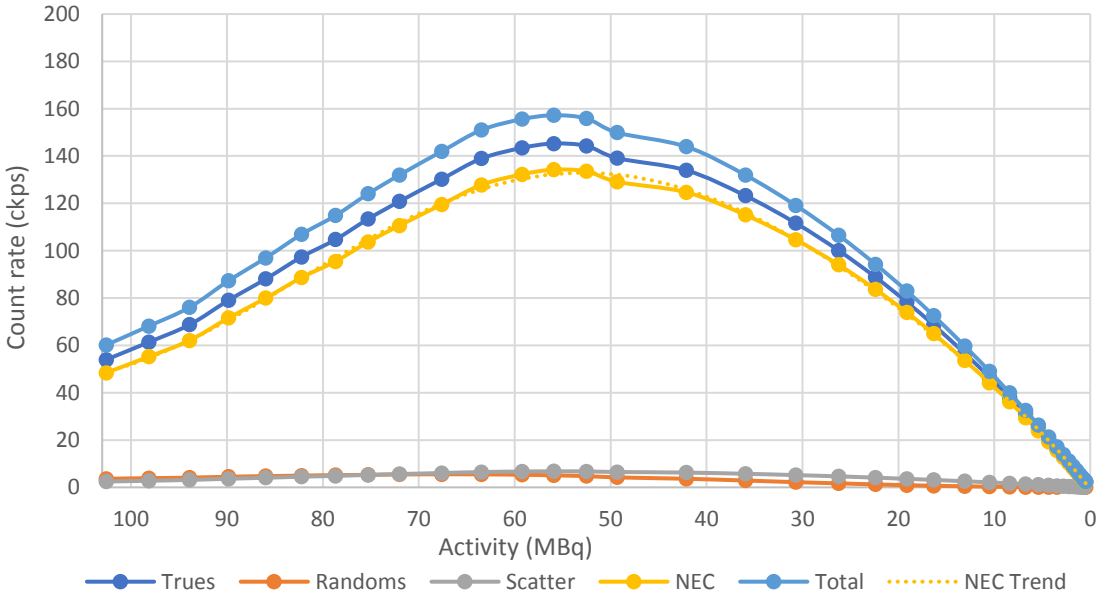

Figure 40. NEMA NU 4-2008 Section 4 report plot of count rates against remaining activity in mouse-sized phantom, Raycan. Data analyzed from SSRB sinograms.

For mouse-sized phantom analyzed from SSRB (Figure 40), noise equivalent count rate trendline had highest R^2-value as 4th order polynomial function with the formula $y = 0.005x^4 - 0.818x^3 - 5.6869x^2 + 4176.7x + 1363.1$. For rat-sized phantom, same data (Figure 38) had highest R^2-value as 6th order polynomial function with the formula $y = -0.000001x^6 + 0.0005x^5 - 0.063x^4 + 3.244x^3 - 109.37x^2 + 5141.4x - 656.88$. These values were used to calculate NECR values for Table 19 (Part 4.3.2).

4.3.2 Comparison of Systems

Among the systems compared in Table 19, the Raycan shows average count rate statistics with good capacity for measuring high activity.

Table 19. System comparison for Count Rates.

Summary of Counting-Rate Test Results for Mouse and Rat Phantoms											
				Mouse phantom				Rat phantom			
System	Energy window (keV)	Timing window (ns)	Randoms correction	Peak NECR (kcps)	Activity (MBq)	NECR at 3.7 MBq (kcps)	Scatter fraction (%)	Peak NECR (kcps)	Activity (MBq)	NECR at 10 MBq (kcps)	Scatter fraction (%)
microPET P4[1]	350-650	6	Calculated	601*	174*	22.1	5.2	173	254	19.2	16.7
microPET R4[1]	250-700	6	Calculated	618	156	37.2	9.3	164	137	30.5	22.2
microPET Focus 120[1]	350-650	6	Calculated	897	103	66.5	5.6	267	129	50.9	20.3
microPET Focus 220[1]	350-650	6	Calculated	763*	89*	47.3	7.2	359	162	51.8	19.3
Inveon[1]	350-625	3.4	Calculated	1670	131	129.0	7.8	592	110	137.8	17.2
ClearPET[1]	250-650	12	Calculated	73	18	29.3	31.0				
Mosaic HP[1]	385-665	7	Measured	555	92	59.6	5.4	244	87	65.2	12.7
Argus[1]	250-700	7	Calculated	117	50	18.7	21.0	40	41	20.4	34.4
VrPET[1]	100-700	3.8	Calculated	74	22		11.5	31	34		23.3
LabPET 8[1]	250-650	20	Calculated	279	82	23.5	15.6	94	91	19.4	29.5
LabPET 12[1]	250-650	20	Calculated	362	81	38.9	16.0	156	83	40.5	29.3
nanoScan Mediso[2]	400-600	5	None	427.9	33	(100)	19.3				
NanoPET/CT[3]	250-750	5	None (?)	430	36		15	130	27		30
Albira[4]	358-664	5		72			9.8	42			21.8
ClearPET[5]	250-750			73.4	(17.5)		31.0				
rPET-1[5]	250-650			29.2	(46.4)		24.2				
LabPET 8[6]	250-650	22	No	183			19	67			31
ClairvivoPET[7]	250-750	10		415			17.7				
FLEX Triumph X-PET[8]	250-750	12		106	5.8		7.9	49	5.6		21
PETBox4[9]	150-650	20		35	1.5		28				
NanoScan[10]	250-750	5		406			17.3	119			34
MuPET[11]	350-650	3.4		1100	57		11.9	354	63		28
Raycan Trans-PET BioCaliburn LH[12]	350-650	5	No	62	28		8.4	25	31		17.7
Raycan Trans-PET BioCaliburn LH[12]	250-750	5	No	110	38		11.3	40	34		19.3
Albira Trimodal PET/ SPECT/CT[13]	358-664	N/A									

Raycan (3D michelogram)	350-650	5	Not used	126	52.5	16.7	13.1	55	56.53	18.9	21.9
Raycan (SSRB)	350-650	5	Not used	141	56	17.0	13.7	64	56.53	19.4	24.1

Notes 1-13: 1. Goertzen et al., 2012; 2. Dahle, 2014; 3. Szanda et al., 2011; 4. Pajak et al., 2016; 5. Cañadas et al., 2011; 6. Prasad et al., 2011; 7. Sato et al., 2016; 8. Prasad et al., 2010; 9. Gu et al., 2013; 10. Nagy et al., 2013; 11. Wong et al.; 12. Wang et al., 2015; 13. Spinks et al., 2014
Values in brackets (): approximations from figures.
** Peak value not reached because of insufficient activity at start of scan.*

4.4 Results for Section 3: Spatial Resolution

4.4.1 NEMA Standard Report

Table 20 presents the spatial resolution results for the Raycan system. Despite the Raycan FOV being 130 mm that should have theoretically allowed to measure spatial resolution until at least 50 mm point, in practice the difficulty of accurate phantom positioning and poor preliminary results prompted to discard the measurement points beyond 25 mm.

Table 20. NEMA NU 4-2008 Section 3 Spatial Resolution report for the Raycan.

Report for Spatial Resolution										
Reconstructed image pixel size (mm): 1							Algorithm: FBP. No filter			
Slice thickness (mm): 1										
At axial center										
	0 mm		5 mm		10 mm		15 mm		25 mm	
	FWHM	FWTM	FWHM	FWTM	FWHM	FWTM	FWHM	FWTM	FWHM	FWTM
Radial	2.15	4.21	2.40	4.61	2.17	4.02	2.15	4.34	2.13	4.46
Tangential	2.30	4.90	2.49	4.43	2.20	4.73	2.38	5.10	2.93	5.89
Axial	1.34	3.42	1.32	3.40	1.33	3.39	1.37	3.53	1.52	3.53
At 1/4 + axial FOV from center										
Radial	2.15	4.17	2.39	4.62	2.20	4.08	2.14	4.20	2.11	4.27
Tangential	2.33	5.25	2.51	4.66	2.23	4.76	2.41	5.55	3.00	6.08
Axial	1.83	3.55	1.83	3.59	1.89	3.59	1.92	3.66	2.18	3.93
At 1/4 - axial FOV from center										
Radial	2.12	4.23	2.38	4.61	2.17	4.20	2.13	4.09	1.98	4.13
Tangential	2.36	5.02	2.49	4.47	2.24	4.59	2.52	5.46	3.08	5.92
Axial	1.82	3.58	1.81	3.62	1.73	3.58	1.89	3.65	2.07	3.76

Overall, the Raycan scanner produces stable resolution results within central 50 mm of the FOV, with poorest resolution in tangential direction that gradually worsens as the distance from axial center increases, but is almost unaffected along the axis. Axial resolution is slightly affected by distance from axial center, with results further worsening towards the ends of the axis. Radial resolution is almost unaffected by the position within FOV.

4.4.2 Comparison of Systems

Spatial Resolution Results							
		FWHM/FWTM (mm) at axial center of FOV			FWHM/FWTM (mm) at ¼ axial offset		
System	Radial offset (mm)	Radial	Tangential	Axial	Radial	Tangential	Axial
microPET P4[1], 350-650 keV Fourier rebinning + 2D FBP	5	2.29/4.03	2.18/3.81	2.20/4.52	2.34/4.22	2.14/3.77	1.78/4.22
	10	2.41/4.23	2.23/3.92	2.38/4.66	2.37/4.14	2.22/3.84	1.97/4.49
	15	2.42/4.19	2.28/3.83	2.42/4.68	2.39/4.16	2.27/3.87	2.04/4.53
	25	2.61/4.67	2.25/3.76	2.42/4.67	2.53/4.41	2.30/3.91	2.07/4.50
	50	3.27/6.40	2.40/4.10	2.58/5.09	3.20/6.08	2.45/4.29	2.30/4.74
	75	3.92/8.07	2.64/4.53	2.88/5.99	3.78/7.12	2.81/5.15	2.72/5.58
microPET Focus 220[1], 250-750 keV Fourier rebinning + 2D FBP	5	1.75	1.80	1.70	1.70	1.70	1.73
	10	1.68	1.78	1.73	1.66	1.79	1.75
	15	1.82	1.71	1.80	1.88	1.72	1.78
	25	2.07	1.69	1.84	2.09	1.74	1.87
	50	2.88	1.77	1.98	2.82	1.82	1.92
	75	4.08	1.90	2.16	3.92	1.90	2.11
microPET R4[1], 350-750 keV Fourier rebinning + 2D FBP	5	2.13/4.90	2.21/4.22	2.72/5.59	2.06/5.24	2.18/4.14	2.37/4.88
	10	2.30/4.60	2.31/4.36	3.02/6.54	2.30/4.61	2.29/4.39	2.66/5.31
	15	2.86/5.38	2.39/4.57	3.25/7.48	2.63/5.35	2.35/4.40	2.84/5.71
	25	3.30/6.32	2.51/4.66	3.27/7.57	3.31/6.23	2.53/4.80	3.09/6.31
microPET Focus 120[1], 350-750 keV Fourier rebinning + 2D FBP	5	1.92/3.66	1.66/3.06	1.90/3.81	1.92/3.63	1.65/3.09	1.62/3.28
	10	1.88/3.95	1.74/3.22	1.94/3.91	1.83/3.69	1.76/3.28	1.66/3.34
	15	1.99/4.02	1.72/3.11	1.98/4.05	1.94/3.75	1.77/3.22	1.69/3.41
	25	2.53/4.84	1.73/3.01	2.05/4.34	2.45/4.49	1.80/3.20	1.81/3.67
Inveon[1], 350-625 keV Fourier rebinning + 2D FPB	5	1.63/3.36	1.62/3.15	2.45/5.62	1.66/3.32	1.63/3.14	1.97/4.20
	10	1.80/3.84	1.58/2.91	2.40/5.51	1.72/3.40	1.64/3.18	2.12/4.44
	15	2.03/4.32	1.56/2.78	2.29/5.32	1.87/3.69	1.63/3.05	2.17/4.72
	25	2.49/5.17	1.61/2.86	2.09/4.67	2.38/4.76	1.65/2.97	2.06/4.54
ClearPET[1], 250-650 keV 3D FBP	5	1.94/3.76	2.00/4.17	3.24/6.05	2.18/4.05	1.97/3.92	3.18/5.91
	10	1.85/3.47	2.27/5.97	3.19/5.97	1.87/3.68	2.14/4.86	3.20/5.88
	15	2.01/3.62	2.43/5.53	3.20/5.96	2.05/3.84	2.33/5.25	3.19/5.83
	25	2.55/4.28	2.42/5.69	3.21/5.97	2.50/4.18	2.43/6.59	3.19/5.85
Mosaic HP[1], 385-665 keV 3D Fourier reprojection	5	2.32/5.30	2.32/4.97	2.64/6.07	2.33/5.32	2.40/4.88	2.48/5.32
	10	2.45/5.48	2.514.96	2.82/6.14	2.37/5.54	2.49/4.97	2.80/5.89
	15	2.43/5.44	2.65/5.24	2.79/6.28	2.48/5.62	2.63/5.25	2.80/5.92
	25	2.59/5.93	2.83/5.25	2.96/6.28	2.63/5.81	2.87/5.31	3.10/6.30

Table 21. System comparison for Spatial Resolutions.

Argus[1], 250-700 keV 2D FBP	5	1.63	1.65		1.65	1.70	
	10	1.71	1.70		1.74	1.75	
	15	1.85	1.70		1.85	1.75	
	25	2.25	1.73		2.15	1.85	
VrPET[1], 100-700 keV SSRB + 2D FBP	5	1.52/2.76	1.62/2.99	2.66/4.81	1.62/2.95	1.68/2.86	
	10	1.58/2.85	1.68/3.02	3.03/5.45	1.54/2.89	1.68/3.07	
	15	1.78/3.25	1.51/2.79	3.11/5.50	1.69/3.09	1.73/3.14	
	25	2.03/3.69	5.12/3.72	3.32/5.92	1.79/3.29	1.98/3.60	
LabPET 8[1], 250-650 keV SSRB + 2D FBP	5	1.65/3.40	1.70/3.30	Intrinsic res. 1.4/4.3	1.57/3.30	1.65/3.50	Intrinsic res. 1.4/4.3
	10	1.91/3.60	1.82/3.67		1.92/3.40	1.74/3.45	
	15	2.01/4.10	1.83/3.70		1.92/3.77	1.86/3.90	
	25	2.56/4.65	1.90/4.28		2.55/4.70	1.93/4.30	
nanoScan Mediso[2], 250-750 keV SSRB SINO + 2D FBP	0	1.28/3.16	1.18/3.05	0.93/2.68	1.20/3.02	1.14/2.98	1.43/2.94
	5	1.50/3.39	1.46/3.36	1.13/2.78	1.46/3.32	1.33/3.19	1.43/2.93
	10	1.53/3.34	1.49//3.58	1.09/2.85	1.36/3.16	1.41/3.42	1.51/2.99
	15	1.69/3.40	1.67/4.28	1.20/3.05	1.63/3.27	1.67/4.14	1.11/3.08
	25	2.34/3.64	2.02/7.27	1.23/3.29	2.39/3.65	1.90/7.21	1.19/3.36
	35	2.36/4.04	2.34/-	1.32/3.46	2.48/4.30	2.11/7.00	1.80/4.13
nanoScan Mediso[2], 400-600 keV Tera-Tomo	0	0.60/1.34	0.97/1.47	0.55/1.31	0.60/1.34	0.81/1.45	0.62/1.25
	5	0.82/1.46	0.87/1.63	0.46/1.41	0.89/1.31	0.94/1.41	0.72/1.16
	10	0.83/1.55	0.85/1.66	0.77/1.41	0.71/1.50	0.86/1.61	0.67/1.26
	15	0.91/1.78	0.86/1.76	0.72/1.40	0.85/1.73	0.89/1.71	0.71/1.34
	25	1.11/1.98	0.96/1.90	0.72/1.40	1.06/1.91	0.93/1.82	0.68/1.30
	35	1.08/1.98	1.00/1.93	0.72/1.39	1.04/1.86	1.01/1.91	0.66/1.30
NanoPET/CT[3], 250-750 keV SSRB + 2D FBP		<2.5	<2.5	~1	<2.5	<2.5	~2
Albira[4], 358-664 keV SSRB + 2D FBP	0	N/A			1.78/3.24	1.72/3.13	2.47/4.51
	5				1.92/3.50	1.31/2.38	2.59/4.72
	10				2.59/4.73	1.57/2.87	2.69/4.89
	15				5.14/9.37	1.14/2.07	2.59/4.72
	20				6.81/12.42	0.90/1.63	3.26/5.95
	25				7.91/14.41	1.01/1.84	3.06/5.57
Albira[4], 358-664 keV MLEM	0	1.72/3.13	1.70/3.10	2.45/4.47	1.52/2.78	1.69/3.07	1.45/2.64
	5	1.68/3.06	1.75/3.19	2.44/4.44	1.55/2.83	1.60/2.91	1.42/2.59
	10	1.93/3.52	1.63/2.97	2.44/4.45	1.86/3.39	1.58/2.8	1.48/2.69
	15	2.24/4.08	1.68/3.07	2.62/4.78	2.13/3.89	1.65/3.01	1.55/2.83
	20	2.58/4.71	1.74/3.17	2.81/5.11	2.33/4.25	1.66/3.02	1.52/2.78
	25	2.81/5.12	1.95/3.55	2.77/5.05	2.79/5.08	1.95/3.55	1.62/2.96

ClearPET[5], 250-750 keV DRP + 3D FBP	5	1.9/3.8	2.0/4.2	3.2/6.0	2.2/4.0	2.0/3.9	3.2/5.9
	10	1.8/3.4	2.3/5.0	3.2/6.0	1.9/3.7	2.1/5.0	3.2/5.9
	15	2.0/3.6	2.4/5.5	3.2/6.0	2.0/3.8	2.3/5.2	3.2/5.8
	20	2.6/4.5	2.3/4.5	3.2/5.9	2.4/3.9	2.3/5.7	3.2/5.8
	25	2.5/4.3	2.4/5.7	3.2/6.0	2.5/4.2	2.4/5.6	3.2/5.8
rPET-1[5], 250-650 keV DRP + 3D FBP	5	1.4/2.5	1.6/3.0	1.8/3.2	1.5/2.8	1.6/3.0	1.5/2.8
	10	1.3/2.3	1.8/3.3	2.1/3.8	1.5/2.7	1.7/3.0	1.8/3.3
	15	1.1/2.1	2.1/3.9	2.3/4.1	1.3/2.4	1.9/3.8	2.1/3.9
	20	1.1/1.9	2.4/4.3	2.7/4.8	1.4/2.6	1.7/3.2	2.4/4.7
LabPET 8[6], 250-650 SSRB+ 2D FBP	5	FWHM 1.7-2.59 FWTM 3.1-4.91	(FWHM 1.7-2.59) (FWTM 3.1-4.91)	FWHM 2.41-2.63 FWTM 4.4-4.79			
	10						
	15						
	25						
LabPET 8[6], 250-650 2D MLEM	5	FWHM 0.84-1.14 FWTM 1.53-2.08	(FWHM 0.84-1.14 FWTM 1.53-2.08)	FWHM 1.55-1.53 FWTM 2.83-2.81			
	10						
	15						
	25						
ClairvivoPET[7], 250-450 keV FORE+ 2D FBP	5	FWHM 2.16-4.12 (FWTM 4-7)	(FWHM 2.5-4.4) (FWTM 4.3-8)	FWHM 2.43-2.63 (FWTM 4.4-4.7)	(FWHM 2.2-4.7) (FWTM 4-8.9)	(FWHM 2.9-5.1) (FWTM 5.1-9.6)	(FWHM 3.1-3.5) (FWTM 5.9-6.5)
	10						
	15						
	25						
	50						
FLEX Triumph X-PET[8], 250-750 2D FBP	5	FWHM 2.0-2.3 (FWTM 3.5-4.1)	(FWHM 2.3-2.4) (FWTM 4-4.5)	FWHM 2.8-3.2 (FWTM 5.1-5.5)	(FWHM 2-2.5) (FWTM 4-4.1)	(FWHM 2.5-3) (FWTM 4.5-5)	(FWHM 3.2-3.4) (FWTM 5.9-6)
	10						
	15						
	25						
PETBox4[9], 150-650 keV MLEM	0	(FWHM 1.5-1.9) (FWTM 3.5-4.1)	(FWHM 1.3-1.4) (FWTM 3.2-3.4)	(FWHM 1.3-1.5) (FWTM 3.5-4)	(FWHM 1.3-1.9) (FWTM 3.5-4)	(FWHM 1.1-1.4) (FWTM 3.1-3.5)	(FWHM 1.2-1.3) (FWTM 3.2-3.6)
	5						
	10						
	15						
	20						
NanoScan[10], 400-600 keV SSRB + FBP	5	1.50/3.29	1.32/3.14	0.91/2.85	1.41/3.27	1.33/3.17	1.23/2.92
	10	1.49/3.32	1.39/3.38	1.16/2.93	1.49/3.24	1.43/3.29	0.97/3.10
	15	1.97/4.07	1.54/3.61	1.67/3.33	1.81/3.84	1.48/3.52	1.49/3.38
	25	2.01/4.05	1.66/3.85	1.57/3.42	2.03/4.11	1.70/3.87	1.89/4.10
MuPET[11], 350-650 keV SSRB+ 2D FBP	0	1.25/3.03	1.14/2.42	0.94/2.35			
	2	1.22/2.92	1.30/2.42	0.96/2.57			
	5	1.48/2.92	1.34/2.53	0.99/2.52			
	10	1.52/3.01	1.39/2.51	1.00/2.60			

	15	1.67/3.20	1.36/2.43	1.05/2.62			
	20	1.74/3.47	1.34/2.45	1.04/2.63			
	25	1.88/3.74	1.34/2.43	1.08/2.68			
	30	2.08/4.02	1.36/2.49	1.12/2.71			
	40	2.61/4.89	1.57/2.96	1.26/2.98			
Raycan Trans-PET BioCaliburn LH[12], 350-650 keV 3D OSEM	0	0.95	1.05	1.01	„essentially identical to axial center of FOV“		
	15	0.96	1.13	0.99			
	30	1.30	1.28	1.00			
	65	1.75	1.69	1.13			
Albira Trimodal PET/ SPECT/CT[13], 358-664 keV MLEM	5	(1.5/)	(1.5/)	(1.4/)	(1.7/)	(1.6/)	
	10	(1.8/)	(1.5/)	(1.4/)	(2.0/)	(1.6/)	(2.4/)
	15	(2.0/)	(1.6/)	(1.4/)	(2.2/)	(1.7/)	(2.4/)
	20	(2.3/)	(1.6/)	(1.4/)	(2.3/)	(1.8/)	(2.4/)
	25	(2.5/)	(1.6/)	(1.5/)	(2.5/)	(1.8/)	(2.4/)
Raycan 350-650 keV 2D FBP	0	2.15/4.21	2.30/4.90	1.34/3.42	2.15/4.17	2.33/5.25	1.83/3.55
	5	2.40/4.61	2.49/4.43	1.32/3.40	2.39/4.62	2.51/4.66	1.83/3.59
	10	2.17/4.02	2.20/4.73	1.33/3.39	2.20/4.08	2.23/4.76	1.89/3.59
	15	2.15/4.34	2.38/5.10	1.37/3.53	2.14/4.20	2.41/5.55	1.92/3.66
	25	2.13/4.46	2.93/5.89	1.52/3.53	2.11/4.27	3.00/6.08	2.18/3.93

Notes 1-13: 1. Goertzen et al., 2012; 2. Dahle, 2014; 3. Szanda et al., 2011; 4. Pajak et al., 2016; 5. Cañadas et al., 2011; 6. Prasad et al., 2011; 7. Sato et al., 2016; 8. Prasad et al., 2010; 9. Gu et al., 2013; 10. Nagy et al., 2013; 11. Wong et al.; 12. Wang et al., 2015; 13. Spinks et al., 2014
Values in brackets (): approximations from figures.

Overall, the Raycan produces somewhat poorer than average spatial resolution results when compared to other systems. However, while NEMA NU 4-2008 specifies the use of FBP reconstruction, a significant portion of studies used iterative algorithms such as OSEM and MLEM. Because of the nature of iterative reconstruction algorithms, such spatial resolution data does not reflect the actual performance and capabilities of the systems. When compared to systems that used FBP reconstruction, the Raycan produces average, but acceptable results.

4.5 Results of Live Animal Imaging

Results of live animal comparison are on Figures 41 to 47. SUVs were calculated following the Formula 17 from Part 3.6.2. On Figure 41, full-body static scans of rats 2 hours after ^{18}F-FDG injection are presented side by side as seen in Carimas software with settings adjusted to produce best quality image for the operator. Overall, both the Raycan and the Inveon systems produce images with the quality sufficient for most preclinical studies.

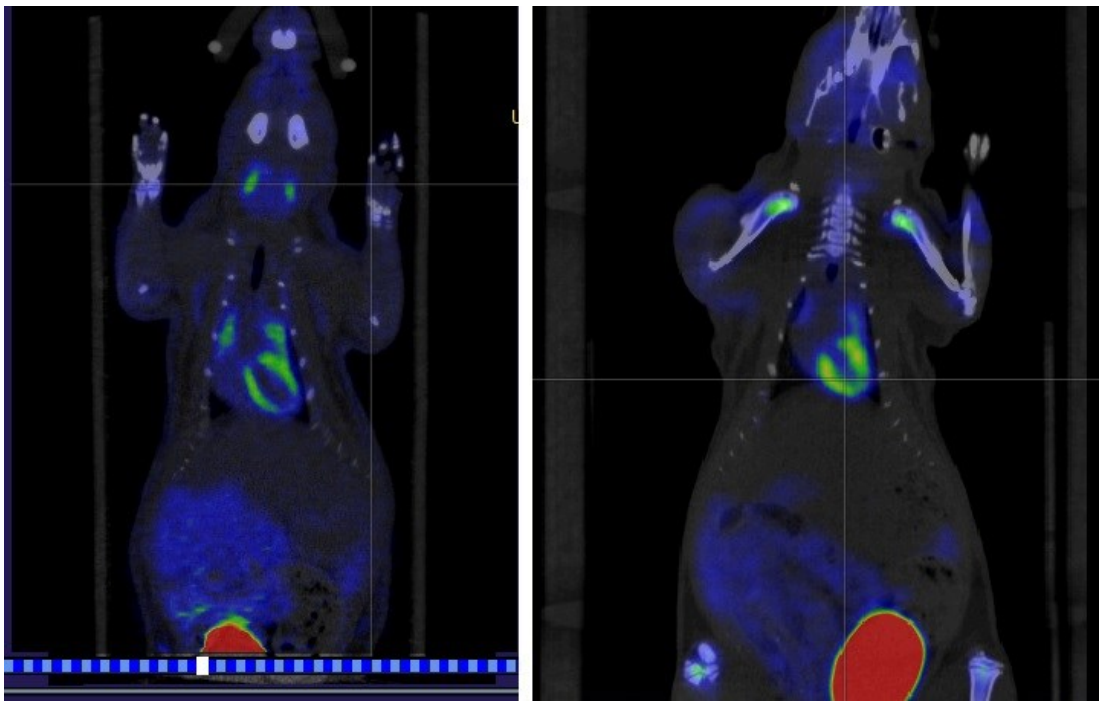

Figure 41. PET and CT images from third scan session (120 min after ^{18}F-FDG injection) combined in Carimas. Rat 1 imaged with the Raycan system (left), Rat 2 with the Inveon (right).

Figures from 42 to 47 show SUV values of tissues from all acquisitions combined (dynamic, static 1 and static 2). From Figures 42, 43 and 44, an inconsistency in myocardium (heart) values is seen. Different from the Inveon, dynamic scan from the Raycan produced overly high SUV value for heart (HeartRD). The expected value should be on the approximate level of corrected SUV values from subsequent static scans (Heart IS corrected and Heart RS corrected). The results for other tissues had no noticeable abnormalities, most probably due to the low activity and thus visually undetectable difference between curves.

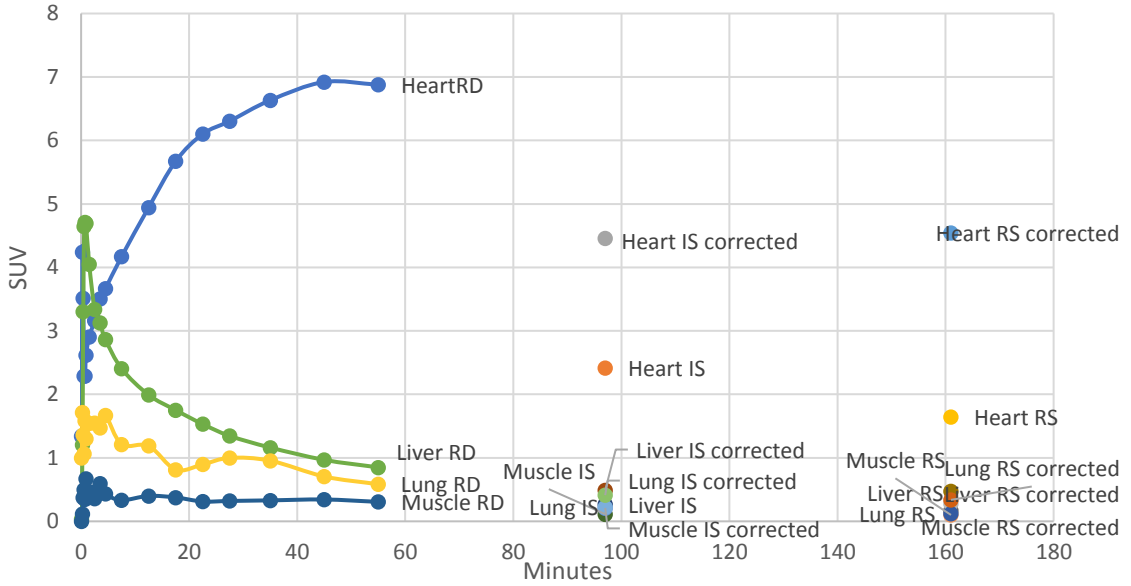

Figure 42. SUV of Rat 1 tissues. RD = Raycan Dynamic; ID = Inveon Dynamic; RS = Raycan Static; IS = Inveon Static. "Corrected" points have their activity values corrected to timepoint 0.

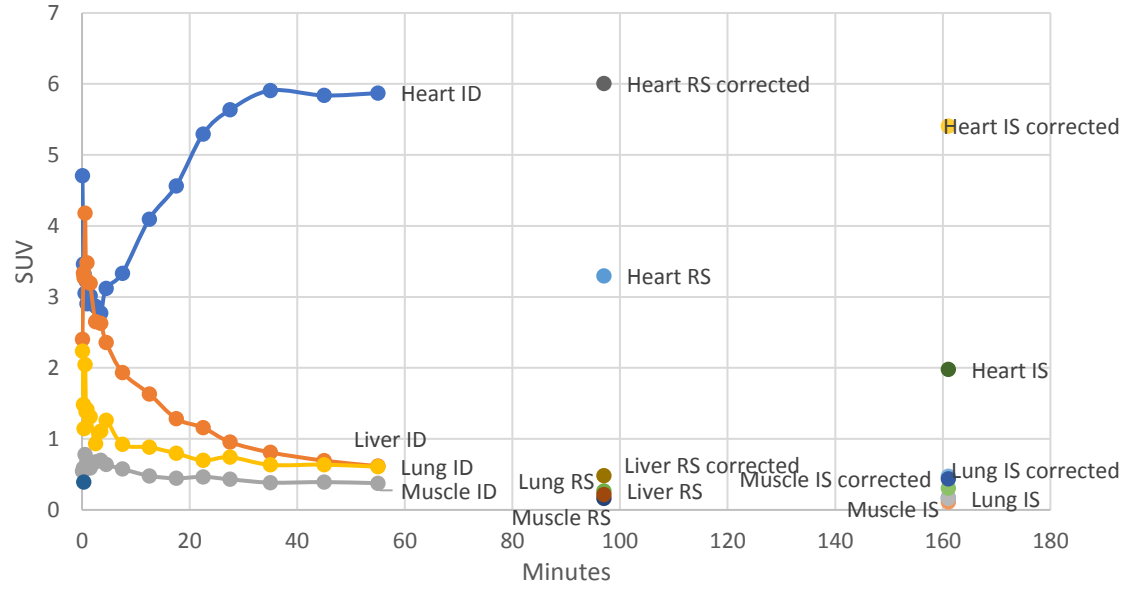

Figure 43. SUV of Rat 2 tissues. RD = Raycan Dynamic; ID = Inveon Dynamic; RS = Raycan Static; IS = Inveon Static. "Corrected" points have their activity values corrected to timepoint 0.

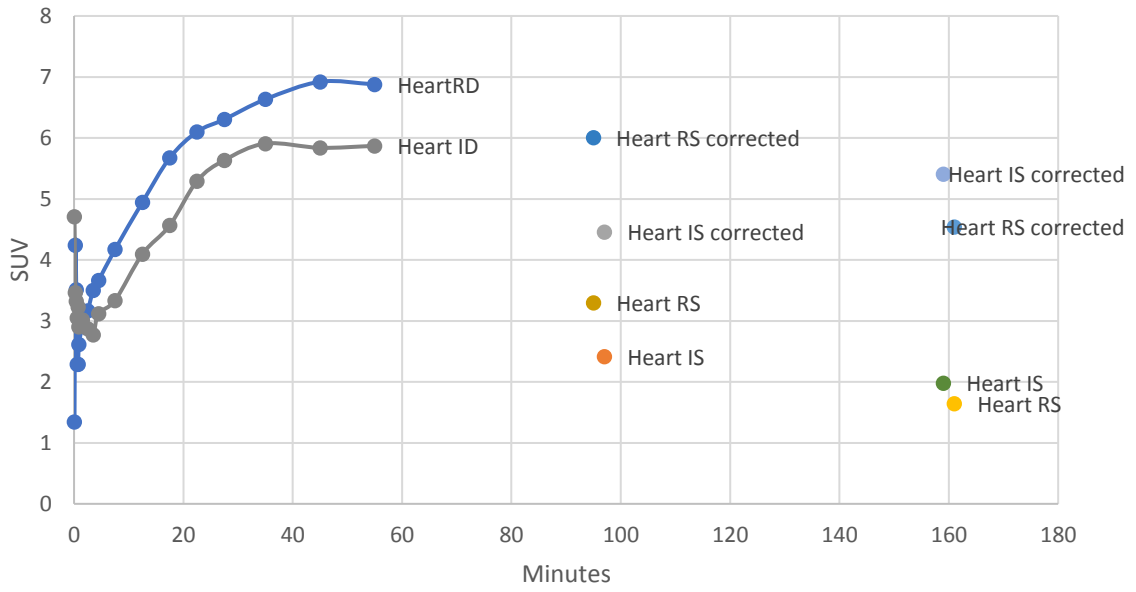

Figure 44. Heart SUV comparison of Rats 1 and 2. RD = Raycan Dynamic; ID = Inveon Dynamic; RS = Raycan Static; IS = Inveon Static. "Corrected" points have their activity values corrected to timepoint 0.

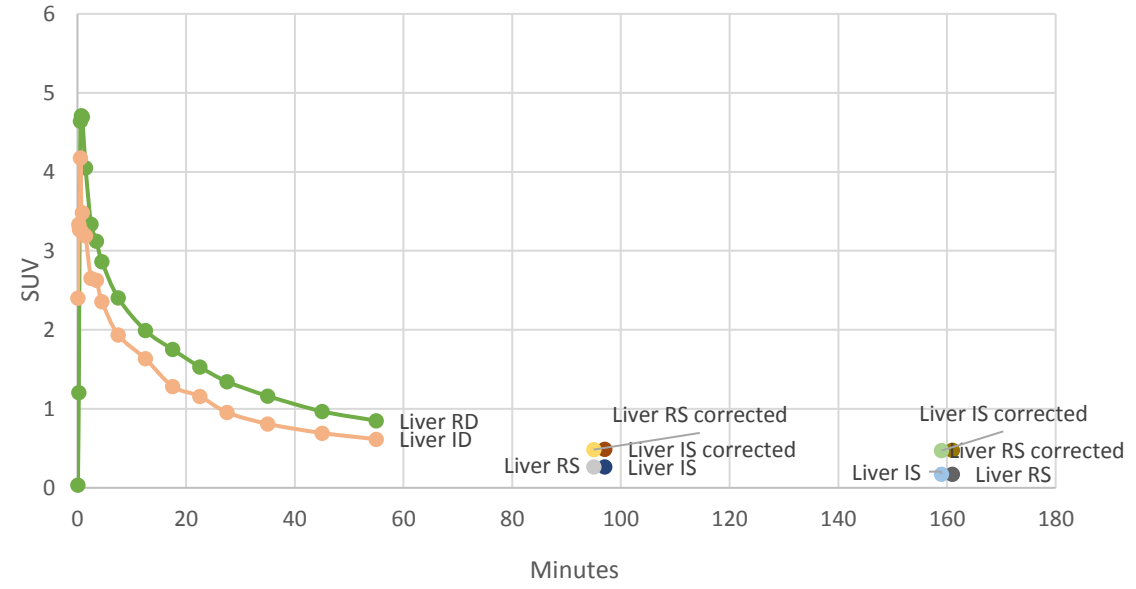

Figure 45. Liver SUV comparison of Rats 1 and 2. RD = Raycan Dynamic; ID = Inveon Dynamic; RS = Raycan Static; IS = Inveon Static. "Corrected" points have their activity values corrected to timepoint 0.

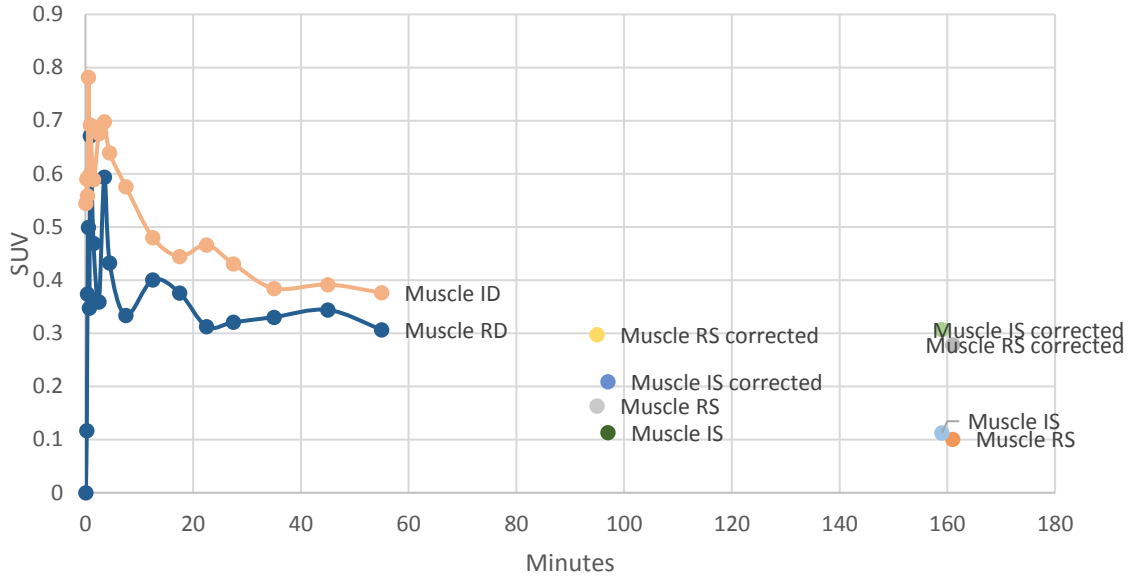

Figure 46. Muscle SUV comparison of Rats 1 and 2. RD = Raycan Dynamic; ID = Inveon Dynamic; RS = Raycan Static; IS = Inveon Static. "Corrected" points have their activity values corrected to timepoint 0.

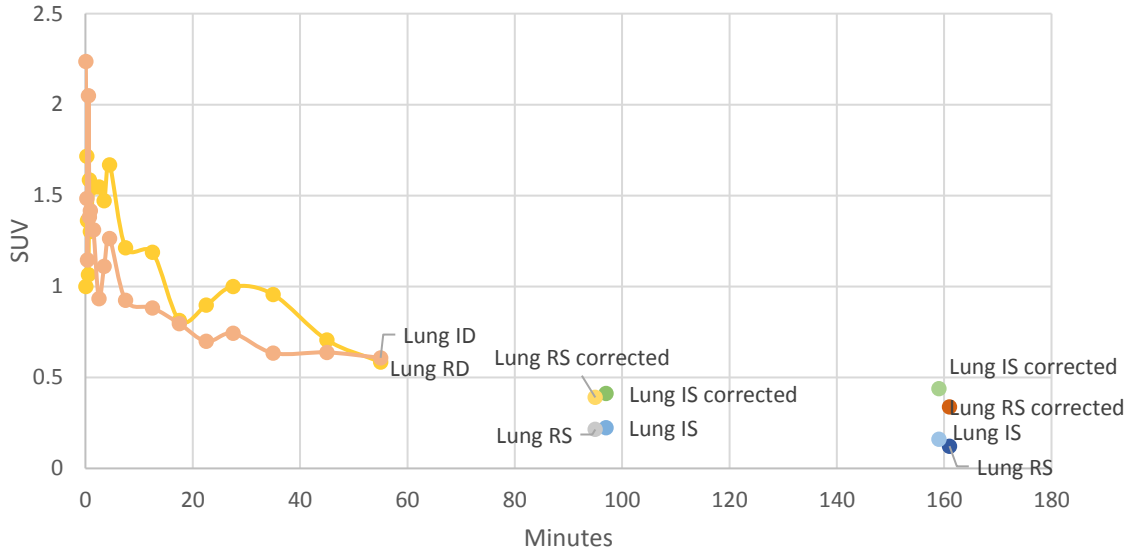

Figure 47. Lung SUV comparison of Rats 1 and 2. RD = Raycan Dynamic; ID = Inveon Dynamic; RS = Raycan Static; IS = Inveon Static. "Corrected" points have their activity values corrected to timepoint 0.

5 Discussion

According to NEMA NU 4-2008 standard and comparison with other systems, the Raycan Trans-PET/CT X5 system shows average PET module performance when compared with other preclinical positron emission tomographs on the market. While the parameters from NEMA evaluation satisfy the basic requirements for preclinical research, some of the detected issues don't let the system to reach its full potential. As the evaluated system is at prototype stage, the encountered technical challenges were expected.

Notably, in the present state, the Raycan Trans-PET/CT X5 appears to suffer from unoptimized reconstruction algorithms and poor data corrections as can be inferred from large spill-over ratio values that can be compared in Table 14 (Part 4.1.2, Image Quality comparison). The degenerating tangential spatial resolution further than 15 mm distance from center of FOV warrants further improvements to optimize the system performance to enable full use of the 130 mm transaxial FOV for multiple animal imaging. Live animal imaging comparison showed, that regardless of the problems found with numerical parameter evaluations, the Raycan system produces static imaging data that are comparable to the Inveon. The dynamic animal scans also revealed the problem with activity estimation of high concentration volumes in dynamic scans if the activity difference between first and last frame is too large, and the manufacturer has been notified about the issue.

From all the systems mentioned in this work, some can be considered as similar (Table 22). Of special interest are the short-FOV (<8 cm axial FOV) scanners that due to the intrinsic qualities of their configuration designs, should face similar technical challenges to maintain adequate performance.

Table 22. List of similar systems and their specifications.

System	aFOV (mm)	tFOV (mm)	Crystals	Detector	Attenuation/ Scatter	Energy window (keV)	Timing window
Raycan Trans-PET/CT X5	50	130	LYSO 1.9×1.9	PSMPT*	Y/N	350-650	5
microPET P4	78	190	LSO 2.2×2.2×10	PSMPT*	Y/Y	350-650	6
microPET R4	78	190	LSO 2.2×2.2×10	PSMPT*	Y/N	350-650	6
microPET Focus 220	76	190	LSO 1.51×1.51×10	PSMPT*	Y/Y	250-700	6
microPET Focus 120	76	85	LSO 1.51×1.51×10	PSMPT*	Y/Y	350-650	6
Argus	48	67	1.45×1.45×7(LYSO) 1.45×1.45×8 (GSO)	PSMPT*	Y/Y	250-700	7
VrPET	45.6	86.6	LYSO 1.4×1.4×12	PSMPT*	N/N	100-700	3.8

LabPET 8	75	100	LYSO+LGSO 2.0×2.0×14	APD**	N/N	250-650	20
rPET-1	45.6	45.6	MLS 1.4×1.4×12	PSMPT*	N/N	250-650	3.8
Raycan Trans-PET BioCaliburn LH	53	130	LYSO 1.89×1.89×13	PSMPT*	N/N	350-650	5

Note: PSMPT – position-sensitive photomultiplier tube; APD** - avalanche photodiode*

To condense the huge set of spatial resolution data (Table 21, Part 4.4.2), the effective transaxial resolution and it's relation with scintillator crystal size was calculated according to the formula used by Goertzen et al. (2012):

$$Effective\ transaxial\ resolution = \sqrt{\left(\frac{FWHM_{rad,center} + FWHM_{rad,¼}}{2}\right) \times \left(\frac{FWHM_{tan,center} + FWHM_{tan,¼}}{2}\right)} \qquad 18.$$

The results are presented in Table 23. BioCaliburn system produces resolution/crystal size value of 0.53, most likely because this was the only system that used OSEM algorithm in the test and thus can't easily be used as a reference. Another outlier system that produces the value below 1 is LabPET 8, and as suggested by Goertzen et al., this is due to individual crystal readout and irregular detector geometry. Overall, the Raycan resolution/crystal size ratio is better than of microPET Focus 120, but falls behind the other systems. However, the difference from the systems whose values are next (microPET Focus 220 and Argus) is only 0.02 and 0.03 respectively. It can be considered that altogether these 4 out of 10 systems (40%) do not have significant spatial resolution difference at 5 mm offset from axial center of FOV.

Table 23. Similar system comparison of Effective Transaxial FWHM Resolution with Crystal Size.

System	Crystal size	Effective transaxial FWHM resolution at 5 mm (mm)	Resolution/crystal size
microPET P4	2.20	2.24	1.02
microPET R4[1]	2.20	2.20	1.00
microPET Focus 120[1]	1.51	1.78	1.18
microPET Focus 220[1]	1.51	1.74	1.15
Argus[1]	1.45	1.66	1.14
VrPET[1]	1.40	1.40	1.00
LabPET 8[1]	2.00	1.64	0.82
rPET-1[2]	1.40	1.52	1.09
Raycan Trans-PET BioCaliburn LH[3]	1.89	1.00	0.53
Raycan	1.90	2.23	1.17

Notes 1-3: 1. Goertzen et al., 2012; 2. Cañadas et al., 2011; 3. Wang et al., 2015

The counting rate performance data (Table 24) are based on larger Table 19 (Part 4.3.2). As some systems had multiple energy window options, the listed ones are those that have a similar energy window to tested Raycan (and listed in Table 22).

Table 24. Similar system summary of Counting-Rate Test Results for Mouse and Rat Phantoms

		Mouse phantom				Rat phantom			
System	Randoms correction	Peak NECR (kcps)	Activity (MBq)	NECR at 3.7 MBq (kcps)	Scatter fraction (%)	Peak NECR (kcps)	Activity (MBq)	NECR at 10 MBq (kcps)	Scatter fraction (%)
microPET P4[1]	Calculated	601*	174*	22.1	5.2	173	254	19.2	16.7
microPET R4[1]	Calculated	618	156	37.2	9.3	164	137	30.5	22.2
microPET Focus 120[1]	Calculated	897	103	66.5	5.6	267	129	50.9	20.3
microPET Focus 220[1]	Calculated	763*	89*	47.3	7.2	359	162	51.8	19.3
Argus[1]	Calculated	117	50	18.7	21	40	41	20.4	34.4
VrPET[1]	Calculated	74	22		11.5	31	34		23.3
LabPET 8[1]	Calculated	279	82	23.5	15.6	94	91	19.4	29.5
rPET-1[2]		29.2	(46.4)		24.2				
LabPET 8[3]	No	183			19	67			31
Raycan Trans-PET BioCaliburn LH[4]	No	62	28		8.4	25	31		17.7
Raycan (3D michelogram)	Not used	126	52.5	16.7	13.1	55	56.53	18.9	21.9
Raycan (SSRB)	Not used	141	55.9	17	13.7	64	56.53	19.4	24.1

Notes 1-4: 1. Goertzen et al., 2012; 2. Cañadas et al., 2011; 3. Prasad et al., 2011; 4. Wang et al., 2015
**Peak value not reached because of insufficient activity at start of scan.*

At 3.7 MBq, the Raycan has similar noise equivalent count rate to Argus and is relatively close to the microPET P4 system. At 10 MBq, NECR are similar to the LabPET 8 (from the study of Goertzen et al., 2012, because the study by Prasad et al., 2011, has no relevant data), Argus and microPET P4. However, peak NECR for both mouse and rat phantoms are only similar to the Argus system. The scatter fraction parameter of the Raycan is similar to the LabPET 8, VrPET and microPET R4, with scatter fraction values difference below 5% for both mouse and rat phantoms of these systems. Overall, the sensitivity and raw count capability of the tested Raycan system is comparable to the Argus and close to the microPET P4 and LabPET 8, also possibly to the VrPET (considering that both NECR peak and activities for both phantoms are stably around half of Raycan). The performance of the rest of the systems suggests better sensitivity and counting ability. From scatter fraction, the performance of the tested Raycan is also close to the LabPET 8 and VrPET, with the result being average, if the significantly well-performing microPET-line systems are not counted.

When comparing sensitivities (Table 25), the Raycan has peak detection efficiency similar to the BioCaliburn and microPET R4 systems. This is, in turn, better than the

microPET P4 and LabPET 8 performance values reported by Prasad et al. (2011). However, it is interesting that the peak detection efficiency reported by Prasad is significantly different from identical system reported by Goertzen (1.33% vs. 2.36%). The reason behind such significant difference remains unconfirmed. For the average sensitivity values, similar to the Raycan are the microPET Focus 220, microPET R4 and VrPET. Based on counting rate test data, the actual system sensitivity of the Raycan is similar to VrPET, with other systems having little continuity between different parameters.

Table 25. Similar system summary for sensitivity results.

System	Average mouse sensitivity (%)	Average total sensitivity (%)	Peak detection efficiency (%)
microPET P4[1]	0.67	0.61	1.19
microPET Focus 220[1]	1.26	1.18	2.28
microPET R4[1]	1.19	1.1	2.06
microPET Focus 120[1]	1.98	1.82	3.42
Argus[1]			4.32
VrPET[1]	1.09	1.09	2.22
LabPET 8[1]	1.45	1.42	2.36
rPET-1[2]	0.46	0.46	1.0 (100-700 keV)
LabPET 8[3]			1.33
Raycan Trans-PET BioCaliburn LH[4]			2.04
Raycan (3D mich)	1.01	1.01	1.82
Raycan (SSRB)	0.9	0.9	1.72

Notes 1-4: 1. Goertzen et al., 2012; 2. Cañadas et al., 2011; 3. Prasad et al., 2011; 4. Wang et al., 2015

Table 27 is based on larger Table 14 (Part 4.1.2) and compares the Image Quality test results. NEMA Image Quality test assumes the use of typical imaging and reconstruction parameters, which for Raycan would be 3D OSEM with post filter set to Low. At these settings, the Raycan has Uniformity standard deviation values close to the microPET systems, Argus, LabPET 8 and rPET-1. The VrPET and BioCaliburn systems perform generally worse. The recovery coefficients in different sized rods of Raycan are close to the values reported for the microPET systems and the BioCaliburn. SOR values for Raycan system are largely similar to rPET-1 system, which despite using both attenuation and scatter corrections, preforms somewhat worse than the non-corrected VrPET and

significantly worse than the microPET line of systems that also implement both corrections while reconstructed using FBP algorithm. Also, another case of disparity in the LabPET 8 evaluations performed by Goertzen et al. (2012) and Prasad et al. (2013) suggests that for individual systems, the use of different softwares and individual VOI placements can sometimes affect results more than the technical characteristics of the systems.

Table 26. Similar system summary of Image Quality phantom test results.

				Uniform Region	Recovery coefficients					Spillover ratios (%)	
System	Energy window (keV)	Recon. algorithm	Attenuation/ Scatter correction	%SD	1 mm	2 mm	3 mm	4 mm	5 mm	Water	Air
microPET P4[1]	350-650	FORE + 2D FBP	Y/Y	5.2	0.11	0.37	0.6	0.77	0.86	4.9	4
microPET Focus 220[1]	250-700	FORE + 2D FBP	Y/Y	6.8	0.15	0.41	0.63	0.74	0.86	1.2	4.1
microPET R4[1]	350-650	FORE + 2D FBP	Y/N	4.5	0.14	0.35	0.6	0.79	0.87	6.2	4.6
microPET Focus 120[1]	350-650	FORE + 2D FBP	Y/Y	6	0.15	0.18	0.75	0.86	0.93	1.8	20.3
Argus[1]	250-700	3D OSEM	Y/Y	6	0.27	0.65	0.93	0.95	0.97	15	13
VrPET[1]	100-700	3D OSEM	N/N	15.4	0.22	0.62	0.72	0.75	0.75	9.3	8.5
LabPET 8[1]	250-650	2D MLEM	N/N	6	0.19	0.78	0.97	1	1.02	24.4	13.7
rPET-1[2]	250-650	3D OSEM	N/N	6.9	0.14	0.46	0.66	0.76	0.81	15	24
LabPET 8[3]	250-650	2D MLEM	N/N	7	0.13	0.32	0.58	0.83	0.96	20	11
Raycan Trans-PET BioCaliburn LH[4]	350-650	3D OSEM	N/N	9.94	0.16		0.76		0.89	9.2	17.7
Raycan	350-650	SSRB + 2D FBP Low Filter	Y/N	4.32	0.09	0.18	0.36	0.57	0.67	8.5	17.5
Raycan	350-650	SSRB + 2D FBP No Filter	Y/N	19.2	0.14	0.27	0.47	0.71	0.76	8	16.3
Raycan	350-650	3D OSEM + PSF Low Filter	Y/N	4.59	0.1	0.4	0.73	0.93	0.87	14.3	22.8
Raycan	350-650	3D OSEM + PSF No Filter	Y/N	5.72	0.11	0.48	0.82	0.98	0.88	14.2	22.4

Notes 1-4: 1. Goertzen et al., 2012; 2. Cañadas et al., 2011; 3. Prasad et al., 2011; 4. Wang et al., 2015

From the gathered data, the system with highest absolute peak sensitivity is the Argus (4.32%), although its aFOV is 48 mm, third shortest after the r-PET and the VrPET (both 45.6 mm). These systems also have smaller than average transaxial FOV and the peak absolute sensitivity of the VrPET is also one of the best among the similar systems. At the same time, the microPET systems P4, R4 and Focus220 that have largest axial FOVs (78, 78 and 76 mm respectively) also have largest transaxial FOVs (190 mm) and their peak absolute sensitivity varies from 1.19% to 2.28%. Considering that the Raycan produces 1.82% with 50×130 mm FOV, it should be noted that the FOV dimensions are not the only major deciding factor deciding the sensitivity of the systems. It is possible, that the technical configuration of each system has different optimal energy and timing window parameters for specific imaging modes. For example, system sensitivity is

affected by factors as the detector crystal material, detector design and intrinsic dimensions, implemented coincidence processing (e.g. integration time), the selected energy window, the selected coincidence window, and so on.

While peak NECR also appear to be higher for the longer aFOV systems (microPET), this is more likely a result of intrinsic detector and gantry designs differences, as they are all produced by the same manufacturer. The scatter fraction values of the Raycan are average among the non-microPET systems, as the latter show relatively stable better-than-average performance compared to the rest of the systems. The spill-over ratios of the Raycan behave similarly to scatter fraction data, being average among the non-microPET systems. Considering that the microPET systems produce good results with both corrections, despite using FBP reconstruction algorithm, it can be assumed that iterative algorithms require highly precise and efficient corrections for adequate performance.

While working on this project, each section posed challenges of varying difficulty in both technical difficulties and interpretation of the NEMA guidelines. Among other things, the Raycan scanner bed had a 39 mm axial shift to the front in respect to the initial position after the conclusion of PET scan, thus requiring manual bed repositioning during repeated scans such as Sections 3 (Spatial Resolution), 4 (Scatter Fraction, Count Losses and Random Coincidence) and 5 (Sensitivity). Section 6 (Image Quality, Accuracy of Attenuation and Scatter Correction) had straightforward and generally clear guidelines. Nevertheless, the efficiency could be raised by providing visual schematics for different tests and clear formulas for each calculation. “Recovery Coefficients” (NEMA NU 4-2008 6.4.2) part could be made significantly more clear by adding visual instruction to compliment the written text that was found to be cumbersome to follow for non-native English speakers. “Accuracy of Corrections” (NEMA NU 4-2008 6.4.3) stated that spill-over ratio is to be reported as “the ratio of the mean in each cold region to the mean of the hot region”, which mathematically can be either represented as two constituting numbers (a:b) or their quotient (result of division). However, most system evaluations starting from Goertzen et al. (2012) present SOR as percentage, multiplying the ratio quotient by 100. Therefore, because the reporting formats are not always uniformly followed or accurately explained in all studies, it requires extra attention when comparing published results from different papers.

Since the scout CT scan is not implemented and positioning by hand using only positioning lasers is imprecise and inconvenient for small three-dimensional objects, Section 5 (Sensitivity) test carried a risk of phantom misalignment. The issue was partially solved by positioning cubic 22-Na source at an angle, using the corners for laser alignment. However, the problem of 39 mm shift after each scan, misalignments during initial positioning and the need for repeated measurements increased the risk of human errors and turned this test into a time-consuming and intense data acquisition session due to the required 101 scan points. At the same time, Section 5 is the only test that has been evaluated as successfully adjusted and refined by independent study (Elhami et al., 2011), with suggested replacement of multiple point source scans with a single line source used for NEMA clinical PET testing. But as the suggested adjustment has not yet been adapted by NEMA, this study followed the original guidelines. The analysis of Section 5 also included text that could be improved by referring to visual instructions with formulas, which would allow to form clear overview of the procedure. The use of robotic arms could be adapted to ensure accurate and reproducible positioning of the source in Sections 5 and 3.

Section 4 (Scatter Fraction, Count Losses and Random Coincidence) is the most time-consuming test requiring around 10 hours of carefully timed acquisitions. The main problem encountered was precise dosage of high activity (~100 MBq) into small volume line sources (0.11 and 0.22 ml). During the data collection, it was necessary for the operator to maintain the focus to remember to adjust the 39 mm axial shift between the scans and follow the acquisition timetable. The data acquisition procedure could be improved by implementing a fully automated acquisition protocol to perform the scans automatically, as it is already realized in well counter correction acquisition for system calibration. For data analysis, this section was most calculation-heavy and presented some difficulties in interpreting the calculation steps, mostly because of considerably nonlinear and partially overlapping instructions for scatter fraction calculation of systems with intrinsic activity.

By requiring multiple acquisitions at different positions, Section 3 (Spatial Resolution) causes technical difficulty similar to Section 5 – accurate point source positioning through the FOV, further complicated by arched bed surface. While a piece of cardboard solved the problem with bed surface, the required positioning precision of ±0.5 mm is literally impossible to achieve due to misaligned laser and yet unimplemented scouting CT scan.

The diagram for source positioning (NEMA NU 4-2008 3.3.3) could also be more detailed, for example drawn in 3D perspective, notably including relative positions of center-FOV and ¼-FOV axial scan locations. In the beginning, we misinterpreted that the acquisition points should be distributed through the FOV, with the measurement points spreading into horizontal, vertical and axial direction from the center of FOV, until the format of the results table and other studies helped to realize the error. Furthermore, this section specifies the use of 2D or 3D FBP reconstruction algorithm, which is of pressing concern for evaluating systems that are unsuitable for or lacking the FBP reconstruction option, such as the LabPET (Goertzen et al., 2012), PETbox4 (Gu et al., 2013), Albira (Spinks et al., 2014; Pajak et al., 2016), and the Raycan Trans-PET BioCaliburn LH (Wang et al., 2015).

This work confirmed the need for standardization of preclinical PET systems and their evaluation procedures. While NEMA NU 4-2008 standard efficiently categorizes the evaluation tests, it lacks the necessary detail and flexibility. The encountered challenges and suggested resolutions were:

- Positioning difficulty. Due to the missing scouting CT scan and possibly misaligned positioning laser, causing a systematic shift of approximately 1 mm in the axial direction it is difficult to ensure exact centering of phantoms in mid-FOV. It should be noted that in NEMA NU 4-2008 testing, the required positioning accuracy is in the range of 1 mm. Manufacturer has been informed of the issue and promised the adjustments in nearby future. Also, it may be an option to structurally mark the phantoms (e.g. small protuberances in central locations of phantoms) for positioning with scouting CT scan or external laser. PET gantries could also have clearly marked FOV in relation to the beds' zero position, allowing to precisely calculate the required bed location.
- Guidelines can be open for interpretation. Over the course of this work, we encountered cases such as in Section 6 (Image Quality, Accuracy of Attenuation and Scatter Correction), Section 4 (Scatter Fraction, Count Losses and Random Coincidence) and Section 3 (Resolution) where the NEMA instructions were open to interpretation. That required comparison of papers and discussions between people, slowing the work and reducing the overall efficiency. That could be solved by refining the instructions, notably by making them linear (step-by-step) and complement with visual diagrams.

- Systems not supporting the algorithms required for NEMA evaluation. Multiple works claiming the evaluation of their systems according to NEMA NU 4-2008 standards could not follow the provided guidelines due to the system characteristics such as missing option for FBP algorithm reconstruction required for spatial resolution test, for example in systems with irregular crystal geometry (Part 4.4). Currently, this issue can't be solved directly. The use of iterative algorithms for resolution evaluation of the systems with irregular detector geometry, while traditional systems use FBP, is likely to cause bias in results and can't be easily circumvented. This creates an obstacle in adequate comparison between systems, as the iterative algorithms have been shown to produce systematically better resolution values than FBP.
- Different data processing approaches and human errors. In Section 6 (Image Quality, Accuracy of Attenuation and Scatter Correction), VOI positioning in most analysis programs is done by hand that can potentially cause errors in resulting measurements. In Section 5 (Sensitivity) and 4 (Scatter Fraction, Count Losses and Random Coincidence) the differences in original data format cause small, but detectable differences that could be potentially avoided. That can potentially be resolved by introducing specialized evaluation software (from manufacturers or e.g. NEMA). Meanwhile, the issue remains that not all studies mention detailed information such as the slice thickness, the original sinogram data type and the type of rebinning performed on the data. At the same time, a significant part of the publications do not follow the NEMA report formats, further complicating any comparisons.
- No automatization. Similar to other studies (Elhami et al., 2011), it was felt that the automatic workflow sequences can significantly improve the quality of work. Tests such as Section 4 (Scatter Fraction, Count Losses and Random Coincidence), requiring multiple hours of precisely timed scan sessions, or Sections 3 and 5 that are dependent on precise positioning, could be done much more efficiently if acquisition times, durations and bed positions could be scheduled in advance.
- PiSYS software provided by RAYCAN also includes quality control feature with options corresponding to NEMA NU 4-2008 evaluation. Unfortunately, it was found to be yet unfunctional as the tool is still a work in progress. However, as an idea and a practical attempt, it shows a practical need for specialized evaluation software. While a single, official cross-platform program is unlikely due to

different data formats, it should be possible for manufacturers to supply their own evaluation software.

In conclusion, it was determined that Raycan Trans-PET/CT X5 small animal imaging system prototype currently has average performance compared to similar systems available on the market. However, considering the improvement potential and the upgrades promised by manufacturer, it is a promising system with competitive prospects in the global market.

Acknowledgements

I would like to thank everyone who guided and helped me through this Master's thesis. Without all the help I received, this work would have been impossible. I want to specially thank:

Professor Anne Roivainen, who responded to my enquiry and referred me to the group that had been working with Raycan scanner and provided valuable advice during the project.

Doctor Chunlei Han, who told me about the project and provided a significant portion of references, and reminded me that I would like to visit China again some day.

Doctor Jarmo Teuho, who was my supervising PhD student, tutor and main deciding force behind the project. Congratulations for successfully defending his thesis.

Aake Petteri Honkaniemi, the actual lord of small animal imaging section of Turku PET Centre, who took care of scan schedules, tracer orders and generally ensured that everything works as it should.

Marko Tirri, for radiation safety training and help with Inveon data.

Heidi Liljenbäck and Helena Virtanen, who assisted with animal imaging.

Jenni Virta, who helped to analyze animal data.

Trainees from the Physics Department, with whom I had fun.

And of course, my family and friends who supported me during my studies.

References

Aide, N., E.P. Visser, S. Lheureux, N. Heutte, I. Szanda and R.J. Hicks. 2012. The motivations and methodology for high-throughput PET imaging of small animals in cancer research. *Eur J Nucl Med Mol Imaging.* 39:1497-1509.

Anand, S.S., H. Singh and A.K. Dash. 2009. Clinical Applications of PET and PET-CT. *Med J Armed Forces India.* 65(4):353-358.

Bailey, D.L., J.L. Humm, A. Todd-Pokropek and A. van Aswegen. 2014. *Nuclear Medicine Physics: A Handbook for Teachers and Students*. International Atomic Energy Agency, Vienna, 736 pp.

Cañadas, M., M. Embid, E. Lage, M. Desco, J.J. Vaquero and J.M. Pérez. 2011. NEMA NU 4-2008 Performance Measurements of Two Commercial Small-Animal PET Scanners: ClearPET and rPET-1. *IEEE Transactions on Nuclear Science*. 58(1):58-65.

Dahle, T.J. 2014. Performance Evaluation of a Small-Animal PET/CT System. Master's thesis, University of Bergen.

Elhami, E., J. Boulding and A.L. Goertzen. 2011. Variations on the NEMA NU 4-2008 Testing Procedures and Effect on the Performance Measurement Results. *IEEE Nuclear Science Symposium Conference Record*.

Fahey, F.H. 2002. Data acquisition in PET imaging. *J Nucl Med Technol*. 30(2):39-49.

Goertzen, A.L., Q. Bao, M. Bergeron, E. Blankemeyer, S. Blidner, M. Cañadas, A.F. Chatziioannou, K. Dinelle, E. Elhami, H.-S. Jans and others. 2012. NEMA NU 4-2008 Comparison of Preclinical PET Imaging Systems. *J Nucl Med*. 53(8):1300-1309.

Gong, K., S.R. Cherry and J. Qi. 2016. On the assessment of spatial resolution of PET systems with iterative image reconstruction. *Phys Med Biol*. 61(5):N193-N202.

Gu, Z., R. Taschereau, N.T. Vu, H. Wang, D.L. Prout, R.W. Silverman, B. Bai, D.B. Stout, M.E. Phelps and A.F. Chatziioannou. 2013. NEMA NU-4 performance evaluation of PETbox4, a high sensitivity dedicated PET preclinical tomograph. *Phys Med Biol*. 58(11):3791-3814.

Gu, Z., D.L. Prout, R.W. Silverman, H. Herman, A. Dooraghi and A.F. Chatziioannou. 2015. A DOI Detector With Crystal Scatter Identification Capability for High Sensitivity and High Spatial Resolution PET Imaging. *IEEE Trans Nucl Sci*. 62(3):740-747.

Habte, F., G. Ren, T.C. Doyle, H. Liu, Z. Cheng and D.S. Paik. 2013. Impact of a Multiple Mice Holder on Quantitation of High-Throughput MicroPET Imaging With and Without Ct Attenuation Correction. *Mol Imaging Biol.* 15(5):569-575.

Hsu, D.F.C., D.L. Freese, P.D. Reynolds, D.R. Innes and C.S. Levin. 2018. Design and Performance of a 1 mm^3 Resolution Clinical PET System Comprising 3-D Position Sensitive Scintillation Detectors. *IEEE Trans Med Imaging*. 37(4):1058-1066

Iriarte, A., R. Marabini, S. Matej, C.O.S. Sorzano and R.M. Lewitt. 2016. System models for PET statistical iterative reconstruction: A review. *Comput Med Imaging Graph*. 48:30-48.

Jones, C. and R. Klein. 2015. Can PET be performed without an attenuation scan? *J Nucl Cardiol*. 23(5):1098–1101

Levin, C.S. and H. Zaidi. 2007. Current Trends in Preclinical PET System Design. *PET Clin.* 2(2):125-60.

Mannheim, J.G., F. Kara, J. Doorduin, K. Fuchs, G. Reischl, S. Liang, M. Verhoye, F. Gremse, L. Mezzanotte and M.C. Huisman. 2017. Standardization of Small Animal Imaging—Current Status and Future Prospects. *Mol Imaging Biol*. DOI: 10.1007/s11307-017-1126-2.

Ming, N. 2017. Trans-PET/CT User manual. RAYCAN.

Nagy, K., M. Tóth, P. Major, G. Patay, G. Egri, J. Häggkvist, A. Varrone, L. Farde, C. Halldin and B. Gulyás. 2013. Performance Evaluation of the Small-Animal nanoScan PET/MRI System. *J Nucl Med*. 54:1825-1832.

National Electrical Manufacturers Association. 2008. Performance Measurements for Small Animal Positron Emission Tomographs. NEMA Standard Publication NU 4-2008.

Nolting, D.D., M.L. Nickels, N. Guo and W. Pham. 2012. Molecular imaging probe development: a chemistry perspective. *Am J Nucl Med Mol Imaging*. 2(3):273-306

Pajak, M.Z., D. Volgyes, S.L. Pimlott, C.C. Salvador, A.S. Asensi, C. McKeown, J. Waldeck and K.I. Anderson. 2016. NEMA NU 4-2008 Performance Evaluation of Albira: A Two-Ring Small-Animal PET System Using Continuous LYSO Crystals. *Open Medicine Journal*. 3:12-26.

Podoloff, D.A., R.H. Advani, C.P. Allred, A.B. Benson, E.A. Brown, H.J. Burstein, R.W. Carlson, R.E. Coleman, M.S. Czuczman, D. Delbeke, et al. 2007. *J Natl Compr Canc Netw*. 5 Suppl 1:S1-22

Prasad, R., O. Ratib and H. Zaidi. 2010. Performance Evaluation of the FLEX Triumph X-PET Scanner Using the National Electrical Manufacturers Association NU-4 Standards. *J Nucl Med*. 51:1608-1615.

Prasad, R., O. Ratib and H. Zaidi. 2011. NEMA NU-04-based performance characteristics of the LabPET-8^{TM} small animal PET scanner. *Phys. Med. Biol*. 56:6649-6664.

Roncali, E. and S.R. Cherry. 2011. Application of Silicon Photomultipliers to Positron Emission Tomography. *Ann Biomed Eng*. 39(4):1358-77.

Sánchez-Crespo, A. and S.A. Larsson. 2006. The influence of photon depth of interaction and non-collinear spread of annihilation photons on PET image spatial resolution. *Eur J Nucl Med Mol Imaging*. 33(8):940-7.

Sato, K., M. Shidahara, H. Watabe, S. Watanuki, Y. Ishikawa, Y. Arakawa, Y.H. Nai, S. Furumoto, M. Tashiro, T. Shoji, et al. 2016. Performance evaluation of the small-animal PET scanner ClairvivoPET using NEMA NU 4-2008 Standards. *Phys. Med. Biol*. 61:696-711.

Serdons, K., A. Verbruggen and G.M. Bormans. 2009. Developing new molecular imaging probes for PET. *Methods.* 8(2):104-11.

Spinks, T.J., D. Karia, M.O. Leach and G. Flux. 2014. Quantitative PET and SPECT performance characteristics of the Albira Trimodal pre-clinical tomograph. *Phys. Med. Biol*. 59:715-731.

Studen, A., D. Burdette, E. Chesi, V. Cindro, N.H. Clinthorne, E. Cochran, B, Grošičar, H. Kagan, C. Lacasta, V. Linhari, et al. 2010. Timing performance of the silicon. PET insert probe. *Radiat Prot Dosimetry*. 139(1-3):199-203.

Szanda, I., J. Mackewn, G. Patay, P. Major, K. Sunassee, G.E. Mullen, G. Nemeth, Y. Haemisch, P.J. Blower and P.K. Marsden. 2011. National Electrical Manufacturers Association NU-4 Performance Evaluation of the PET Component of the NanoPET/CT Preclinical PET/CT Scanner. *J Nucl Med*. 52:1741-1747.

Tong, S., A.M. Alessio and P.E. Kinahan. 2010. Image reconstruction for PET/CT scanners: past achievements and future challenges. *Imaging Med*. 2(5):529-545.

Turkington, T.G. 2011. PET Imaging Basics. In: *Clinical PET-CT in Radiology: Integrated Imaging in Oncology* (edited by Shreve P. and D.W. Townsend), pp. 21-28. Springer-Verlag, New York.

Vandenberghe, S., E. Mikhaylova, E. D'Hoe, P. Mollet and J.S. Karp. 2016. Recent developments in time-of-flight PET. *EJNMMI Phys.* 3:3.

Vanhove, C., J.P. Bankstahl, S.D. Krämer, E. Visser, N. Belcari and S. Vandenberghe. 2015. Accurate molecular imaging of small animals taking into account animal models, handling, anaesthesia, quality control and imaging system performance. *EJNMMI Phys.* 2:31.

Vaquero, J.J. and P. Kinahan. 2015. Positron Emission Tomography: Current Challenges and Opportunities for Technological Advances in Clinical and Preclinical Imaging Systems. *Annu Rev Biomed Eng*. 17:385-414.

Wang, L., J. Zhu, X. Liang, M. Niu, X. Wu, C.-M. Kao, H. Kim and Q. Xie. 2014. Performance evaluation of the Trans-PET® BioCaliburn® LH system: a large FOV small-animal PET system. *Phys. Med. Biol*. 60: 137-150.

Wong, W.-H., H. Li, H. Baghaei, Y. Zhang, R.A. Ramirez, S. Liu, C. Wang and S. An. 2012. Engineering and Performance (NEMA and Animal) of a Lower-Cost Higher-Resolution Animal PET/CT Scanner Using Photomultiplier-Quadrant-Sharing Detectors. *J Nucl Med*. 53:1786-1793.

Yao, R., R. Lecomte and E.S. Crawford. 2012. Small-Animal PET: What Is It, and Why Do We Need It? *J Nucl Med Technol*. 40(3):157-165.

Appendices

Measurement protocol for the spatial resolution (NEMA Section 3)

Date: _____

Radionuclide: 22Na

Phantom: 1×1 cm cube with 0.3 mm point source in the centre

10^5 (100 000) prompt counts acquired per measurement

Acquisition duration for each measurement (seconds): _____

Source activity (MBq): _____

Activity measurement time (hh:mm): _____

Scan start at (hh:mm): _____

System used: _____

Raycan PET FOV:

130 mm transaxial (radial and tangential radius – 65 mm).

50 mm axial (maximum axial radius 25 mm).

¼ axial FOV is 12.5 mm.

Siemens Inveon PET FOV:

100 mm transaxial (radial and tangential radius – 50 mm).

127 mm axial (maximum axial radius 63.5mm)

¼ axial FOV is 31.75 mm

Data processing – Reconstruction by 2D and 3D filtered back projection, with no smoothing for all spatial resolution data.

Reconstruction parameters:

Slice thickness: _____

Zoom: _____

Pixel size: _____

Measurement sheet:

1) Centre of axial FOV
   Bed position:
   Horizontal axial ↔ (mm): _____
   Vertical ↕ (mm): _____
   a. Zero point
      i. Zero point Acquisition duration: _____
   b. Radial offset
      i. 5 mm Acquisition duration: _____
      ii. 10 mm Acquisition duration: _____
      iii. 15 mm Acquisition duration: _____
      iv. 25 mm Acquisition duration: _____
      v. 50 mm Acquisition duration: _____

2) +¼ of axial FOV
   Bed position:
   Horizontal axial ↔ (mm): _____
   Vertical ↕ (mm): _____
   a. Zero point
      i. Zero point Acquisition duration: _____
   b. Radial offser
      i. 5 mm Acquisition duration: _____
      ii. 10 mm Acquisition duration: _____
      iii. 15 mm Acquisition duration: _____
      iv. 25 mm Acquisition duration: _____
      v. 50 mm Acquisition duration: _____

3) +¼ of axial FOV
   Bed position:
   Horizontal axial ↔ (mm): _____
   Vertical ↕ (mm): _____
   a. Zero point
      i. Zero point Acquisition duration: _____
   b. Radial offser
      i. 5 mm Acquisition duration: _____
      ii. 10 mm Acquisition duration: _____
      iii. 15 mm Acquisition duration: _____
      iv. 25 mm Acquisition duration: _____
      v. 50 mm Acquisition duration: _____

Measurement protocol for the scatter fraction and count rate phantom (NEMA Section 4)

Mark the phantom:

Rat phantom: set bed height at 19.50 mm, injected volume is about 0.22 ml

Mouse phantom: set bed height at 32.00 mm, injected volume is about 0.11-12 ml

Energy window: _____

Date: _____

1) Perform a background scan without the line source insert (Intrinsic True Count rate scan):
    a. Place the phantom mid-FOV, as in actual scan
    b. Perform a PET scan without any activity for 5 minutes
    c. Mark the scan time:
        i. Scan started at:_____

2) Fill the line source for phantom with the required amount of activity
    a. Suggested initial activity is 100 MBq at the start of the scan
    b. The point source should have active length 10 mm shorter than phantom
    c. Inject the required activity, so that it is contained between the middle of two black lines in the insert (it may not be perfect)
    d. Seal the line source open end with wax
    e. Insert the source into the middle of the hole using the two outer black lines as starting and end points
    f. Mark the injected activity and injection time:
        i. Injection time (hh:mm):_____
        ii. Injected activity (MBq):_____

3) Place the phantom in the PET/CT system
    a. Place the phantom so that the source is closest to the subject bed
    b. Center the phantom in the transverse and axial field-of-view within 1 mm precision using the lasers and the bed height specified above
    c. From PiSYS, select the “Motion controller” option
    d. Mark the bed position below (once centered with the lasers):
        i. Left and right arrow (mm):_____
        ii. Up and down arrow (mm):_____

4) Actual imaging (PET only)
    a. Start PET scan at the specified time mark and begin timing with stopwatch etc.
    b. Mark the start time of the first PET acquisition
        i. PET acquisition start (hh:mm):_____
    c. When the PET scan is finished, open “Motion Controller”
        i. Select “Steps”, insert value 39.00 mm and click right arrow
        ii. Check that the bed coordinates match what was written above

iii. If not, then adjust with necessary step size and clicking the arrows

d. Start the next PET scan as specified in TABLE 1
e. For each PET scan, repeat steps c to d until finished

Perform PET scans of the phantom following the intervals below.

The times mark the starting points in hh:mm format. After each point, a PET scan with acquisition length of 5 minutes is performed (to acquire a minimum of 500,000 prompt counts).
Motion Control: insert value 39.00 mm and click right arrow. Horizontal bed position _____ mm.

Mark down the starting point of each scan in the table (needed for analysis). Count rate is for statistics.

	TABLE 1. Required time points to collect each individual 5 min scans.		
	Time Mark to Start Scan	Actual Scan Start Time	Kilocounts per second (kcps)
	Background		
1	0:00		
2	0:07		
3	0:14		
4	0:21		
5	0:28		
6	0:35		
7	0:42		
8	0:49		
9	0:56		
10	1:06		
11	1:16		
12	1:26		
13	1:36		
14	1:46		
15	1:56		
16	2:21		
17	2:46		
18	3:11		
19	3:36		
20	4:01		
21	4:26		
22	4:51		
23	5:26		
24	6:01		
25	6:36		
26	7:11		
27	7:46		
28	8:21		
29	8:56		
30	9:31		
31	10:06		
32	10:41		
33	11:16		
34	11:51		
35	12:26		
36	13:01		
37	13:36		
38	14:11		
39	14:46		
40	15:21		

Raycan measurement protocol for sensitivity phantom (NEMA Section 5)

Set bed height at 45.00 mm, imaging time for each time point is 60 seconds

1) Perform a background scan without the phantom:
    a. Perform a PET scan without any activity for 1 minute
    b. Mark the scan time and background count rate:
        i. Scan started at: _____
        ii. Background count rate: _____

2) Measure the activity of the phantom in a dose calibrator
    a. Mark the measured activity and time:
        i. Measurement time (hh:mm): _____
        ii. Phantom activity (MBq): _____

3) Place the phantom in the PET/CT system mid-FOV
    a. Place the phantom at the specified bed height
    b. Center the phantom in the transverse and axial FOV using the lasers
    c. From PiSYS, select the "Motion controller" option
    d. Mark the bed position below before moving to PET (once centered with the lasers):
        i. ↔ (mm): _____
        ii. ↕ (mm): 45.00

4) When performing the actual imaging (PET only scan)
    a. Start from the Centre FOV PET scan
        i. Select "New Scan"
        ii. Description "0 mm"
        iii. Click so-called "Magic Button".
    b. When the PET scan is finished, open "Motion Controller"
        i. Select "Steps", insert value (39 + desired step ±0.5), click → (right arrow)
        ii. Check that the bed coordinates match to desired bed position
        iii. If not, then adjust with necessary step size and clicking the arrows
        iv. Mark down the bed coordinates in the table
    c. Start the next PET scan as specified in TABLE 1
        i. New Scan description: current step.
        ii. Click "Magic Button"
    d. For each PET scan, repeat steps b to c until finished

Start from the Centre FOV and move to +0.5 mm steps up to +25.0 mm from the Centre FOV, then move in -0.5 mm steps up to – 25.0 mm from the Centre FOV.

At each point, a PET scan with acquisition length of 1 minute is performed (to acquire a minimum of 10,000 prompt counts). The step size in the measurement is 0.5 mm. Mark down the left and right arrow coordinates of each scan in the table in xxx,yy format

TABLE 1. Required time points to collect each individual 1 min scans.			
	Bed Position Location		Bed Position Location
Background		Centre FOV	
0.5		-0.5	
1.0		-1.0	
1.5		-1.5	
2.0		-2.0	
2.5		-2.5	
3.0		-3.0	
3.5		-3.5	
4.0		-4.0	
4.5		-4.5	
5.0		-5.0	
5.5		-5.5	
6.0		-6.0	
6.5		-6.5	
7.0		-7.0	
7.5		-7.5	
8.0		-8.0	
8.5		-8.5	
9.0		-9.0	
9.5		-9.5	
10.0		-10.0	
10.5		-10.5	
11.0		-11.0	
11.5		-11.5	
12.0		-12.0	
12.5		-12.5	
13.0		-13.0	
13.5		-13.5	
14.0		-14.0	
14.5		-14.5	
15.0		-15.0	
15.5		-15.5	
16.0		-16.0	
16.5		-16.5	
17.0		-17.0	
17.5		-17.5	
18.0		-18.0	
18.5		-18.5	
19.0		-19.0	
19.5		-19.5	
20.0		-20.0	
20.5		-20.5	
21.0		-21.0	
21.5		-21.5	
22.0		-22.0	
22.5		-22.5	
23.0		-23.0	
23.5		-23.5	
24.0		-24.0	
24.5		-24.5	
25.0		-25.0	

Measurement protocol for the image quality, accuracy of attenuation, and scatter corrections (NEMA Section 6)

Date: _____

Radionuclide: 18F (FDG) at 3.7 MBq ±5% (3.515 - 3.885 MBq)

Phantom: One small compartment filled with air, another with distilled water.

Large (hot) region filled with activity.

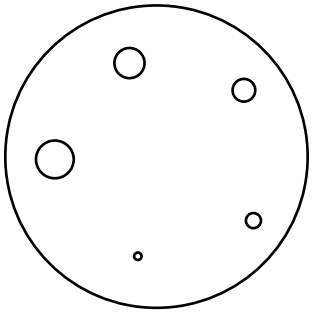

Mark the rod that is in line (or close to) Air compartment.

Emission scan to include whole axial length (50mm) – 20 min.

20 min does not include time required for attenuation measurements

Energy window (keV): _____

Injected activity (MBq): _____

Injection time (hh:mm): _____

Scan start at (hh:mm): _____

Report reconstruction parameters:

Zoom: _____

Pixel size: _____

Algorithm: _____

Number of iterations: _____

Filter (type and width): _____